

POLITECNICO DI TORINO

**Corso di Laurea Magistrale
in Ingegneria Meccanica**

Tesi di Laurea Magistrale

**Data driven Modeling of Turbulent Flows using
Artificial Neural Networks**



Relatore

Prof. Alessandro Ferrari

Candidato

Luca Lamberti

Anno accademico 2018/2019

ACKNOWLEDGMENTS

I would like to express special appreciation to Professor Roberto Paoli, who constantly proved to be exceptionally kind and available towards me, weekly keeping up-to-date and suggesting new solutions for the thesis work.

My thankfulness extends to Professor Alessandro Ferrari, whose dedication and accentuated curiosity towards research and innovation encouraged hard work.

Furthermore, I wish to thank my girlfriend Isabella, who constantly stood by me in all difficult moments during these five years and during the thesis development.

Finally, I wish to express deep gratitude to my family, my father Lucio, my mother Elvira and sister Chiara, who in innumerable occasions in the last five years supported my commitment and hopes.

TABLE OF CONTENTS

<u>CHAPTER</u>		<u>PAGE</u>
1	INTRODUCTION	1
1.1	Motivations	1
1.2	Incompressible Reynolds-averaged Navier–Stokes equations	3
1.2.1	Reynolds Decomposition and Derivation of Mean Flow Equations	4
1.3	The closure problem	6
1.3.1	Turbulent-viscosity models	7
1.3.2	General eddy-viscosity model	11
1.4	Data Driven Turbulence Modeling	14
1.4.1	Neural Networks	14
1.4.2	Training of a Neural Network	16
1.4.3	The Tensor-Basis neural network	18
1.4.4	Description of the proposed approach	20
2	IMPLEMENTATION OF THE METHOD	25
2.1	Development of a RANS CFD Solver	25
2.1.1	Nondimensionalization of the governing equations	28
2.1.2	The Marker and Cell (MAC) method	32
2.1.3	Discretization of the equations	33
2.1.4	X momentum equation	34
2.1.5	Y momentum equation	36
2.1.6	k transport equation	38
2.1.7	ε transport equation	40
2.1.8	Poisson Equation	42
2.1.9	Poisson Equation Solver	45
2.2	Turbulent fully-developed channel flow	46
2.2.1	Mesh	48

TABLE OF CONTENTS (continued)

2.2.2	Boundary Conditions	50
2.2.3	Validation of the solver	62
2.3	Artificial Neural Network	65
2.3.1	High-Fidelity datasets	67
2.3.2	Input layers' normalizations	68
2.3.3	Network's hyperparameters and architecture	71
2.3.4	Training phase and a priori result	75
2.3.5	Embedment of the neural network into the CFD solver	78
3	RESULTS AND CONCLUSIONS	80
3.1	Application to the turbulent channel flow case	80
3.2	Effect on the mean velocity	87
3.3	Conclusions	91
	CITED LITERATURE	93

LIST OF FIGURES

<u>FIGURE</u>	<u>PAGE</u>
1 Reynolds decomposition	4
2 Diagram of a fully-connected feed-forward network with two hidden layers	14
3 Schematic of the TBNN architecture	19
4 Comparison of a standard RANS solver with the proposed approach	23
5 Standard data driven turbulence modelling approach (a) and proposed method (b)	24
6 Structured meshes	26
7 Grid resolutions for wall-functions and near-wall modeling approaches	27
8 Staggered Arrangement	33
9 Centered approximation of the first derivative	34
10 Control volume for the x-momentum equation	35
11 Control volume for the y-momentum equation	37
12 Control volume for the k-transport equation	39
13 Control volume for the ε -transport equation	41
14 Control volume for the continuity equation	43
15 Geometry of the channel flow	47
16 Mesh for the turbulent channel flow	48
17 Magnification of the mesh for the turbulent channel flow, near-wall resolution	49
18 Channel flow boundary conditions	51
19 Ghost cells	52
20 Ghost cells for bottom wall boundary condition	55
21 Ghost cells for top symmetry boundary condition	57
22 Ghost cells for left zero-gradient boundary condition	60
23 Ghost cells for left zero-gradient boundary condition	61
24 Solver validation: Channel flow $u^+(y^+)$ profile	63
25 Solver validation: Channel flow $u^+(y/\delta)$ profile	64

LIST OF FIGURES (continued)

26	Solver validation: Channel flow $k^+(y^+)$ and $\langle uv(y^+) \rangle$ profiles	64
27	Solver validation: von Karman constant	65
28	Train and validation RMSE	75
29	A priori Predictions of Reynolds stress anisotropy tensor on the Duct Flow case . . .	76
30	Baseline LEVM Predictions of Reynolds stress anisotropy tensor on the Duct Flow case	77
31	Embedment of the neural network into the CFD solver	78
32	Turbulent Channel Flow: Reynolds stresses profiles with LEVM	81
33	Turbulent Channel Flow: DNS Reynolds stresses profiles	82
34	Turbulent Channel Flow: DNS, LEVM and TBNN Reynolds Stresses profiles' comparison	83
35	Turbulent Channel Flow: TBNN Reynolds stresses profiles	84
36	Coefficient $g^{(1)}$ predicted by TBNN at first solver iteration	85
37	Coefficients $g^{(n)}$ predicted by TBNN at first solver iteration	86
38	Mean velocity field resulting from enforcing true DNS anisotropy tensor	88
39	Mean velocity field resulting from the TBNN approach	89
40	Turbulent Channel Flow: TBNN $\langle uv \rangle$ predicted profile	90

LIST OF TABLES

<u>TABLE</u>		<u>PAGE</u>
I	NEURAL NETWORKS' KEY TERMINOLOGY	66
II	NEURAL NETWORK'S TRAINING AND VALIDATION DATASET	67
III	NEURAL NETWORK'S ARCHITECTURE	73
IV	MODEL'S CHARACTERISTICS	74

SUMMARY

Numerical simulations based on Reynolds-averaged Navier Stokes (RANS) models are still the workhorse tool in engineering design involving turbulent flows. Two decades ago, when LES started gaining popularity thanks to the increasing availability of computational resources, it was widely expected that it would have gradually replaced RANS methods in industrial CFD for decades to come. In the past two decades, however, while LES-based methods gained widespread applications and the earlier hope did not diminish, the predicted time when LES would replace RANS has been significantly delayed. Most industrial users are probably decades away from any routine use of scale resolving simulations, not to mention the cost, time and user skill it take to run these computations. In brief, RANS solvers, particularly those based on standard eddy viscosity models (e.g $k-\varepsilon$, $k-\omega$, S-A and $k-\omega$ SST) are expected to remain the workhorse in the CFD of high Reynolds number flows for decades. However, predictions from RANS simulations are known to have large discrepancies in many flows of engineering relevance, including those with swirl, pressure gradients, or mean streamline curvature. It is a consensus that the dominant cause for such discrepancies is the RANS-modeled Reynolds stresses. In light of the long stagnation in traditional turbulence modeling, researchers explored machine learning as an alternative to improve RANS modeling by leveraging data from high-fidelity simulations. The goal is to make use of vast amounts of turbulent flows data, machine learning techniques and current understanding of turbulence physics to develop models with better predictive capabilities in the context of RANS simulations. Recently, in a seminal work, Ling et al (2016) developed a neural network architecture capable of embedding invariance properties into the Reynolds stressor predicted in output. Such a network, named the tensor basis neural network (TBNN), was applied to a variety of flow fields with encouraging results compared to both classical turbulence models and neural networks that do not preserve Galilean invariance. Yet, as in most data driven turbulence modelling approaches, the TBNN was used as a post-processing tool to correct the Reynolds stress tensor field predicted by a RANS simulation run with standard closure models. This means that, theoretically, the network can be applied only to correct the Reynolds stress tensor for the same RANS model on which it has been trained since, in general, different turbulence models yield different results depending on the flow type. Moreover, there is no physical insight that suggests a relation between the RANS velocity gradients - used as inputs of the machine learning model - and the true Reynolds stress tensor.

SUMMARY (continued)

Differently, in this work a network with a similar architecture to the Ling's one was be trained and tested on a database of high-fidelity data of eight different flows to learn a functional mapping between the inputs of Pope's General Eddy Viscosity Model and the anisotropic part of the Reynolds stress tensor. Then the network was embedded into a CFD RANS solver as a replacement of the standard closure model - and therefore called at every solver's iteration. Lasty, the RANS solver with embedded TBNN was be tested on a canonical flow case - turbulent channel flow - to evaluate its performances. As for the organization of this work: in Chapter 1 further details on the data driven turbulence modelling will be given, RANS models and equations will be introduced and also an introduction to Neural Networks will be presented. In Chapter 2, it will be given a detailed explanation of the RANS CFD solver and the neural network's implementation. Finally, in Chapter 3, the method will be tested on a turbulent channel flow case and the results will be discussed.;

Chapter 1

INTRODUCTION

1.1 Motivations

Turbulence is a common physical characteristic of many industrial fluid flows.

For example, in wind turbine design, the knowledge of turbulent quantities in the incoming flow and in the blade boundary layers is important for performance. In internal combustion engines, vigorous turbulence increases fuel/air mixing, thus improving overall efficiency and reducing emissions. In airplane design, delaying the occurrence of turbulence in boundary layers over the wing surfaces leads to reduced fuel consumption [16].

These examples, and a vast number of other applications, demonstrate the importance of determining the effect of turbulence on the performance of engineering devices and justify the continuous interest in developing more accurate techniques to simulate and predict turbulent flows.

Nowadays, two techniques are at the industry's computational power's reach for the numerical simulation of turbulence flows: RANS (Reynolds Averaged Naviers Stokes) Simulations and LES (Large Eddy Simulations). DNS use (Direct Numerical Simulations), despite proving to be the most accurate method for all turbulent flows' simulation, is still limited to research purposes and canonical flows' applications, since the computational power required is well beyond industry capabilities.

Two decades ago, when LES started gaining popularity thanks to the increasing availability of computational resources, it was widely expected that it would have gradually replaced RANS methods in industrial CFD for decades to come. In the past two decades, however, while LES-based methods such as wall-modeled LES and hybrid LES/RANS methods gained widespread applications and the earlier hope did not diminish, the predicted time when LES would replace RANS has been significantly delayed[15].

It is under these premises that, in July 2017, a three day Turbulence Modeling Symposium sponsored by the University of Michigan and NASA, was held in Ann Arbor, Michigan [12]. The meeting gathered nearly 90 experts from academia, government and industry in order to discuss the state of the art in turbulence modeling and to wrestle with questions surrounding its future. One message came through very clearly from the participants of the symposium: industry still need RANS, all the time. Most industrial users are probably decades away from any routine use of scale resolving simulations, not to mention the cost, time and user skill it take to run these computations. In brief, RANS solvers, particularly those based on standard eddy viscosity models (e.g $k-\varepsilon$, $k-\omega$, S-A and $k-\omega$ SST) are expected to remain the workhorse in the computation of high Reynolds number CFD for decades. This is likely to be true even in mission critical design applications such as aircraft design. Interestingly, even the advanced RANS models (such as Reynolds stress transport models and Explicit Algebraic Reynolds stress models) have not seen much development in the past few decades; these methods are indeed more computationally expensive and less robust than the standard eddy viscosity RANS models [14]. As a consequence, the need for standard RANS model improvements remains a key issue in CFD research not just in the near-term.

In today's CFD landscape, RANS is widely used, mostly in a steady mode, although the known weaknesses of this approach in predicting many classes of flows can be very problematic. In particular, RANS is considered less adequate or even unacceptable for classes of flows involving massive separations or severe streamlines curvatures [12].

Indeed, even the most sophisticated RANS models invoke radically simplifying assumptions about the structure of the underlying turbulence. As a result, even if a model is based on physically and mathematically appealing ideas, the model formulation typically devolves into the calibration of a large number of free parameters or functions using a small set of canonical problems. Even after decades of efforts in the turbulence modeling community, universally applicable RANS models with predictive capabilities are the main source that limits the predictive accuracy of RANS models [13]. Large discrepancies in the RANS-modeled Reynolds Stresses are the main source that limits the predictive accuracy of RANS models.

For example, at the present time of this work, the most popular standard two-equation RANS models rely on the Linear Eddy Viscosity Model (LEVM) for their Reynolds stress closure [9]. This LEVM postulates a linear relationship between the Reynolds stresses and the mean strain rate tensor. However, this model does not provide satisfactory predictive accuracy in many engineering-relevant flows such as those with curvature, impingement and separation and simple shear flows [38]. More advanced nonlinear eddy viscosity models have also been proposed which rely on higher-order products of the

mean strain rate and rotation rate tensors. These nonlinear models have not gained widespread usage because they do not give consistent performance improvement over the LEVM and often lead to worsened convergence properties [9].

It is however clear that a significative improvement of the eddy viscosity models in standard RANS methods would mitigate a very important source of discrepancy in Reynolds stress modeling. While traditional development of turbulence models has focused on incorporating more physics to improve predictive capabilities, an alternative approach is to use data [14]. Indeed, given the recent rise of data science, it is fair to ask ourselves: can we use vast amounts of turbulent flows data, machine learning techniques and current understanding of the physics of turbulence to setup a framework that can lead to develop models with better predictive capabilities in the context of RANS simulations [13]?

The goal of the present work is to address this question by attempting to develop an alternative and more accurate Reynolds stress closure model using available turbulent datasets and machine learning techniques. In particular, deep neural networks are chosen as the tool to extract improved models from large sets of data due to the possibility of exploiting the flexibility of their architecture in order to embed invariance tensor properties into the machine learning model [9].

1.2 Incompressible Reynolds-averaged Navier–Stokes equations

Scientists and engineers seek to predict and understand the velocity \mathbf{U} and pressure fields p of a variety of fluid flows. For low-Mach flows with negligible gravity effects, the challenge facing scientists and engineers is to solve the incompressible Navier-Stokes equations:

$$\nabla \cdot \mathbf{U} = 0 \quad (1.1)$$

$$\frac{\partial \mathbf{U}}{\partial t} + \nabla \cdot (\mathbf{U} \otimes \mathbf{U}) = -\frac{1}{\rho} \nabla p + \nu \nabla^2 \mathbf{U} \quad (1.2)$$

for the three-dimensional velocity field $(U) = (u; v; w)$ and the pressure field p , which are in general functions of space and time [37]. Equation (1.1) is called continuity equation and corresponds to the conservation of mass, whereas (1.2) corresponds to the conservation of momentum equation.

The parameters ν and ρ are the kinematic viscosity and density of the fluid, respectively. The key dimensionless parameter in incompressible fluid mechanics, the Reynolds number Re , is formed by a velocity scale U and a length scale L and is given by $Re = UL/\nu$. As a global rule, a large Re indicates that the fluid flow is turbulent whereas a small Re suggests a laminar flow field. Many flows of scientific and engineering interest are in a turbulent regime, which is characterized by many simultaneously active temporal and spatial scales. Analytical approaches to solving the Navier-Stokes

equations have succeeded for only the simplest flow fields, hence the need to solve equations (1.1) and (1.2) numerically.

Equations (1.1) and (1.2) can be written in a useful form using Einstein notation:

$$\frac{\partial U_i}{\partial x_i} = 0 \quad (1.3)$$

$$\frac{\partial U_j}{\partial t} + \frac{\partial}{\partial x_i} (U_i U_j) = -\frac{1}{\rho} \frac{\partial p}{\partial x_j} + \frac{\partial}{\partial x_i} \left[\nu \left(\frac{\partial U_i}{\partial x_j} + \frac{\partial U_j}{\partial x_i} \right) \right] \quad (1.4)$$

1.2.1 Reynolds Decomposition and Derivation of Mean Flow Equations

The earliest rigorous mathematical attempt at resolving the turbulence problem was due to Osborn Reynolds. Reynolds' idea is to decompose the fields into its mean and fluctuating part:

$$\mathbf{U}(\mathbf{x}, t) = \langle \mathbf{U}(\mathbf{x}, t) \rangle + \mathbf{u}(\mathbf{x}, t) \quad (1.5)$$

where:

$$\langle \mathbf{U}(\mathbf{x}, t) \rangle = \lim_{T \rightarrow \infty} \frac{1}{T} \int_t^{t+T} \mathbf{U}(\mathbf{x}, t') dt' \quad (1.6)$$

corresponds to the application of the averaging operator to the flow field $\mathbf{U}(\mathbf{x}, t)$. Equation (1.6) is referred to as the Reynolds decomposition.

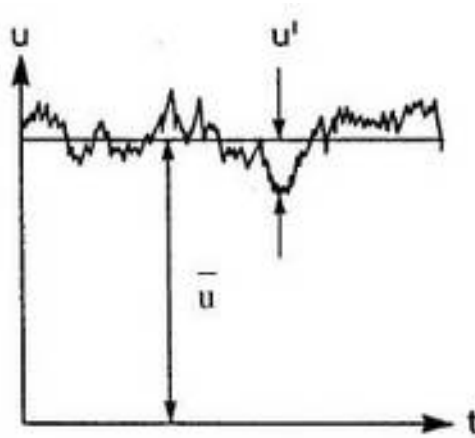


Figure 1: Reynolds decomposition

In most engineering applications, only the average components of the flow field are relevant. One could therefore think of applying the $\langle \cdot \rangle$ averaging operator to equations (1.3) and (1.4) in order to obtain equations for the mean flow. In doing so, it is firstly crucial to observe that $\langle \cdot \rangle$ averaging operator commutes with spatial and time derivatives.

By applying $\langle \cdot \rangle$ averaging operator to continuity equation (1.3) one has:

$$\left\langle \frac{\partial U_i}{\partial x_i} \right\rangle = \frac{\partial \langle U_i \rangle}{\partial x_i} = 0$$

The derivation of the mean momentum equation is slightly longer. First of all, it is crucial to notice that the mean of a fluctuation is null:

$$\langle \mathbf{u} \rangle = \langle (\mathbf{U} - \langle \mathbf{U} \rangle) \rangle = \langle \mathbf{U} \rangle - \langle \langle \mathbf{U} \rangle \rangle = \langle \mathbf{U} \rangle - \langle \mathbf{U} \rangle = 0$$

since the mean of a mean of a quantity is the mean of the quantity itself ($\langle \langle f \rangle \rangle = \langle f \rangle$). We can now derive each term of the mean momentum equation separately :

1.

$$\left\langle \frac{\partial U_j}{\partial t} \right\rangle = \frac{\partial \langle U_j \rangle}{\partial t}$$

2.

$$\begin{aligned} \left\langle \frac{\partial}{\partial x_i} (U_i U_j) \right\rangle &= \frac{\partial}{\partial x_i} (\langle U_i U_j \rangle) = \frac{\partial}{\partial x_i} (\langle (\langle U_i \rangle + u_i) \cdot (\langle U_j \rangle + u_j) \rangle) \\ &= \frac{\partial}{\partial x_i} (\langle \langle U_i \rangle \langle U_j \rangle + u_i \langle U_j \rangle + u_j \langle U_i \rangle + u_i u_j \rangle) \\ &= \frac{\partial}{\partial x_i} (\langle \langle U_i \rangle \langle U_j \rangle \rangle + \langle u_i \rangle \langle U_j \rangle + \langle u_j \rangle \langle U_i \rangle + \langle u_i u_j \rangle) \\ &= \frac{\partial}{\partial x_i} (\langle U_i \rangle \langle U_j \rangle + \langle u_i u_j \rangle) \end{aligned}$$

3.

$$\left\langle \frac{1}{\rho} \frac{\partial p}{\partial x_j} \right\rangle = \frac{1}{\rho} \frac{\partial \langle p \rangle}{\partial x_j}$$

4.

$$\left\langle \frac{\partial}{\partial x_i} \left[\nu \left(\frac{\partial U_i}{\partial x_j} + \frac{\partial U_j}{\partial x_i} \right) \right] \right\rangle = \frac{\partial}{\partial x_i} \left[\nu \left(\frac{\partial \langle U_i \rangle}{\partial x_j} + \frac{\partial \langle U_j \rangle}{\partial x_i} \right) \right]$$

Collecting the time-averaged continuity and momentum equations one has:

$$\frac{\partial \langle U_i \rangle}{\partial x_i} = 0 \tag{1.7}$$

$$\frac{\partial \langle U_j \rangle}{\partial t} + \frac{\partial}{\partial x_i} (\langle U_i \rangle \langle U_j \rangle) = -\frac{1}{\rho} \frac{\partial \langle p \rangle}{\partial x_j} + \frac{\partial}{\partial x_i} \left[\nu \left(\frac{\partial \langle U_i \rangle}{\partial x_j} + \frac{\partial \langle U_j \rangle}{\partial x_i} \right) \right] - \frac{\partial \langle u_i u_j \rangle}{\partial x_i} \tag{1.8}$$

which correspond to the Reynolds-averaged Navier–Stokes equations (or RANS equations) of motion for fluid flow. Equation (1.8) can be rewritten the substantial mean derivative in conservative form:

$$\frac{\overline{D} \langle U_j \rangle}{\overline{D} t} = \frac{\partial}{\partial x_i} \left[\nu \left(\frac{\partial \langle U_i \rangle}{\partial x_j} + \frac{\partial \langle U_j \rangle}{\partial x_i} \right) - \frac{1}{\rho} \langle p \rangle \delta_{ij} - \langle u_i u_j \rangle \right] \tag{1.9}$$

where the mean substantial derivative is:

$$\frac{\overline{D}\langle U_j \rangle}{\overline{Dt}} = \frac{\partial \langle U_j \rangle}{\partial t} + \frac{\partial}{\partial x_i} (\langle U_i \rangle \langle U_j \rangle)$$

Equation (1.9) is the general form of a momentum conservation equation with the term in the square brackets representing the sum of three specific stresses: the viscous specific stress, the isotropic specific stress $-\langle p \rangle / \delta_{ij} \rho$ and the apparent stress arising from the fluctuating velocity field $-\langle u_i u_j \rangle$.

The term $-\langle u_i u_j \rangle$ is usually referred to as *Reynolds Stress Tensor* and, in general, corresponds to a second order 3x3 tensor:

$$\langle u_i u_j \rangle = \begin{bmatrix} \langle u_1^2 \rangle & \langle u_1 u_2 \rangle & \langle u_1 u_3 \rangle \\ \langle u_2 u_1 \rangle & \langle u_2^2 \rangle & \langle u_2 u_3 \rangle \\ \langle u_3 u_1 \rangle & \langle u_3 u_2 \rangle & \langle u_3^2 \rangle \end{bmatrix} \quad (1.10)$$

where 1,2,3 correspond to the three directions of the System Reference Frame (such as x,y,z). The single terms of the tensor are referred to as Reynolds stresses.

The Reynolds Stress Tensor (1.10) is obviously symmetric, since $\langle u_i u_j \rangle = \langle u_j u_i \rangle$. The diagonal components $\langle u_1^2 \rangle = \langle u_1 u_1 \rangle$, $\langle u_2^2 \rangle$ and $\langle u_3^2 \rangle$ are called *normal stresses* while the off-diagonal components are called *shear stresses*. A crucial turbulence statistic linked to the Reynolds stresses is the *turbulent kinetic energy* $k(\mathbf{x}, t)$ (TKE), which is defined to be half of the trace of Reynolds stress tensor:

$$k = \frac{1}{2} \langle u_i u_i \rangle \quad (1.11)$$

It is a scalar and corresponds to the mean kinetic energy per unit of mass in the fluctuating velocity field. The distinction between shear stresses and normal stresses is dependent on the choice of coordinate system. An intrinsic distinction can be made between *isotropic stresses* and *anisotropic stresses*. The isotropic stress is $\frac{2}{3} k \delta_{ij}$ and then the deviatoric anisotropic part is:

$$a_{ij} = \langle u_i u_j \rangle - \frac{2}{3} k \delta_{ij} \quad (1.12)$$

Lastly, the normalized anisotropy tensor - which will be used extensively in this work - is defined as:

$$b_{ij} = \frac{a_{ij}}{2k} = \frac{\langle u_i u_j \rangle}{2k} - \frac{1}{3} \delta_{ij} \quad (1.13)$$

1.3 The closure problem

With the notable exception of the Reynolds stress tensor, the RANS equations are identical to the Navier-Stokes equations. However, the presence of this addition single term poses a key issue in the

solution of mean flow equations. Indeed, for a general statistically three-dimensional flow, there are four independent equations governing the mean velocity field: namely three components of the momentum equation (1.6) and the continuity equation (1.5). However, differently from the instantaneous Navier Stokes equations (1.1) and (1.2), they contain more than four unknowns. In addition to the three components of $\langle \mathbf{U} \rangle$ and to $\langle p \rangle$, there are also the Reynolds stresses.

Such a system, with more unknowns than equations, is said to be unclosed and therefore cannot be solved. Additional relations must be specified to determine $\langle u_i u_j \rangle$ and close the system of equations. Although exact transport equations can be derived for the Reynolds stresses from the Navier-Stokes equations, these involve third-order moments of the velocity field. Indeed, attempting to close the RANS equations results in an infinite cascade of unclosed terms which have to be modeled again. Not to mention that the solution of six additional transport equations - one for each component of the Reynolds stress tensor- requires a considerable computational cost. Efforts have therefore focused primarily on modeling the effects of the Reynolds stress tensor on the mean flow field. The goal of turbulence modeling is to propose useful and tractable models for $\langle u_i u_j \rangle$. This entails the attempt to relate it to mean flow quantities and other turbulence statistic whose transport equation can be solved, in order to provide a closure to the set of equations (1.5), (1.6). Note that the Navier-Stokes equations have a variety of transformation properties. Of particular consequence in the present work is Galilean invariance. That is, the Navier-Stokes equations are the same in an inertial reference frame that is translating with a constant velocity \mathbf{V} . Hence, replacing the spatial coordinate with $(\mathbf{x} - \mathbf{V}t)$ and the velocity with $\mathbf{U} - \mathbf{V}$ does not change the form of the Navier-Stokes equations. This fact remains true even for the RANS equations. Therefore, any turbulence model for the Reynolds stress tensor must also preserve Galilean invariance.

1.3.1 Turbulent-viscosity models

Significant modelling efforts have been devoted to finding closures for the Reynolds stresses. The majority of the most popular approaches fall into the class of turbulent-viscosity models, which are based on the *turbulent-viscosity hypothesis* [38]. This was introduced in 1877 by Boussinesq and is mathematically analogous to the stress-rate-of-strain relation for a Newtonian fluid. The turbulent-viscosity hypothesis can be viewed in two parts. First, there is the *intrinsic* assumption that, at each point and time, the Reynolds stress anisotropy tensor a_{ij} is a function of the mean velocity gradients $\partial \langle U_i \rangle / \partial x_j$ at the same point and time. Second, there is the *specific* assumption that the relationship

between a_{ij} and $\partial\langle U_i\rangle/\partial x_j$ is:

$$a_{ij} = -\nu_T \left(\frac{\partial\langle U_i\rangle}{\partial x_j} + \frac{\partial\langle U_j\rangle}{\partial x_i} \right) = -2\nu_T \langle S_{ij} \rangle \quad (1.14)$$

where $\langle S_{ij} \rangle$ is the mean rate-of-strain tensor and ν_T is a scalar called *turbulent eddy viscosity*. The model given by (30) is called the *linear eddy viscosity model* (LEVM) because the Reynolds stresses are a linear function of the mean velocity gradients. The eddy viscosity model is motivated via analogy with the molecular theory of gases. The turbulent flow is thought of as consisting of multiple interacting eddies. The eddies exchange momentum giving rise to an eddy viscosity. Although convenient, the eddy viscosity hypothesis is known to be incorrect for many flow fields. The intrinsic assumption that the Reynolds stresses only depend on local mean velocity gradients is incorrect; turbulence is a temporally and spatially non-local phenomenon. Moreover, the specific form proposed in analogy with the molecular theory of gases (30) is also flawed because the turbulence timescales are at odds with the timescales in the molecular theory of gases. Nevertheless, the eddy viscosity model is appealing due to its simplicity and ease of numerical implementation. This is the main reason why most of the popular standard RANS models rely on such a closure [9].

If the turbulent-viscosity hypothesis is accepted as an adequate approximation, all that remains to determine is an appropriate specification of the turbulent viscosity $\nu_T(\mathbf{x}, t)$. In the most popular low equations RANS models, it is expressed as a function of one or two turbulent quantities.

One of the most commonly used forms for the eddy viscosity is the $k - \varepsilon$ model:

$$\nu_T = C_\mu \frac{k^2}{\varepsilon} \quad (1.15)$$

where:

$$\varepsilon = \nu \left\langle \frac{\partial u_i}{\partial x_j} \frac{\partial u_j}{\partial x_i} \right\rangle \quad (1.16)$$

is the dissipation rate of turbulent kinetic energy; it coincides with the dissipation term in the turbulent kinetic energy transport equation. In general, the model constant C_μ must be calibrated for different flows. A common choice is $C_\mu = 0.09$ which has been observed in channel flow and in the temporal mixing layer.

From (1.15), it is clear that, the computation of $\nu_T(\mathbf{x}, t)$ requires to determine first the $k(\mathbf{x}, t)$ and $\varepsilon(\mathbf{x}, t)$ fields. The idea of the $k - \varepsilon$ model is to derive them by solving the transport equations for the two turbulent statistics, along with the solution of the mean Navier-Stokes equations. From the definition (1.11) of the turbulent kinetic energy, it is possible to derive its exact transport equation from the instantaneous Navier-Stokes system of equations. By using the Reynolds decomposition and

by applying the averaging operator $\langle \cdot \rangle$, equations (1.3) and (1.4) can be usefully manipulated to obtain:

$$\frac{\partial k}{\partial t} + \langle \mathbf{U} \rangle \cdot \nabla k = \frac{\overline{Dk}}{\overline{Dt}} = -\nabla \cdot \mathbf{T}' + P - \varepsilon \quad (1.17)$$

where:

- $T'_i = \frac{1}{2} \langle u_i u_j u_j \rangle + \langle u_i p' \rangle - \nu \frac{\partial k}{\partial x_j}$ is the turbulent kinetic energy flux, with $p' = p - \langle p \rangle$ being the pressure fluctuation.
- $P = -\langle u_i u_j \rangle \frac{\partial \langle U_i \rangle}{\partial x_j}$ is the production of turbulent kinetic energy.
- ε is the dissipation rate, defined by equation (1.16).

In Eq.(1.17), any term that is completely determined by the knowns of the RANS equation with the closure model (30) - namely the mean velocity and pressure fields and the Reynolds stress tensor - is said to be in closed form. It is clear that the terms ε and $-\nabla \cdot \mathbf{T}'$ are unknowns and, in order to obtain a closed set of equations, these terms must be modeled. In the standard $k - \varepsilon$ model, the turbulent kinetic energy flux is modelled with a gradient-diffusion hypothesis as:

$$\mathbf{T}' = -\frac{\nu_T}{\sigma_k} \nabla k \quad (1.18)$$

where the turbulent Prandtl number for kinetic energy is generally taken to be $\sigma_k = 1$. Mathematically, the term ensures that the resulting model transport equation for k yields smooth solutions and that a boundary condition can be imposed on k everywhere on the boundary of the solution domain. By substituting (1.18) into (1.17), one obtains the model transport equation for k :

$$\frac{\partial k}{\partial t} + \langle \mathbf{U} \rangle \cdot \nabla k = \frac{\overline{Dk}}{\overline{Dt}} = \nabla \cdot \left(\frac{\nu_T}{\sigma_k} \nabla k \right) + P - \varepsilon \quad (1.19)$$

In order to close the set of equations, it remains to specify a transport equation for ε . An exact equation can be derived, but it is not a useful starting point for a model equation. Consequently, rather than being based on the exact equation, the standard model equation for ε is best viewed as being entirely empirical. It is:

$$\frac{\partial \varepsilon}{\partial t} + \langle \mathbf{U} \rangle \cdot \nabla \varepsilon = \frac{\overline{D\varepsilon}}{\overline{Dt}} = \nabla \cdot \left(\frac{\nu_T}{\sigma_\varepsilon} \nabla \varepsilon \right) + C_{\varepsilon 1} \frac{P\varepsilon}{k} - C_{\varepsilon 2} \frac{\varepsilon^2}{k} \quad (1.20)$$

The standard values of all the model constants in the $k - \varepsilon$ equations due to Launder and Sharma are:

$$C_\mu = 0.09 \quad C_{\varepsilon 1} = 1.44 \quad C_{\varepsilon 2} = 1.92 \quad \sigma_k = 1 \quad \sigma_\varepsilon = 1.3 \quad (1.21)$$

In general, the model constants should be calibrated case by case for different flows, since the values (1.21) are obtained from physical insights derived from only a small sets of canonical flows. Altogether, the mean flow equations (1.5) and (1.6), the transport equations for k and ε and the turbulent

viscosity hypothesis (30) represent a closed set of equations that can be solved to obtain the mean velocity and pressure fields. The $k - \varepsilon$ model is called a *two - equation model* because two additional transport equations are solved for the two turbulent quantities k and ε . The two equation models are nowadays the most frequently employed in the industry since they represent a good compromise between the computational effort required and the solution accuracy obtained [31].

It is however clear that, due to all the assumptions and simplifications used in their derivation, the solution of these equations will not have several limits to its applications.

Historically, many two equation models have been proposed. In most of these, k is taken as one of the two turbulent statistics to determine ν_T but there are different choices for the second variable. Another class of very popular two-equation models are the $k - \omega$ ones, where $\omega = \varepsilon/k$ is taken as the second turbulent variables. In its original form due to Wilcox, the following model equation for ω is solved:

$$\frac{\partial \omega}{\partial t} + \langle \mathbf{U} \rangle \cdot \nabla \omega = \frac{\overline{D}\omega}{\overline{D}t} = \nabla \cdot \left(\frac{\nu_T}{\sigma_\omega} \nabla \omega \right) + C_{\omega 1} \frac{P\omega}{k} - C_{\omega 2} \omega^2 \quad (1.22)$$

and the turbulent viscosity is computed analogously to the $k - \varepsilon$ model as (1.15) by simply substituting $\varepsilon = \omega k$. The constants of (1.22) are calibrated analogously to the $k - \varepsilon$. It is important to observe that (1.22) differs from the ω equation implied by the $k - \varepsilon$ model and by the definition of $\omega = \varepsilon/k$. Indeed, even if one calibrates the model constants to make the models identical in some specific cases - such as homogeneous turbulence - the equation for ω implied by the $k - \varepsilon$ model:

$$\frac{\partial \omega}{\partial t} + \langle \mathbf{U} \rangle \cdot \nabla \omega = \frac{\overline{D}\omega}{\overline{D}t} = \nabla \cdot \left(\frac{\nu_T}{\sigma_\omega} \nabla \omega \right) + (C_{\varepsilon 1} - 1) \frac{P\omega}{k} - (C_{\varepsilon 2} - 1) \omega^2 + \frac{2\nu_T}{k\sigma_\omega} \nabla \omega \cdot \nabla k \quad (1.23)$$

contains an additional term compared to (1.22), in particular the last one.

As described by Wilcox (1993), for boundary layers flows the $k - \omega$ model yields superior results compared to $k - \varepsilon$ model, both in the treatment of the viscous near-wall region and in its accounting for the effects of streamwise pressure gradient. However, the treatment of non-turbulent free-stream boundaries is problematic.

Menter (1994) proposed a two equation model designed to yield the best behavior of the $k - \varepsilon$ and $k - \omega$ models. In this model, the transport equation employed for ω is in the form (1.23) but with the final term multiplied by a blending function. Close to the walls, the bending function is zero (leading to the standard Wilcox ω equation) whereas remote from the wall the blending functions tend to 1 (thus producing the standard ε equation).

In 1994 Spalart and Allmaras introduced a one-equation model developed for aerodynamic applications, in which a single model transport equation is solved for the turbulent viscosity ν_T . The model

equation is of the form:

$$\frac{\partial \nu_T}{\partial t} + \langle \mathbf{U} \rangle \cdot \nabla \nu_T = \frac{\overline{D} \nu_T}{\overline{D} t} = \nabla \cdot \left(\frac{\nu_T}{\sigma_\nu} \nabla \nu_T \right) + S_\nu \quad (1.24)$$

where the source term S_ν depends on the laminar and turbulent viscosities, on the mean rate or rotation tensor $\langle \mathbf{R} \rangle$, on the turbulent viscosity gradient and on the distance from the nearest wall. In applications to the aerodynamic flows for which it is intended, the model has proved quite successful. However, it has a clear limitation as a general model.

It is indeed important to realize that the choice of the turbulent model to use is always a compromise. If accuracy were the only criterion in the selection of the model, then the choice would naturally tend toward models with higher level of description of turbulence and hence with more transport equations involved. However, cost and ease of use are also important criteria that favor the simpler models. This may justify why, from an informal survey of single phase RANS model usage based on papers published in the Journal of Fluids Engineering during 2009 – 2011 it, emerged that over 2/3 of all simulations reported used some variation of 1 or 2 equation models (S-A, $k - \varepsilon$ family and $k - \omega$ family) [31].

This fact should also motivate the attempt to improve those models at all levels by trying to mitigate their various sources of errors, yet keeping their simplicity and advantageous properties.

1.3.2 General eddy-viscosity model

In a two-equation model, the scaling turbulent parameters - such as ε and k , can be used to normalize the mean rate of strain $\langle \mathbf{S} \rangle$ and rate of rotation $\langle \mathbf{R} \rangle$ tensors as suggested by Pope [11]:

$$\langle s_{ij} \rangle = \frac{1}{2} \frac{k}{\varepsilon} \left(\frac{\partial \langle U_i \rangle}{\partial x_j} + \frac{\partial \langle U_j \rangle}{\partial x_i} \right) = \frac{k}{\varepsilon} \langle S_{ij} \rangle \quad (1.25)$$

$$\langle r_{ij} \rangle = \frac{1}{2} \frac{k}{\varepsilon} \left(\frac{\partial \langle U_i \rangle}{\partial x_j} - \frac{\partial \langle U_j \rangle}{\partial x_i} \right) = \frac{k}{\varepsilon} \langle R_{ij} \rangle \quad (1.26)$$

If we substitute the expression for nu_T (1.15) into the linear eddy viscosity model (30), by using the definition of normalized anisotropy tensor b_{ij} (1.13) one has:

$$\mathbf{b} = -2C_\mu \langle \mathbf{s} \rangle \quad (1.27)$$

where $\langle \mathbf{s} \rangle$ is the normalized rate of strain tensor of (1.25). The deficiencies of the k_ε model and the eddy viscosity assumption have been well discussed above; namely, the inability to account for streamline curvature, turbulence history and so on. However, if one accepts the intrinsic assumption of the turbulent-viscosity hypothesis - namely that the Reynolds stress anisotropy tensor at each time and space point is determined by mean velocity gradients in the same point and time - a more general

eddy viscosity model than the linear relation (1.27) can be derived.

More clearly, if one accepts the relation:

$$b_{ij} = b_{ij}(\langle \mathbf{s} \rangle, \langle \mathbf{r} \rangle) \quad (1.28)$$

where \mathbf{b} and $\langle \mathbf{s} \rangle$ are non-dimensional symmetric tensors with zero trace -due to incompressibility- and $\langle \mathbf{r} \rangle$ is non-dimensional, antisymmetric and with zero-trace, the most general representation of the anisotropic Reynolds stresses in terms of the mean rate of strain and rotation rate tensors is:

$$\mathbf{b} = \sum_{n=1}^{10} g^{(n)}(\lambda_1, \dots, \lambda_5) \mathbf{T}^{(n)} \quad (1.29)$$

where $\mathbf{T}^{(n)}$ are tensors depending on $\langle \mathbf{s} \rangle$ and $\langle \mathbf{r} \rangle$. The form (1.29) guarantees Galilean invariance. If this were not satisfied, then the fluid behavior would be different for observers in different frames of reference [18]. In order to achieve the desired invariance, the coefficients of the tensor basis must depend on the tensor invariants λ_i .

Owing to the Cayley-Hamilton theorem, the number of independent invariants and linearly independent second-order tensors that may be formed from $\langle \mathbf{s} \rangle$ and $\langle \mathbf{r} \rangle$ is finite. This means that the coefficients $g^{(n)}$ in (1.29) are functions of a finite number of invariants. Since \mathbf{a} is symmetric and has zero trace, all the independent tensors $\mathbf{T}^{(n)}$ must satisfy the same property.

In the general three-dimensional case there are 10 independent tensors and 5 invariants. The basis tensors are known functions of the normalized mean rate of strain and rate of rotation tensors $\langle \mathbf{s} \rangle$ and $\langle \mathbf{r} \rangle$ respectively, and are given by:

$$\begin{aligned} \mathbf{T}^{(1)} &= \langle \mathbf{s} \rangle \\ \mathbf{T}^{(2)} &= \langle \mathbf{s} \rangle \langle \mathbf{r} \rangle - \langle \mathbf{r} \rangle \langle \mathbf{s} \rangle \\ \mathbf{T}^{(3)} &= \langle \mathbf{s} \rangle^2 - \frac{1}{3} \mathbf{I} \cdot \text{Tr}(\langle \mathbf{s} \rangle^2) \\ \mathbf{T}^{(4)} &= \langle \mathbf{r} \rangle^2 - \frac{1}{3} \mathbf{I} \cdot \text{Tr}(\langle \mathbf{r} \rangle^2) \\ \mathbf{T}^{(5)} &= \langle \mathbf{r} \rangle \langle \mathbf{s} \rangle^2 - \langle \mathbf{s} \rangle^2 \langle \mathbf{r} \rangle \\ \mathbf{T}^{(6)} &= \langle \mathbf{r} \rangle^2 \langle \mathbf{s} \rangle + \langle \mathbf{r} \rangle \langle \mathbf{s} \rangle^2 - \frac{2}{3} \mathbf{I} \cdot \text{Tr}(\langle \mathbf{s} \rangle \langle \mathbf{r} \rangle^2) \\ \mathbf{T}^{(7)} &= \langle \mathbf{r} \rangle \langle \mathbf{s} \rangle \langle \mathbf{r} \rangle^2 - \langle \mathbf{r} \rangle^2 \langle \mathbf{s} \rangle \langle \mathbf{r} \rangle \\ \mathbf{T}^{(8)} &= \langle \mathbf{s} \rangle \langle \mathbf{r} \rangle \langle \mathbf{s} \rangle^2 - \langle \mathbf{s} \rangle^2 \langle \mathbf{r} \rangle \langle \mathbf{s} \rangle \\ \mathbf{T}^{(9)} &= \langle \mathbf{r} \rangle^2 \langle \mathbf{s} \rangle^2 - \langle \mathbf{s} \rangle^2 \langle \mathbf{r} \rangle^2 - \frac{2}{3} \mathbf{I} \cdot \text{Tr}(\langle \mathbf{s} \rangle^2 \langle \mathbf{r} \rangle^2) \\ \mathbf{T}^{(10)} &= \langle \mathbf{r} \rangle \langle \mathbf{s} \rangle^2 \langle \mathbf{r} \rangle^2 - \langle \mathbf{r} \rangle^2 \langle \mathbf{s} \rangle^2 \langle \mathbf{r} \rangle \end{aligned} \quad (1.30)$$

where \mathbf{I} is the three-dimensional identity tensor and $\text{Tr}(\mathbf{A})$ corresponds to the operation of taking the trace of tensor \mathbf{A} . The five invariants are:

$$\begin{aligned}\lambda_1 &= \text{Tr}(\langle \mathbf{s} \rangle^2) \\ \lambda_2 &= \text{Tr}(\langle \mathbf{r} \rangle^2) \\ \lambda_3 &= \text{Tr}(\langle \mathbf{s} \rangle^3) \\ \lambda_4 &= \text{Tr}(\langle \mathbf{r} \rangle^2 \langle \mathbf{s} \rangle) \\ \lambda_5 &= \text{Tr}(\langle \mathbf{r} \rangle^2 \langle \mathbf{s} \rangle^2)\end{aligned}\tag{1.31}$$

Note that the linear eddy viscosity model is recovered when $g^{(1)} = C_\mu$ and $g^{(n)} = 0$ for $n > 1$.

Finding the coefficients of (1.29) is extremely difficult for general three-dimensional turbulent flows, with the aggravation that there is no obvious hierarchy of the basis components [11]. There are additional shortcomings of the representation of \mathbf{b} via (1.29) beyond its obvious complexity. For example, the Reynolds stresses are not necessarily functions solely of the mean rate of strain and rotation. Building on this point, the Reynolds stresses are nonlocal objects and representing them as functions of local quantities is insufficient. Nevertheless, the representation (1.29) for the eddy viscosity is appealing because the tensor basis is an integrity bases which guarantees that \mathbf{b} will satisfy Galilean invariance and remain a symmetric, anisotropic tensor. Although (1.29) is very general, it is also extremely complicated to treat. Pope itself, when proposing formulation (1.29), tuned the coefficients only for a particular two-dimensional flow case and declared the three-dimensional form is so analytically intractable as to be of no value. Indeed, for two dimensional flows there are only three linearly independent basis tensors \mathbf{T} and two non-zero independent invariants and therefore (1.29) is much easier to treat.

When in a certain eddy viscosity model $g^{(n)} \neq 0$ for $n > 1$, the model is said to be nonlinear, since it entails the product of two or more second-order tensors.

Nonlinear eddy viscosity models, although more computationally expensive, have the potential to represent additional flow physics, such as secondary flows and flows with mean streamline curvature. Many nonlinear models have been developed, including quadratic eddy viscosity models, yet in all of them only few -usually one more - of the $g^{(n)}$ coefficients are tuned due to the difficulty of treating (1.29) analytically.

1.4 Data Driven Turbulence Modeling

The term 'Data driven Turbulence Modelling' usually refers to the attempt to deal with the RANS models closure problem using machine learning techniques. In the following paragraphs, the neural networks basics will be introduced and it will be explained as well how in this work it was applied to turbulence modelling.

1.4.1 Neural Networks

Neural networks are a class of machine learning algorithms that have found applications in a wide variety of fields, including computer vision, natural language processing and gaming. Neural networks have shown to be particularly powerful in dealing with high dimensional data and modeling nonlinear and complex relationships [18]. Mathematically, a neural network defines a mapping $f : \mathbf{x} \rightarrow \mathbf{y}$ where \mathbf{x} is the input variable and \mathbf{y} is the output variable. The function f is defined as a composition of many different functions, which can be represented through a network structure. As an example, Figure 2 depicts a basic fully-connected feed-forward network that defines a mapping $f : \mathbb{R}^4 \rightarrow \mathbb{R}^3$ between the input layer (\mathbb{R}^4) and the output layer (\mathbb{R}^3) through two hidden layers.

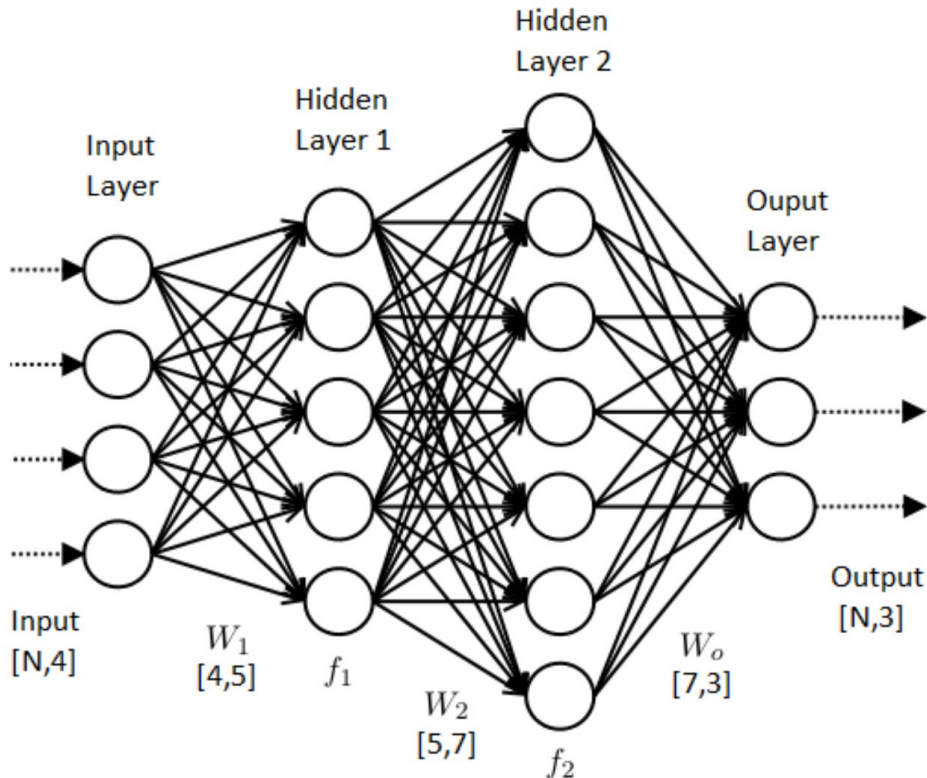


Figure 2: Diagram of a fully-connected feed-forward network with two hidden layers

The essential idea of the Neural Network can be summarized as follows for the one in Figure 2 :

1. The input layer here represents a 4-dimensional vector input $\mathbf{x} = [x_1, x_2, x_3, x_4]^T$ with each node in the layer standing for each component of the vector.
2. At the first hidden layer, the input \mathbf{x} gets transformed into a 5-dimensional output.

This is done in two steps:

- First, an affine transformation is performed at each node j in the hidden layer:

$$z_j^{(1)} = b_j^{(1)} + \sum_{i=1}^3 w_{ij}^{(1)} x_i \quad j = 1, 2, 3, 4, 5 \quad (1.32)$$

where $b_j^{(1)}$ is the bias value for node j and $w_{ij}^{(1)}$ is the weight value associated with the arrow linking node i in the input layer to node j in the first hidden layer.

- Second, a nonlinear transformation is performed according to a pre-specified activation function, ϕ as:

$$f_j^{(1)} = \phi(z_j^{(1)}) \quad (1.33)$$

An example of an activation function is the ReLU function $\phi(z) = \max(0, z)$

The two equations 1.33 and 1.32 can be represented altogether in vector notation as:

$$\mathbf{f}^{(1)} = \phi(\mathbf{W}^{(1)}\mathbf{x} + \mathbf{b}^{(1)}) \quad (1.34)$$

where ϕ operates element-wise and the weight matrix $\mathbf{W}^{(1)}$ and the bias vector $\mathbf{b}^{(1)}$ of the first hidden layer are defined by:

$$\mathbf{W}^{(1)} = \begin{bmatrix} w_{11}^{(1)} & w_{12}^{(1)} & w_{13}^{(1)} & w_{14}^{(1)} & w_{15}^{(1)} \\ w_{21}^{(1)} & w_{22}^{(1)} & w_{23}^{(1)} & w_{24}^{(1)} & w_{25}^{(1)} \\ w_{31}^{(1)} & w_{32}^{(1)} & w_{33}^{(1)} & w_{34}^{(1)} & w_{35}^{(1)} \\ w_{41}^{(1)} & w_{42}^{(1)} & w_{43}^{(1)} & w_{44}^{(1)} & w_{45}^{(1)} \end{bmatrix}^T \quad (1.35)$$

$$\mathbf{b}^{(1)} = [b_1^{(1)} \ b_2^{(1)} \ b_3^{(1)} \ b_4^{(1)} \ b_5^{(1)}]^T \quad (1.36)$$

3. Similarly, the second hidden layer takes $\mathbf{f}^{(1)}$ as input and produces a 7-dimensional output

$$\mathbf{f}^{(2)} = \phi(\mathbf{W}^{(2)}\mathbf{f}^{(1)} + \mathbf{b}^{(2)}) \quad (1.37)$$

4. Finally, the output layer returns the 2-dimensional output of the network:

$$\mathbf{y} = \phi_{out} \left(\mathbf{W}^{(out)} \mathbf{f}^{(2)} + \mathbf{b}^{(out)} \right) \quad (1.38)$$

The transformation ϕ_{out} is generally different from the nonlinear activations in the hidden layers. The choice of ϕ_{out} is guided by the output type and output distribution. For continuous outputs, ϕ_{out} can simply be the identity in which case the output is a linear combination of the final hidden layer.

The network just described is an example of a fully-connected, feed-forward network. It is fully-connected because every node in a hidden layer is connected with all the nodes in the previous and the following layers. It is feed-forward because the information flows in a forward direction from input to output; there is no feedback connection where the output of any layer is fed back into itself. A fully-connected, feed-forward network is the most basic type of neural network and is commonly referred to as a multilayer perceptron (MLP). Interestingly, it has been mathematically proven that MLPs are universal function approximators. The complexity of such a neural network increases with the number of hidden layers (depth of the network) and the number of nodes per hidden layer (width of the network).

Networks with more than one hidden layer are called deep neural networks.

1.4.2 Training of a Neural Network

The neural network expresses a functional form f^{NN} which is completely defined by a set of weights and biases denoted by \mathbf{W} . This functional form is in general an approximation to the true function f between the input and the output data. To find the best function approximation, one has to solve an optimization problem that minimizes the overall difference between $f(x)$ and $f^{NN}(x)$ for all x in the input dataset to obtain the model parameters. The process of finding the best model parameters (weights and biases) is called model training or learning. Once the model is trained, its performance is assessed on the validation dataset. Training and validation datasets are generated from the full dataset by splitting it into validation and training portions. Often, the split is done with 20% of the dataset used for validation and 80% used for training.

The overall difference between the true function and the approximation f^{NN} is quantified by a loss function. Typically, the choice of loss function is dependent on the particular problem. A general form of the total loss function is:

$$L(\mathbf{W}) = \frac{1}{N} \sum_{n=1}^N L_n(\mathbf{W}) \quad (1.39)$$

where N is the total number of data points used for training and L_n is the loss function defined for a single data point. A commonly used loss function is the mean squared error (MSE) loss:

$$L(W) = \frac{1}{N} \sum_{n=1}^N [(f(\mathbf{x}_n) - f^{NN}(\mathbf{x}_n)) \cdot (f(\mathbf{x}_n) - f^{NN}(\mathbf{x}_n))] \quad (1.40)$$

The stochastic gradient descent method (SGD) and its variants are used to iteratively find parameters W that minimize the loss function (1.39). In standard Gradient Descent, the model parameters W are updated according to:

$$W^k = W^{k-1} - \eta \nabla L(W^k) = W^{k-1} - \eta \left(\frac{1}{N} \sum_{n=1}^N \nabla L_n(W^k) \right) \quad (1.41)$$

where W^k are the model parameters at step k and η is the learning rate. This step repeats until convergence is achieved to within a user-specified tolerance.

Although neural networks have impressive approximation properties, training them requires the solution of a non-convex optimization problem. The classical gradient descent algorithm (GD) has significant trouble in finding a global minimum and can often get stuck in a shallow local minimum. The stochastic gradient descent algorithm provides a way of escaping from local minima in an effort to get closer to a global minimum. In each iteration of the stochastic gradient descent, the gradient $\nabla L(W)$ is approximated by the gradient at a single data point $\nabla L_n(W)$.

$$W^k = W^{k-1} - \eta \nabla L_n(W^k) \quad (1.42)$$

The algorithm sweeps through the training data until convergence to a local minimum is achieved. One full pass over the training data is called an epoch. Note that, generally, the training data is randomly shuffled at the beginning of each epoch. This algorithm is stochastic in the sense that the estimated gradient using a random data point is noisy whereas the gradient calculated on the entire training data is exact. In practice, Mini-Batch Stochastic Gradient Descent is employed, in which multiple data points are used in each iteration to approximate the gradient. The batch size M controls the number of random data points used per iteration. Hence at each iteration the model parameters are updated as:

$$W^k = W^{k-1} - \eta \nabla L_m(W^k) = W^{k-1} - \eta \left(\frac{1}{M} \sum_{n=1}^M \nabla L_n(W^k) \right) \quad (1.43)$$

The Mini-Batch Stochastic Gradient Descent is widely used since it combines the advantages of Gradient Descent and Stochastic Gradient Descent methods: it proves indeed less noisy than SGD and is more prone to overcome shallow local minimum compared to GD.

For parameter initialization, in most cases the initial weights are randomly sampled from a uniform

or normal distribution and the initial biases are set to 0.

Besides model parameters, the performance of a neural network changes with the external configuration of the network model and the training process. The external configuration refers to the number of hidden layers, the number of nodes per layer, the activation functions and the learning rate. These are called the hyperparameters of a model. The search for the best values of hyperparameters is called hyperparameter tuning. A grid search can be performed to search combinations of values on a grid of parameters in the hyperparameter space. A separate validation set that is different from the test set is used for model evaluation during the tuning process. Alternatively, a Bayesian optimization of the hyperparameters may also be performed.

1.4.3 The Tensor-Basis neural network

One possible way of applying machine learning techniques to turbulence modeling consists in using them to determine a suitable function that satisfies (1.28). In case neural networks are chosen, the most straightforward idea would be to use the nine distinct components of $\langle \mathbf{s} \rangle$ and $\langle \mathbf{r} \rangle$ as inputs of the network for many points of the physical space in order to obtain the corresponding \mathbf{b} components in output. Yet, in this case, it is not trivial for the neural network to learn some known physical properties of the nondimensional anisotropy tensor, such as the Galileian and rotational invariances. Indeed, when the coordinate frame is rotated, the input components of the mean strain rate and rotation rate tensors change and the anisotropy tensor in output is also rotated by the same angle. A 'physically correct' neural network, given the same input tensors at different rotation angles of the coordinates frames, should be able to predict in output the same anisotropy tensor rotated by the same angles. This result is not trivial to obtain with the intuitive network architecture described above. One possible way of achieving it would consist in training the network on a set of observations including the same input and output tensors rotated at different angles. In any case, however, the neural network would have to learn the invariance properties of the output tensor on herself.

A special network architecture, which will be referred to as the tensor basis neural network (TBNN), was proposed in 2016 by Julia Ling [9], in order to directly enforce invariance properties on the output anisotropy tensor. The key was to design a network architecture to match equation (1.29). In this network, two input layers are present: the invariants input layer and the tensor basis input layer. The invariants input layer is formed by the five invariants $\lambda_1 \dots \lambda_5$ and is followed by a series of hidden layers. The final hidden layer has 10 nodes and represents the coefficients $g^{(n)}$ for $n=1, \dots, 10$ of (1.29). The tensor basis input layer is composed by the 10 invariant tensors $\mathbf{T}^{(n)}$ for $n=1, \dots, 10$ of (1.29). The

merge output layer takes the element-wise products of the final hidden layer and the basis tensors input layer and sums the results to give the final prediction for \mathbf{b} - which is the same as taking the dot product between the two layers. This innovative architecture ensures that (1.29) is satisfied, thereby guaranteeing the Galileian invariance of the network predictions. Indeed, since \mathbf{b} is expressed as a linear combination of 10 isotropic basis tensors, any tensor \mathbf{b} in output that satisfies (1.29) will automatically satisfy Galileian invariance.

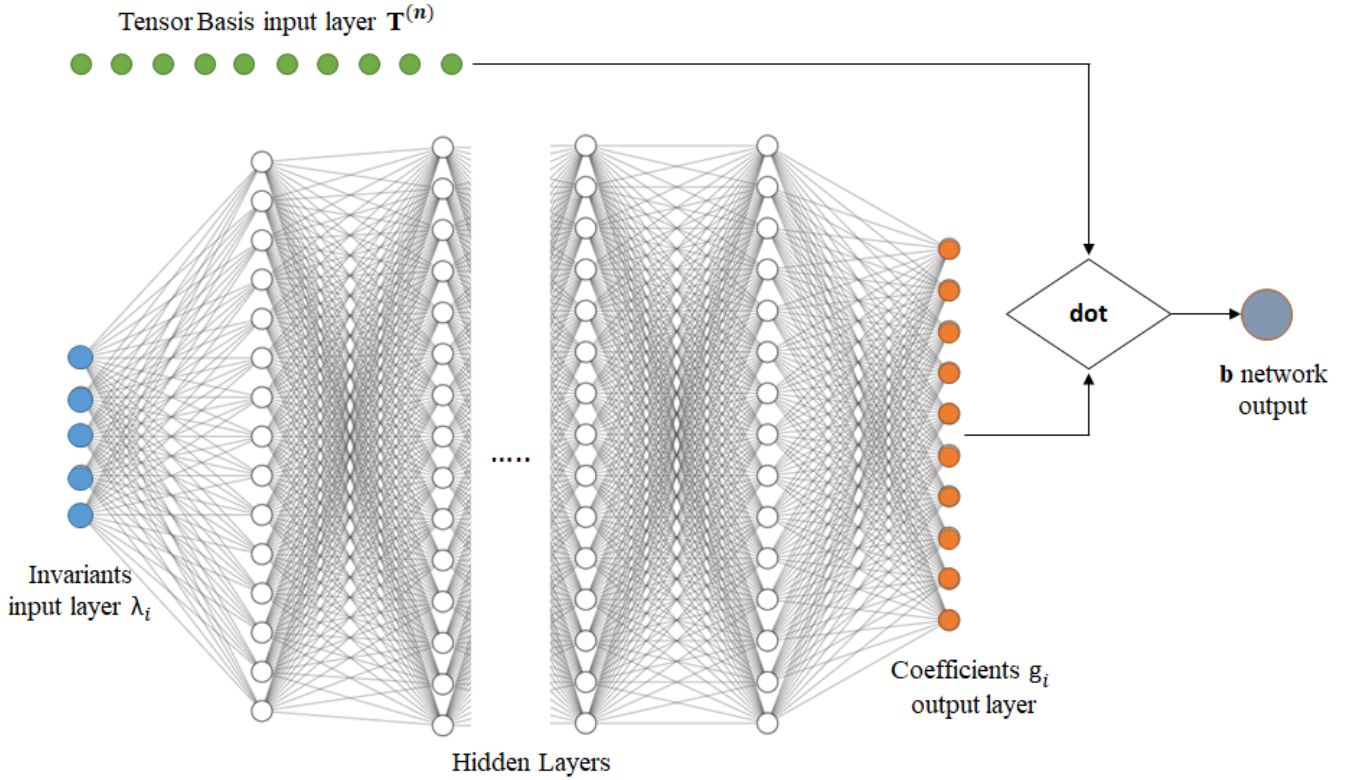


Figure 3: Schematic of the TBNN architecture

In brief, the key idea is to employ the network to predict the coefficients $g^{(n)}$ from the five invariants $\lambda_1 \dots \lambda_5$ and to compute \mathbf{b} accordingly as a linear combination of the tensor invariants basis derived from $\langle \mathbf{s} \rangle$ and $\langle \mathbf{r} \rangle$, rather than directly deriving \mathbf{b} from the two tensors' components. When Ling, Jones and Templeton used neural networks to predict the Reynolds stress anisotropy eigenvalues in 2016 [10], they reported a significant performance gain when a rotationally invariant input feature set was used. These results showed that embedding invariance properties into the machine learning model, as the network architecture described in Fig.(3) allows, is critical for achieving high performance predictions.

1.4.4 Description of the proposed approach

The procedure followed by Ling for employing the TBNN to improve Reynolds stresses prediction in RANS simulations can be summarized as follows:

1. First of all, a neural network with the architecture described in Fig.(3) is trained, validated and tested on a database of nine different flows for which high fidelity (DNS or well-resolved LES) as well as RANS results were available. The RANS data, obtained using the $k - \varepsilon$ model with the the LEVM (30) for the Reynolds stresses, were used as the input to the Neural Network. Therefore, each input observation consisted of the quantities (invariants and tensors basis) derived from $\langle \mathbf{s} \rangle$ and $\langle \mathbf{r} \rangle$ at a particular point in the space of the RANS solution. Hence each RANS simulations provides several observations (the \mathbf{x} in input to the network), theoretically one for each cell at which the numerical solution of the flow field is available. The high-fidelity data were used to provide the truth labels for the Reynolds stress anisotropy (the \mathbf{y} that the network tries to replicate) during model training and evaluation.

In brief, the network is trained to learn a function $f : \mathbf{x}(x, t)^{RANS} \rightarrow \mathbf{y}(x, t)^{DNS}$ -where \mathbf{x} is the set of neural network inputs - in this case the 5 invariants and the 10 basis tensors at a particular point in the space - and \mathbf{y} is the output of the network - namely the nondimensional anisotropy stress tensor \mathbf{b} at the corresponding point in space.

2. Once the neural network is trained, a desired RANS simulation is performed using a standard model - such as the $k - \varepsilon$ model with the LEVM - as one would normally do. The simulation can either be on a flow similar to one of the nine flows in the training database -which should theoretically yield better results - or on a completely different class of flow - in order to test the network model's generality.
3. When the RANS simulation has converged, the invariants λ_i and the basis tensors $\mathbf{T}^{(n)}$ are computed at each point of the numerical solution using the tensors $\langle \mathbf{s} \rangle^{RANS}$ and $\langle \mathbf{r} \rangle^{RANS}$ computed from the RANS solution flow fields $\langle \mathbf{U} \rangle^{RANS}$, k^{RANS} , ε^{RANS} . Here the suffix RANS refers to any quantity in output of the simulation run with the standard RANS model chosen.
4. For each point in the space of the numerical solution, the the invariants λ_i and the basis tensors $\mathbf{T}^{(n)}$ are fed to the previously trained network. The output will be the predicted anisotropy tensor \mathbf{b}^{TBNN} at the same point. The result will be an anisotropy stress tensor field $\mathbf{b}^{TBNN}(\mathbf{x}, t)$.
5. Starting from the previous RANS solution, a new RANS simulation is run by imposing the Reynolds stress anisotropy tensor field $\mathbf{b}^{TBNN}(\mathbf{x}, t)$ predicted by the TBNN as a constant in the

momentum equations and in the turbulent kinetic energy equation production term. Since the Reynolds stresses are prescribed in the simulation, there will be no need for a closure model like the LEVM.

6. The simulation is allowed to re-converge. At the end, the anisotropy stress tensor field will be the same as the one predicted from the neural network, since $\mathbf{b}^{TBNN}(\mathbf{x}, t)$ is held constant during the simulation. However the pressure and velocity fields will be different from the ones computed in the first simulation, since the LEVM model has been replaced by an imposed known field of the anisotropy tensor. It is fair to assume that, if $\mathbf{b}^{TBNN}(\mathbf{x}, t)$ proves a better approximation than $\mathbf{b}^{RANS}(\mathbf{x}, t)$ of the correct anisotropy stress tensor field, then the new pressure and velocity fields will be closer to the correct ones.

According to Ling's procedure, the neural network is used as a 'post-processing' tool to correct the anisotropy stress tensor field predicted by the standard RANS simulation. Once the corrected field is computed, it is injected in the RANS equations as a replacement of the LEVM model and the simulation is allowed to re-converge.

The idea of using machine learning techniques as a post-processing correction tool of a converged RANS solution has been applied in the majority of data driven turbulence modelling approaches [9],[10], [14], [15], [13]. From a very general perspective, these approaches differ in the machine learning method applied, in the quantity to predict - for example it can be the full anisotropy stress tensor, its eigenvalues, a constant of the standard model to tune.. - or on the inputs of the machine learning model. This entails that, since the neural network will be fed with quantities computed from a RANS simulation, it has to be trained on a database of RANS solutions.

The 'post-processing' approach, however, may present two key issues:

- Since the neural network is trained with quantities - the 5 invariants and the 10 basis tensors in the case of Ling approach - derived from a RANS simulation performed with a certain model X - such as $k - \varepsilon$, $k - \omega$, S-A and so on - theoretically the same network could not be applied to correct a simulation performed with a different model Y . Indeed, due to the inaccuracies of these models, the result of a RANS solution will be generally different when using different models, even though in most cases the difference is not huge. However, if the network is trained to learn a function $f : \mathbf{x}(x, t)^{RANS, X} \rightarrow \mathbf{y}(x, t)^{DNS}$ - where X is the RANS model used to compute the solution of the flows in the training database - it is not clear why the same function should yield good performances when correcting the fields computed with a different RANS model Y . This

entails that , theoretically, a different neural network should be trained for each RANS model and for each of its variants.

- In the case of Ling's article, a neural network is trained to learn a function $f : Q(\langle \mathbf{s} \rangle^{RANS}, \langle \mathbf{r} \rangle^{RANS}) \rightarrow \mathbf{b}(x, t)^{DNS}$ where Q is the set of procedures to transform $\langle \mathbf{s} \rangle^{RANS}$ and $\langle \mathbf{r} \rangle^{RANS}$ into the correct inputs of the neural network. This attempts to reproduce the function $b_{ij} = b_{ij}(\langle \mathbf{s} \rangle, \langle \mathbf{r} \rangle)$ whose validity is assumed in every eddy-viscosity model. However, this relation holds for the 'true' or 'correct' fields, like the ones computed with an high-fidelity DNS simulation.

In other words, relation (1.28) could be rewritten as : $b_{ij}^{DNS} = f(\langle \mathbf{s} \rangle^{DNS}, \langle \mathbf{r} \rangle^{DNS})$ and this relations, despite the limitations of its validity, has been taken as the starting point for the developing of the most popular RANS closure models. However, there is no physical hint that the nondimensional stress anisotropy tensor should depend on the velocity gradients computed via a RANS model which, in most cases, differ from the 'real' DNS ones. Hence a neural network trained to learn a function $f : Q(\langle \mathbf{s} \rangle^{RANS}, \langle \mathbf{r} \rangle^{RANS}) \rightarrow \mathbf{b}(x, t)^{DNS}$ will not only have to learn how to relate \mathbf{b} to velocity gradients but also how to correct the RANS inputs.

In this work, a different approach is followed in the attempt to overcome the previous two issues. It can be summarized as follows:

1. First of all, a tensor basis neural network with the same architecture of the one described by Ling, will be validated and tested on a database of eight different flows for which high fidelity data(DNS or well-resolved LES) are available. The DNS $\langle \mathbf{s} \rangle$ and $\langle \mathbf{r} \rangle$ data -not the RANS ones- will be used as the input to the Neural Network for each cell at which the DNS solution of the flow field is available. The high-fidelity data will again be used to provide the truth labels for the Reynolds stress anisotropy (the \mathbf{y} that the network tries to replicate) during model training and evaluation.

Hence, the network will be trained to learn a function $f : \mathbf{x}(x, t)^{DNS} \rightarrow \mathbf{y}(x, t)^{DNS}$ -where \mathbf{x} is the set of neural network inputs - in this case the 5 invariants and the 10 basis tensors at a particular point in the space - and \mathbf{y} is the output of the network - namely the nondimensional anisotropy stress tensor \mathbf{b} at the corresponding point in space.

2. A RANS simulation with a chosen model - for example the $k - \varepsilon$ one - will be run, but the LEVM closure (30) will be replaced by the pre-trained neural network. Hence, instead of using the network as a post-processing tool called at the end of a RANS simulation to correct the obtained anisotropy stress tensor field, it will be called at each iteration of the CFD solver to

relate \mathbf{b} to velocity gradients. Therefore, theoretically, at the end of the simulation the velocity gradients and the anisotropy stress tensor will satisfy the network function learned from DNS data. A scheme of the idea is described in the following Fig.(4b) for a general $k - \varepsilon$ explicit RANS solver.

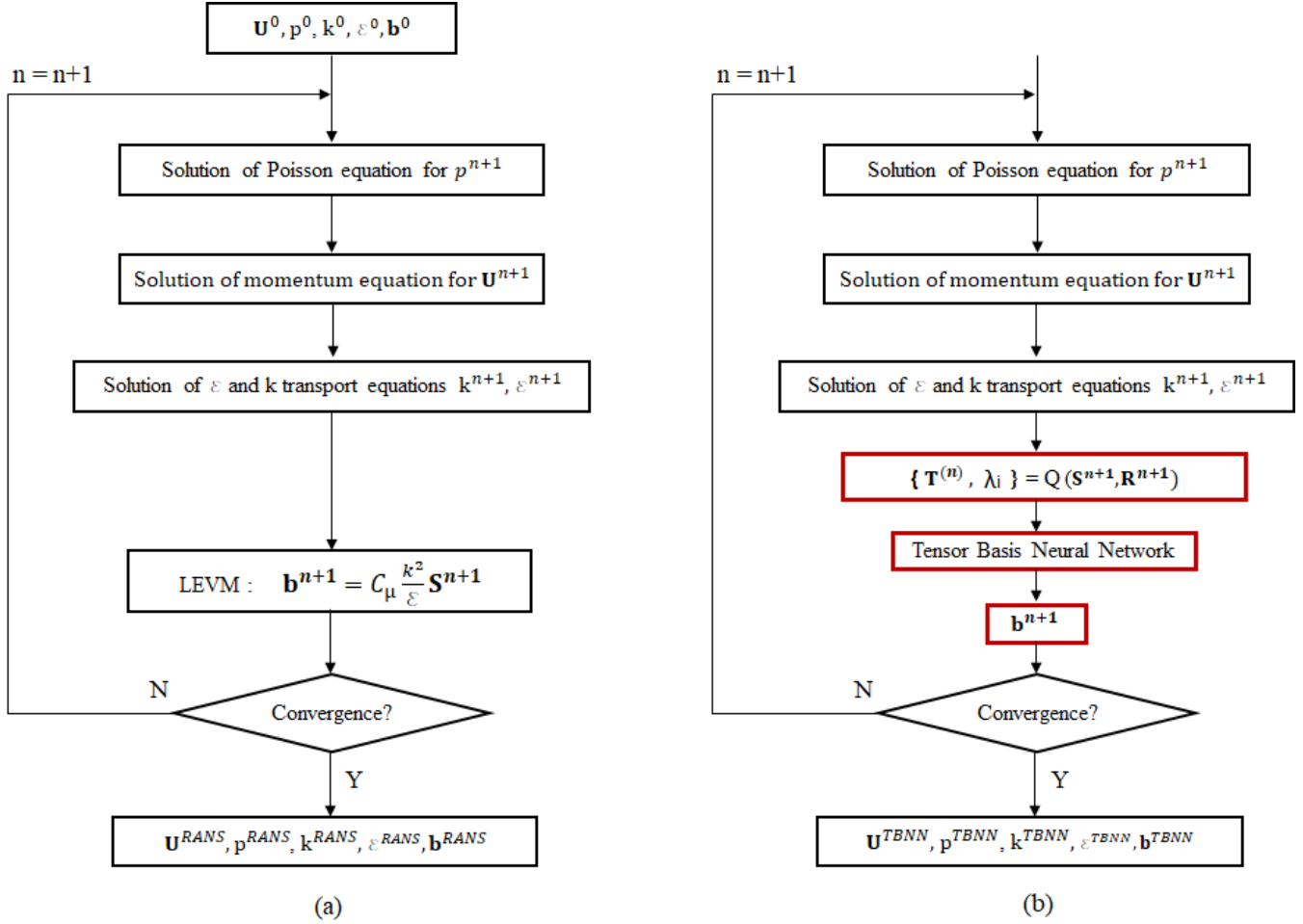


Figure 4: Comparison of a standard RANS solver with the proposed approach

It is interesting to notice that this approach addresses both the issues pointed above. Firstly, the neural network is trained to learn a relationship between the 'true' velocity gradients and the 'true' anisotropy stress tensor $f : Q(\langle \mathbf{s} \rangle^{DNS}, \langle \mathbf{r} \rangle^{DNS}) \rightarrow \mathbf{b}(x, t)^{DNS}$ as (1.29) and therefore it is trained to replicate exactly (1.29). Secondly, since the network is trained using DNS data, it could theoretically be used in all RANS models as a replacement to the LEVM. As a consequence, there will be no need to train a different neural network for each different RANS method and for each of its variants, thus improving considerably the generality of the method.

Lastly, it is crucial to notice that the replacement of the LEVM with the neural network would not entail a significant increase in the computational power when performing the simulation. Indeed,

the prediction time of the trained-network is negligible and comparable to the application of the LEVM - it mostly consists of matrix multiplications in cascade as explained in (1.34)- and also the additional task of computing the inputs of the network from the mean strain rate and rotation rate tensors basically consist a series of matrices multiplications. Another interesting aspect to keep into consideration is that the simulation procedure described in Fig.(4b) could be started from a previously converged RANS solution to speed the convergence of the method.

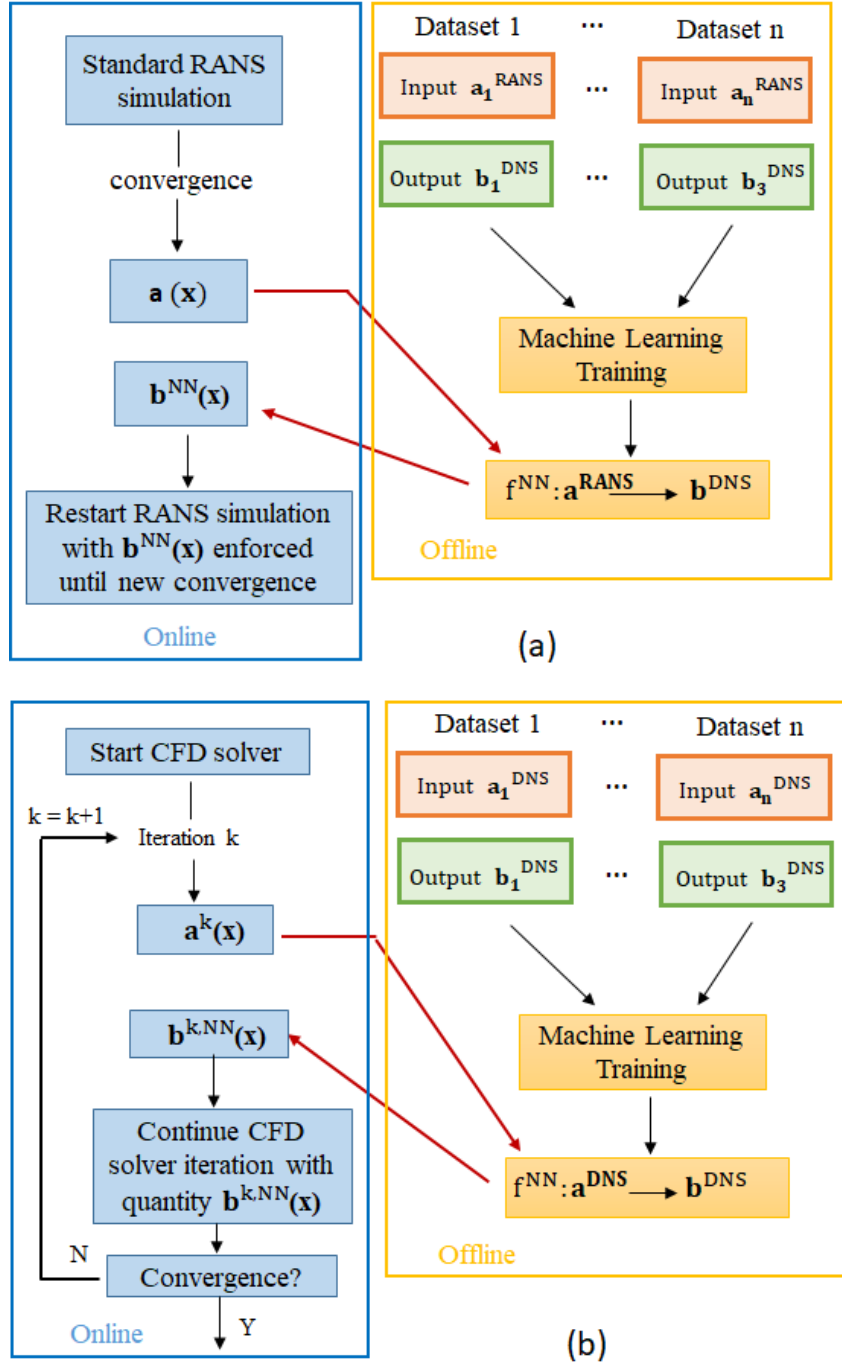


Figure 5: Standard data driven turbulence modelling approach (a) and proposed method (b)

Chapter 2

IMPLEMENTATION OF THE METHOD

2.1 Development of a RANS CFD Solver

In order to test the data driven turbulence modelling method described in the previous section, it is firstly necessary to develop a standard RANS solver. Once validated, it will be possible to modify the solver to embed the pre-trained neural network as a replacement of the LEVM. Hence, in the following sections, a detailed explanation of the steps employed to code the solver will be given. The goal of the code is to solve the set of RANS partial differential equations governing the evolution of turbulent flows, which will be later listed.

When writing a CFD solver, three main approaches are possible: finite difference method (FDM), finite elements method (FEM) and finite volume method (FVM) [37]. They all consist of different methods to solve a set of partial or ordinary differential equations on a discretized geometry of the chosen problem. Here, the finite volume method is chosen. The choice is motivated by the fact that the solver will be applied to cartesian, structured 2D geometries, for which the FVM proves to be the easiest one to implement. With the term *structured mesh* or *structured grid*, we refer to discretization of the physical space of the problem into geometrical entities characterized by regular connectivity, so that the inner nodes have the same number of elements around them and the mesh geometry can always be mapped into an 'equivalent' rectangular one. This is shown in the following Fig(6). The possible element choices are quadrilateral in 2D and hexahedra in 3D.

In the FVM, the values of the unknown variables are calculated at discrete places on a meshed geometry. "Finite volume" refers to the small volume surrounding each node point on a mesh. In the finite volume method, volume integrals in a partial differential equation that contain a divergence term are converted to surface integrals, using the divergence theorem. These terms are then evaluated as fluxes

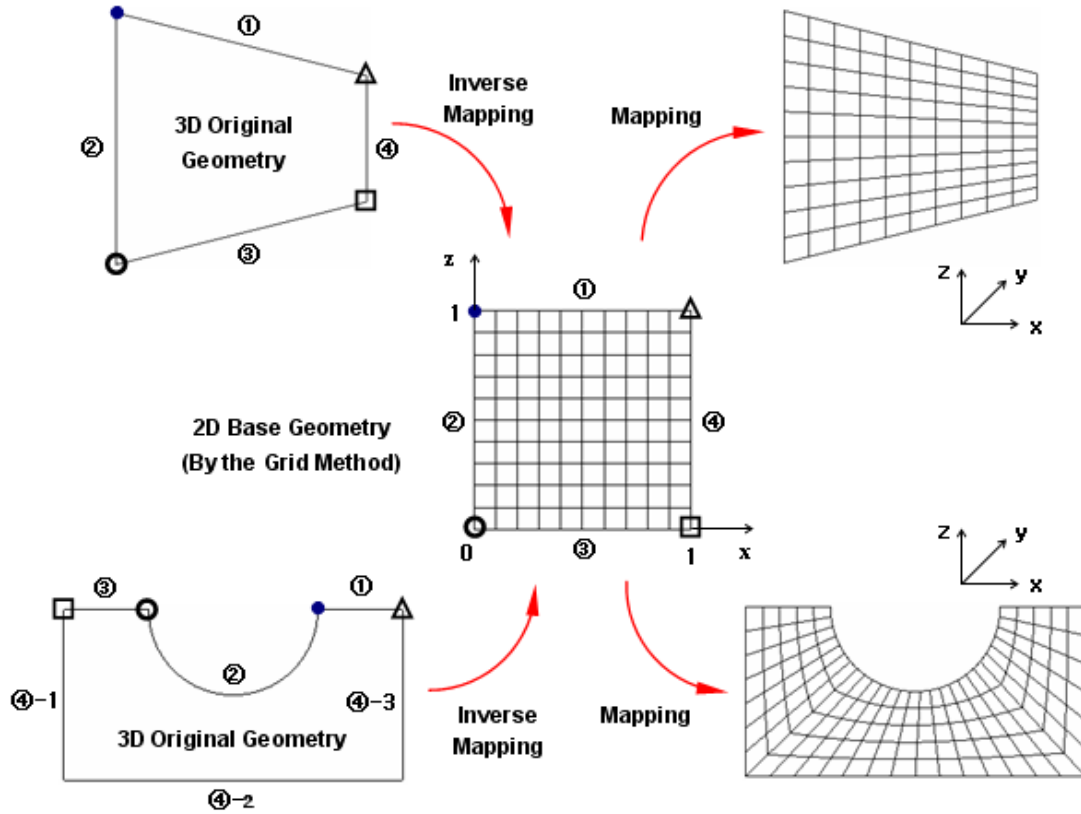


Figure 6: Structured meshes

at the surfaces of each finite volume. Because the flux entering a given volume is identical to that leaving the adjacent volume, these methods are conservative. Another advantage of the finite volume method is that it is easily formulated to allow for unstructured meshes. The method is used in many computational fluid dynamics packages [39].

As for the RANS turbulence model, a $k - \varepsilon$ with LEVM model is chosen. Hence, along with the average Navier-Stokes equations, two additional partial differential transport equations - for ε and k - will have to be solved. One of the main issues with the $k - \varepsilon$ family of models is that, when used for wall-bounded turbulent flows- they are not valid all the way to the physical walls. To work around this, three possible approaches can be followed [38]

- *Wall functions approach* : One approach consists in modelling the boundary layer using the renowned log-law correlation between the u component of the mean velocity field and the viscous distance y^+ from the wall- later defined - in the first cell adjacent to the wall. In practice, the RANS equations are not solved within the buffer layer and viscous sublayers - the regions of the flow closest to the wall - , yet rather a known relation is directly enforced in the first cell of the mesh covering this whole near-wall region. This approach is suitable for cases where wall-bounded effects are secondary, or the flow undergoes geometry-induced separation [29].

The benefit is that wall functions allow the use of a relatively coarse mesh in the near-wall region.

- *Enhanced wall treatments* This option combines a blended law-of-the wall and a two-layer zonal model. This case involves the full numerical resolution of the boundary layer in the viscous sublayer and in the buffer layer [30]. This approach is suitable for low-Reynolds flows or for flows in which wall-bounded effects are of high priority (adverse pressure gradients, aerodynamic drag, pressure drop, heat transfer, etc.) since it provides a more accurate description of the near wall region. This method requires a fine-near wall mesh capable of resolving the viscous sub-layer.
- *low-Reynolds models*: As in the Enhanced wall treatment approach, the boundary layer is numerically resolved up to the viscous sublayer. However, instead of using a two-layer zonal model, low-Reynolds models make use of different blending functions applied to the standard RANS equations. Those functions ensure that, far from the wall, the low-Re model is equivalent to the standard RANS model while, near the wall, the solution of the blended equations leads to the correct wall relations [26]. This method as well requires a fine-near wall mesh capable of resolving the viscous sub-layer.

An example of the typical grid resolutions required by the different approaches is shown in the following Fig.(7):

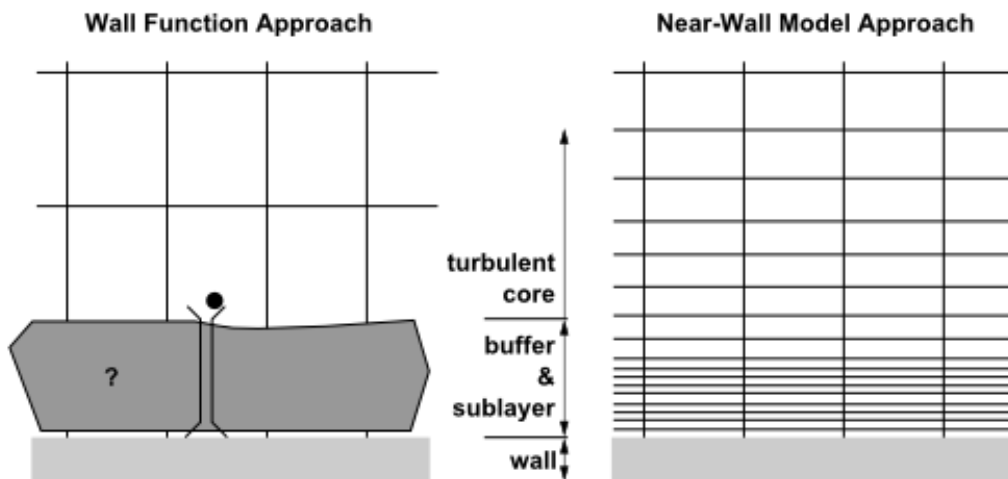


Figure 7: Grid resolutions for wall-functions and near-wall modeling approaches

Quantitatively, when a wall-functions approach is chosen the first cell adjacent to the wall must be placed at $y^+ > 30$ - namely beyond the buffer layer - , whereas when a wall-resolved method is used

the first cell must be placed well within the viscous sublayer - usually at $y^+ \simeq 1$. Since the flows for which the RANS solver will be used are at relatively small Reynolds number, a wall-functions approach would impose the definition of an excessively big first cell - since $y^+ = 30$ would be a non negligible fraction of the total size of the flow geometry. Therefore, a low-Reynolds turbulence model will be used; in particular the Abe-Kondoh-Nagano model [23] has been chosen since it yields good results in the case of the channel flow, to whom the RANS solver will be applied [27],[24].

Another relevant aspect to mention is that the RANS solver will be applied to steady turbulent flows, namely to flows in which the quantities do not vary with time. Notwithstanding, the solver will be built to solve the unsteady RANS equations - where the term $\frac{\partial}{\partial t}$ is present.

Indeed, a common practice for CFD steady solvers consists in solving the flow in time and in taking the solution at steady state - when the temporal change of the variables falls below a certain threshold value. This approach is analogue to the one that will be used to solve the discrete Poisson Equation for the effective pressure, as explained in the following sections.

2.1.1 Nondimensionalization of the governing equations

For a 2D RANS Abe-Kondoh-Nagano low-Re $k - \varepsilon$ model solver for incompressible flows, the set of governing equations in conservative form to solve is the following [37]:

$$\left\{ \begin{array}{l} \frac{\partial u}{\partial x} + \frac{\partial v}{\partial y} = 0 \\ \frac{\partial u}{\partial t} + \frac{\partial(u^2)}{\partial x} + \frac{\partial(uv)}{\partial y} + \frac{1}{\rho} \frac{\partial p}{\partial x} + \frac{2}{3} \frac{\partial k}{\partial x} = \nu \left(\frac{\partial^2 u}{\partial x^2} + \frac{\partial^2 u}{\partial y^2} \right) - \left(\frac{\partial a_{xx}}{\partial x} + \frac{\partial a_{xy}}{\partial y} \right) \\ \frac{\partial v}{\partial t} + \frac{\partial(uv)}{\partial x} + \frac{\partial(v^2)}{\partial y} + \frac{1}{\rho} \frac{\partial p}{\partial y} + \frac{2}{3} \frac{\partial k}{\partial y} = \nu \left(\frac{\partial^2 v}{\partial x^2} + \frac{\partial^2 v}{\partial y^2} \right) - \left(\frac{\partial a_{xy}}{\partial x} + \frac{\partial a_{yy}}{\partial y} \right) \\ \frac{\partial k}{\partial t} + \frac{\partial(uk)}{\partial x} + \frac{\partial(vk)}{\partial y} = \frac{\partial}{\partial x} \left[\left(\nu + \frac{\nu_T}{\sigma_k} \right) \frac{\partial k}{\partial x} \right] + \frac{\partial}{\partial y} \left[\left(\nu + \frac{\nu_T}{\sigma_k} \right) \frac{\partial k}{\partial y} \right] + P - \varepsilon \\ \frac{\partial \varepsilon}{\partial t} + \frac{\partial(u\varepsilon)}{\partial x} + \frac{\partial(v\varepsilon)}{\partial y} = \frac{\partial}{\partial x} \left[\left(\nu + \frac{\nu_T}{\sigma_\varepsilon} \right) \frac{\partial \varepsilon}{\partial x} \right] + \frac{\partial}{\partial y} \left[\left(\nu + \frac{\nu_T}{\sigma_\varepsilon} \right) \frac{\partial \varepsilon}{\partial y} \right] + f_1 C_{\varepsilon 1} \frac{P\varepsilon}{k} - f_2 C_{\varepsilon 2} \frac{\varepsilon^2}{k} \\ a_{xx} = -2C_\mu f_\mu \frac{k^2}{\varepsilon} \frac{\partial u}{\partial x} \\ a_{xy} = -C_\mu f_\mu \frac{k^2}{\varepsilon} \left(\frac{\partial u}{\partial y} + \frac{\partial v}{\partial x} \right) \\ a_{yy} = -2C_\mu f_\mu \frac{k^2}{\varepsilon} \frac{\partial v}{\partial y} \end{array} \right. \quad (2.1)$$

where:

- The first equation corresponds to the conservation of mass, or continuity equation.
- The second and third equations correspond respectively to the x and y momentum equations.
- The fourth equation corresponds to the transport equation for the turbulent kinetic energy k .
- The fifth equation corresponds to the transport equation for the turbulent kinetic energy dissipation rate ε .
- The last three equations correspond to the Linear Eddy Viscosity Model applied for each non-zero component of the anisotropy stress tensor.
- The correction factors of the Abe-Kondoh-Nagano low-Re $k - \varepsilon$ model are [25]:

$$f_1 = 1 \quad f_2 = \left(1 - e^{-\frac{y^k}{3.1}}\right) \left[1 - 0.3 e^{-\left(\frac{Re_T}{6.5}\right)^2}\right] \quad f_\mu = \left(1 - e^{-\frac{y^k}{14}}\right)^2 \left[1 + \frac{5}{Re_T^{3/4}} e^{-\left(\frac{Re_T}{200}\right)^2}\right]$$

with:

$$Re_T = \frac{k^2}{\nu \varepsilon} \quad y^k = \frac{y \varepsilon^{1/4}}{\nu^{3/4}}$$

where y is the distance to the nearest wall.

- The model constants are [25]:

$$C_\mu = 0.09 \quad C_{\varepsilon 1} = 1.5 \quad C_{\varepsilon 2} = 1.9 \quad \sigma_k = 1.4 \quad \sigma_\varepsilon = 1.4$$

- The terms u and v in (2.1) correspond the x and y component of the mean flow field $\langle \mathbf{U} \rangle$. The averaging operator $\langle \rangle$ has been omitted for the sake of brevity in all the equations.

Now, the system (2.1) is expressed in dimensional form and therefore the solution depends on the specific problem parameters - like the fluid viscosity or the geometry size. In order to obtain a general form for the solution of the flow, it is necessary to nondimensionalize the variables of the equations in (2.1).

As a consequence, the following dimensionless parameters are introduced:

$$\begin{aligned} u^* &= \frac{u}{U} & v^* &= \frac{v}{U} & p^* &= \frac{p}{\rho U^2} & k^* &= \frac{k}{U^2} & a_{ij}^* &= \frac{a_{ij}}{U^2} & P^* &= \frac{PL}{U^3} \\ x^* &= \frac{x}{L} & y^* &= \frac{y}{L} & t^* &= t \frac{U}{L} & \varepsilon^* &= \frac{\varepsilon L}{U^3} & \nu_T^* &= \frac{\nu_T}{\nu} \end{aligned} \quad (2.2)$$

where L is a characteristic length and U is a characteristic velocity of the specific problem considered.

By substituting (2.2) in the continuity equation of (2.1) one obtains:

$$\frac{\partial u^*}{\partial x^*} \frac{U}{L} + \frac{\partial v^*}{\partial y^*} \frac{U}{L} = 0$$

from which it follows immediately:

$$\frac{\partial u^*}{\partial x^*} + \frac{\partial v^*}{\partial y^*} = 0 \quad (2.3)$$

which corresponds to the non-dimensional continuity equation.

Instead, by substituting (2.2) in the momentum equation along x of (2.1) one obtains:

$$\frac{U^2}{L} \frac{\partial u^*}{\partial t^*} + \frac{U^2}{L} \frac{\partial(u^{*2})}{\partial x^*} + \frac{U^2}{L} \frac{\partial(u^*v^*)}{\partial y^*} + \frac{\rho U^2}{L} \frac{1}{\rho} \frac{\partial p^*}{\partial x^*} + \frac{2}{3} \frac{U^2}{L} \frac{\partial k^*}{\partial x^*} = \nu \left(\frac{U}{L^2} \frac{\partial^2 u^*}{\partial x^{*2}} + \frac{U}{L^2} \frac{\partial^2 u^*}{\partial y^{*2}} \right) - \frac{U^2}{L} \left(\frac{\partial a_{xx}^*}{\partial x} + \frac{\partial a_{xy}^*}{\partial y} \right) \quad (2.4)$$

Recalling that the Reynolds number is defined as:

$$Re = \frac{UL}{\nu} \quad (2.5)$$

if we divide (2.4) by U^2/L and substitute the expression (2.5) we obtain:

$$\frac{\partial u^*}{\partial t^*} + \frac{\partial(u^{*2})}{\partial x^*} + \frac{\partial(u^*v^*)}{\partial y^*} + \frac{\partial p^*}{\partial x^*} + \frac{2}{3} \frac{\partial k^*}{\partial x^*} = \frac{1}{Re} \left(\frac{\partial^2 u^*}{\partial x^{*2}} + \frac{\partial^2 u^*}{\partial y^{*2}} \right) - \left(\frac{\partial a_{xx}^*}{\partial x} + \frac{\partial a_{xy}^*}{\partial y} \right) \quad (2.6)$$

which corresponds to the non-dimensional momentum equation along x .

An analogous method is followed in order to nondimensionalize the momentum equation along y .

Indeed, by substituting (2.2) in the y momentum equation of (2.1) one obtains:

$$\frac{U^2}{L} \frac{\partial v^*}{\partial t^*} + \frac{U^2}{L} \frac{\partial(u^*v^*)}{\partial x^*} + \frac{U^2}{L} \frac{\partial(v^{*2})}{\partial y^*} + \frac{\rho U^2}{L} \frac{1}{\rho} \frac{\partial p^*}{\partial y^*} + \frac{2}{3} \frac{U^2}{L} \frac{\partial k^*}{\partial y^*} = \nu \left(\frac{U}{L^2} \frac{\partial^2 v^*}{\partial x^{*2}} + \frac{U}{L^2} \frac{\partial^2 v^*}{\partial y^{*2}} \right) - \frac{U^2}{L} \left(\frac{\partial a_{xy}^*}{\partial x} + \frac{\partial a_{yy}^*}{\partial y} \right) \quad (2.7)$$

By dividing (2.7) by U^2/L and substituting the expression (2.5) we obtain:

$$\frac{\partial v^*}{\partial t^*} + \frac{\partial(u^*v^*)}{\partial x^*} + \frac{\partial(v^{*2})}{\partial y^*} + \frac{\partial p^*}{\partial y^*} + \frac{2}{3} \frac{\partial k^*}{\partial y^*} = \frac{1}{Re} \left(\frac{\partial^2 v^*}{\partial x^{*2}} + \frac{\partial^2 v^*}{\partial y^{*2}} \right) - \left(\frac{\partial a_{xy}^*}{\partial x} + \frac{\partial a_{yy}^*}{\partial y} \right) \quad (2.8)$$

which corresponds to the non-dimensional Momentum Equation along y .

Now, if we substitute (2.2) in the k transport equation of (2.1) one obtains:

$$\frac{U^3}{L} \frac{\partial k^*}{\partial t^*} + \frac{U^3}{L} \frac{\partial(u^*k^*)}{\partial x^*} + \frac{U^3}{L} \frac{\partial(v^*k^*)}{\partial y^*} = \frac{\nu U^2}{L^2} \frac{\partial}{\partial x} \left[\left(1 + \frac{\nu_T^*}{\sigma_k} \right) \frac{\partial k^*}{\partial x^*} \right] + \frac{\nu U^2}{L^2} \frac{\partial}{\partial y} \left[\left(1 + \frac{\nu_T^*}{\sigma_k} \right) \frac{\partial k^*}{\partial y^*} \right] + \frac{U^3}{L} (P^* - \varepsilon^*) \quad (2.9)$$

If we divide (2.9) by U^3/L and substitute the expression (2.5) we obtain:

$$\frac{\partial k^*}{\partial t^*} + \frac{\partial(u^*k^*)}{\partial x^*} + \frac{\partial(v^*k^*)}{\partial y^*} = \frac{1}{Re} \frac{\partial}{\partial x} \left[\left(1 + \frac{\nu_T^*}{\sigma_k} \right) \frac{\partial k^*}{\partial x^*} \right] + \frac{1}{Re} \frac{\partial}{\partial y} \left[\left(1 + \frac{\nu_T^*}{\sigma_k} \right) \frac{\partial k^*}{\partial y^*} \right] + P^* - \varepsilon^* \quad (2.10)$$

An analogous method is followed in to nondimensionalize the ε transport equation in (2.1). Indeed, by substituting (2.2) in ε transport equation of (2.1) and dividing by U^4/L^2 one obtains:

$$\frac{\partial \varepsilon^*}{\partial t^*} + \frac{\partial(u^* \varepsilon^*)}{\partial x^*} + \frac{\partial(v^* \varepsilon^*)}{\partial y^*} = \frac{1}{Re} \frac{\partial}{\partial x} \left[\left(1 + \frac{\nu_T^*}{\sigma_\varepsilon} \right) \frac{\partial \varepsilon^*}{\partial x^*} \right] + \frac{1}{Re} \frac{\partial}{\partial y} \left[\left(1 + \frac{\nu_T^*}{\sigma_\varepsilon} \right) \frac{\partial \varepsilon^*}{\partial y^*} \right] + C_{\varepsilon 1} \frac{P^* \varepsilon^*}{k^*} - C_{\varepsilon 2} \frac{\varepsilon^{*2}}{k^*} \quad (2.11)$$

Finally, by substituting (2.2) in the LEVM model of (2.1) one obtains:

$$U^2 a_{ij}^* = -C_\mu \frac{k^{*2}}{\varepsilon^*} \frac{U^4}{U^3/L} \left(\frac{\partial u_i}{\partial x_j} + \frac{\partial u_j}{\partial x_i} \right) \frac{U}{L} \quad (2.12)$$

and by dividing (2.12) by U^2 we get to:

$$a_{ij}^* = -C_\mu \frac{k^{*2}}{\varepsilon^*} \left(\frac{\partial u_i}{\partial x_j} + \frac{\partial u_j}{\partial x_i} \right) \quad (2.13)$$

The last step consists in expressing Re_T and y^k of the Abe-Kondoh-Nagano model as a function of the nondimensional variables:

$$Re_T = \frac{1}{\nu} \frac{k^{*2}}{\varepsilon^*} \frac{U^4}{U^3/L} = Re \frac{k^{*2}}{\varepsilon^*} \quad y^k = \frac{y^k}{L} = (y^* \varepsilon^{*1/4}) L \left(\frac{U^3}{L} \right)^{1/4} \nu^{3/4} = (y^* \varepsilon^{*1/4}) Re^{3/4}$$

Hence, the conservative nondimensional form of the governing equations of the 2D RANS Abe-Kondoh-Nagano low-Re $k - \varepsilon$ model are:

$$\left\{ \begin{array}{l} \frac{\partial u^*}{\partial x^*} + \frac{\partial v^*}{\partial y^*} = 0 \\ \frac{\partial u^*}{\partial t^*} + \frac{\partial(u^{*2})}{\partial x^*} + \frac{\partial(u^* v^*)}{\partial y^*} + \frac{\partial p^*}{\partial x^*} + \frac{2}{3} \frac{\partial k^*}{\partial x^*} = \frac{1}{Re} \left(\frac{\partial^2 u^*}{\partial x^{*2}} + \frac{\partial^2 u^*}{\partial y^{*2}} \right) - \left(\frac{\partial a_{xx}^*}{\partial x} + \frac{\partial a_{xy}^*}{\partial y} \right) \\ \frac{\partial v^*}{\partial t^*} + \frac{\partial(u^* v^*)}{\partial x^*} + \frac{\partial(v^{*2})}{\partial y^*} + \frac{\partial p^*}{\partial y^*} + \frac{2}{3} \frac{\partial k^*}{\partial y^*} = \frac{1}{Re} \left(\frac{\partial^2 v^*}{\partial x^{*2}} + \frac{\partial^2 v^*}{\partial y^{*2}} \right) - \left(\frac{\partial a_{xy}^*}{\partial x} + \frac{\partial a_{yy}^*}{\partial y} \right) \\ \frac{\partial k^*}{\partial t^*} + \frac{\partial(u^* k^*)}{\partial x^*} + \frac{\partial(v^* k^*)}{\partial y^*} = \frac{1}{Re} \frac{\partial}{\partial x} \left[\left(1 + \frac{\nu_T^*}{\sigma_k} \right) \frac{\partial k^*}{\partial x^*} \right] + \frac{1}{Re} \frac{\partial}{\partial y} \left[\left(1 + \frac{\nu_T^*}{\sigma_k} \right) \frac{\partial k^*}{\partial y^*} \right] + P^* - \varepsilon^* \\ \frac{\partial \varepsilon^*}{\partial t^*} + \frac{\partial(u^* \varepsilon^*)}{\partial x^*} + \frac{\partial(v^* \varepsilon^*)}{\partial y^*} = \frac{1}{Re} \frac{\partial}{\partial x} \left[\left(1 + \frac{\nu_T^*}{\sigma_\varepsilon} \right) \frac{\partial \varepsilon^*}{\partial x^*} \right] + \frac{1}{Re} \frac{\partial}{\partial y} \left[\left(1 + \frac{\nu_T^*}{\sigma_\varepsilon} \right) \frac{\partial \varepsilon^*}{\partial y^*} \right] + C_{\varepsilon 1} \frac{P^* \varepsilon^*}{k^*} - C_{\varepsilon 2} \frac{\varepsilon^{*2}}{k^*} \\ a_{xx}^* = -2C_\mu f_\mu \frac{k^{*2}}{\varepsilon^*} \frac{\partial u^*}{\partial x^*} \\ a_{xy}^* = -C_\mu f_\mu \frac{k^{*2}}{\varepsilon^*} \left(\frac{\partial u^*}{\partial y^*} + \frac{\partial v^*}{\partial x^*} \right) \\ a_{yy}^* = -2C_\mu f_\mu \frac{k^{*2}}{\varepsilon^*} \frac{\partial v^*}{\partial y^*} \end{array} \right. \quad (2.14)$$

2.1.2 The Marker and Cell (MAC) method

In order to solve numerically the equations governing the Initial and Boundary value problem described above, the unsteady explicit MAC (Marker in Cell) method is used. The method was firstly introduced by Harlow and Welch in in order to numerically solve the time-dependent flow of an incompressible liquid whose boundary is partly confined and partly free [21].

A *staggered arrangement* is chosen for the computation of the variables on the grid [37]. In this grid's arrangement the pressure, the velocity components and the turbulence quantities are not stored on the same grid points: in this case, the pressure is computed at the center of the cells, v is computed in correspondence of the upper edge of the cell, u in correspondence of the right edge and the turbulence quantities, -such as k , ε - are stored at the cell vertex [28]. The production terms in k and ε transport equations are evaluated at the same locations of k , ε , namely the cell vertices, where the strain and rotation rate tensors are computed and the eddy viscosity calculated from k and ε at these cell vertices are directly used to calculate the turbulent stress tensor. In this way, the Navier-Stokes equations and the k and ε transport equations are coupled as closely as possible, as mentioned in [28].

Whenever the value of a variable is required in a grid location different from the one where the variable is computed and stored, simple interpolation is used as it will be later shown. The main advantage of such an arrangement is that it helps avoiding some types of convergence and oscillation problems in the velocity and pressure fields [39] and guarantees a strong coupling between the Navier-Stokes equations and the k and ε transport equations [28].

In the following, when referring to quantities computed at the edges of the Control Volumes, fractional indices are used. However, when writing the code, the velocity and turbulent quantities' values will be stored with indices corresponding to the position of the center of the cell. Since when plotting the solution both the pressure and velocity field must be referred to the same grid locations, the value of u and v at the center of each cell is computed by interpolation between consecutive edges. The following Fig. (8) shows how the staggered arrangement is implemented.

In the following, we will refer only to nondimensional quantities for pressure and velocity. In order to ease the writing, the superscript $*$ will be omitted.

In the following discussion, we will refer to the column index as i and to the row index as j . The center of each cell corresponds to an indices pair (i,j) , so that we will refer to the pressure at the center of the (j,i) cell as p_{ji} . For the velocity components and the turbulent quantities, the fractional index notation will be used, as shown in Fig (8a). The MAC method is explicit [20] this means that the velocity field at time t^{n+1} is a function of variables already computed at time t^n . The method makes use of

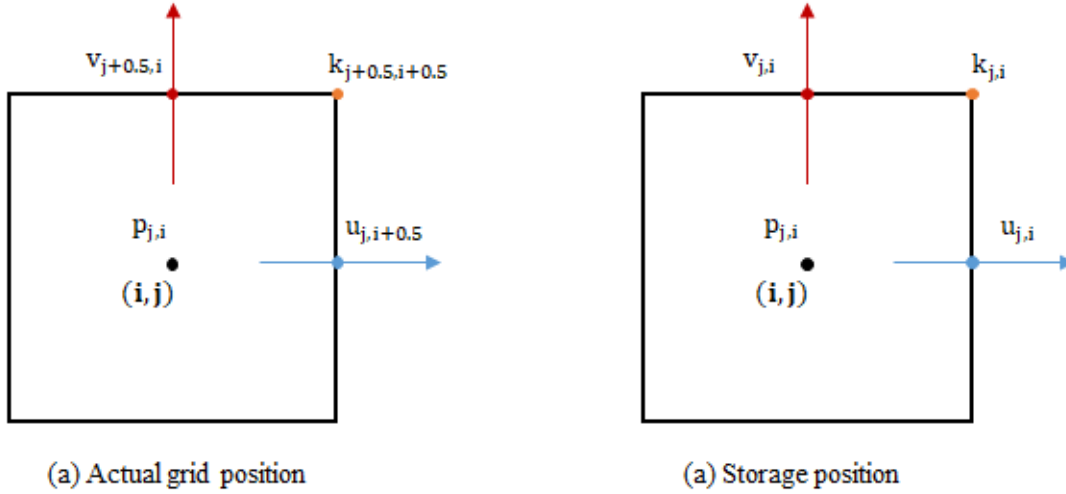


Figure 8: Staggered Arrangement

finite volumes approximations applied to the full Navier-Stokes equations and the numerical scheme is Forward-in-Time Central-in-Space [21].

2.1.3 Discretization of the equations

In this section, the Navier-stokes momentum equations and the k and ε transport equations are discretized according to the Finite Volume Method. The discretization procedure will be carried out on cartesian, non uniform grid. This means that the grid is composed of adjacent rectangles which may have different dimensions Δx and Δy . For the continuity equation, a special treatment is required. This will be examined in the following section. Before starting with the discretization, it is useful to remind the expression for the centered discretization of the first derivative on a non-uniform grid:

$$\left(\frac{\partial \phi}{\partial x}\right)_i \simeq \phi_{i+1} \frac{\Delta x_i}{(\Delta x_i + \Delta x_{i+1})(\Delta x_i)} + \phi_i \frac{\Delta x_{i+1} - \Delta x_i}{\Delta x_{i+1} \Delta x_i} - \phi_{i-1} \frac{\Delta x_{i+1}}{(\Delta x_i + \Delta x_{i+1})(\Delta x_{i+1})} \quad (2.15)$$

where $\Delta x_i = x_i - x_{i-1}$, $\Delta x_{i+1} = x_{i+1} - x_i$ and ϕ_i corresponds to the numerical approximation of variable ϕ at position x_i of the discretization grid, as shown in the following Fig (9)

In case of uniform grid $\Delta x_i = \Delta x_{i+1} = \Delta x$, equation (2.16) is reduced to :

$$\left(\frac{\partial \phi}{\partial x}\right)_i \simeq \frac{\phi_{i+1} - \phi_{i-1}}{2\Delta x} \quad (2.16)$$

Another important aspect to explain is the linear interpolation. Indeed, since a staggered arrangement is used, it is possible that the value of a variable is needed at a position in the grid at which it is not defined. For example, it may happen that the discretization procedure requires the value of velocity components at the cell center, whereas they are defined at the cell faces. In all these cases, a

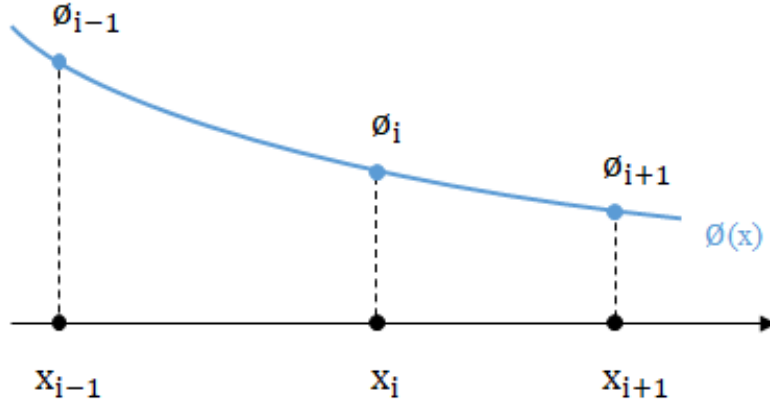


Figure 9: Centered approximation of the first derivative

linear interpolation will be applied to determine the value of the variable at the desired position. For example, referring to Fig (9), if we imagine that the variable ϕ is defined only at the grid points x_{i-1} and x_{i+1} yet its value is needed at position x_i , the value ϕ_i can be approximated as:

$$\phi_i \simeq \phi_{i+1} \frac{\Delta x_i}{(\Delta x_i + \Delta x_{i+1})} + \phi_{i-1} \frac{\Delta x_{i+1}}{(\Delta x_i + \Delta x_{i+1})} \quad (2.17)$$

Lastly, a relevant aspect to notice is that, due to the staggered arrangement, the control volumes of the different variables are generally different. This will be shown in the following sections.

2.1.4 X momentum equation

The nondimensional Navier-Stokes momentum equation in x direction, already derived in (2.14), is :

$$\frac{\partial u}{\partial t} + \frac{\partial(u^2)}{\partial x} + \frac{\partial(uv)}{\partial y} + \frac{\partial p}{\partial x} + \frac{2}{3} \frac{\partial k}{\partial x} = \frac{1}{Re} \left(\frac{\partial^2 u}{\partial x^2} + \frac{\partial^2 u}{\partial y^2} \right) - \left(\frac{\partial a_{xx}}{\partial x} + \frac{\partial a_{xy}}{\partial y} \right) \quad (2.18)$$

where, in order to ease the writing, the superscript * has been omitted.

Integrating (2.18) over the u -control volume shown in Fig.(10) one has [20]:

$$\iint \frac{\partial u}{\partial t} dx dy + \iint \frac{\partial}{\partial x} \left(u^2 + a_{xx} - \frac{1}{Re} \frac{\partial u}{\partial x} \right) dx dy + \iint \frac{\partial}{\partial y} \left(uv + a_{xy} - \frac{1}{Re} \frac{\partial u}{\partial y} \right) dx dy + \iint \frac{\partial p_{eff}}{\partial x} dx dy = 0 \quad (2.19)$$

where we have substituted $p_{eff} = p + 2k/3$.

Application of the Green theorem to the above expression and use of MAC method for the time discretization leads to:

$$\frac{\Delta x \Delta y}{\Delta t} (u_{j,i+\frac{1}{2}}^{n+1} - u^n) + (E_{j,i+1}^x - E_{j,i}^x) \Delta y + \left(F_{j+\frac{1}{2},i+\frac{1}{2}}^x - F_{j-\frac{1}{2},i+\frac{1}{2}}^x \right) \Delta x + (p_{eff,j,i+1}^{n+1} - p_{eff,j,i}^{n+1}) \Delta y = 0 \quad (2.20)$$

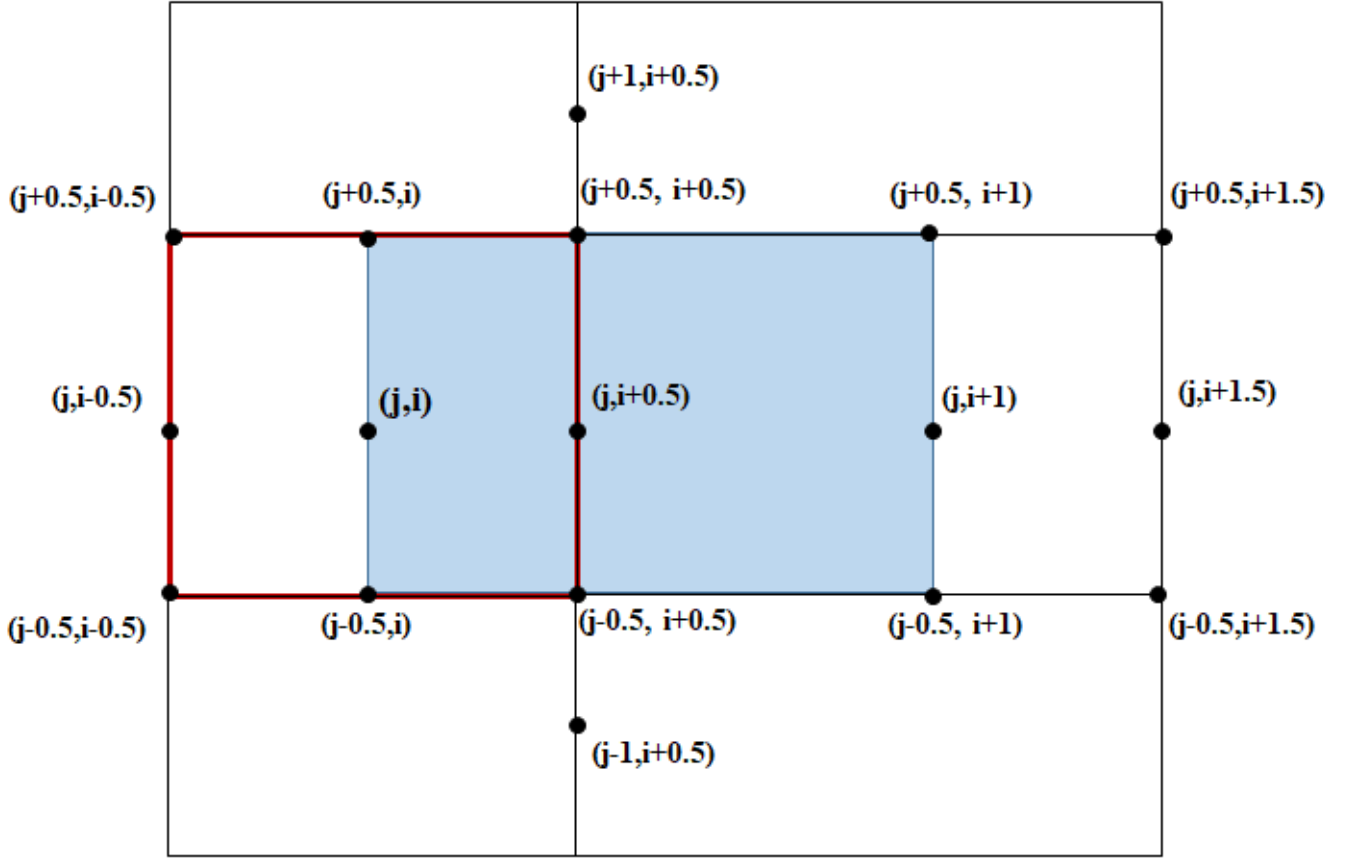


Figure 10: Control volume for the x-momentum equation

or equivalently :

$$\frac{(u_{j,i+\frac{1}{2}}^{n+1} - u_{j,i+\frac{1}{2}}^n)}{\Delta t} + \frac{(E_{j,i+1}^x - E_{j,i}^x)}{\Delta x} + \frac{(F_{j+\frac{1}{2},i+\frac{1}{2}}^x - F_{j-\frac{1}{2},i+\frac{1}{2}}^x)}{\Delta y} + \frac{(p_{eff,j,i+1}^{n+1} - p_{eff,j,i}^{n+1})}{\Delta x} = 0 \quad (2.21)$$

where $\Delta x = x_{j,i+1} - x_{j,i}$ and $\Delta y = y_{j+\frac{1}{2},i+\frac{1}{2}} - y_{j-\frac{1}{2},i+\frac{1}{2}}$ are the dimensions of the (j,i) x-momentum Control Volume , $\Delta t = t^{n+1} - t^n$, E^x and F^x are the axial and transversal fluxes of x-momentum defined as:

$$E^x = u^2 + a_{xx} - \frac{1}{Re} \frac{\partial u}{\partial x} \quad F^x = uv + a_{xy} - \frac{1}{Re} \frac{\partial u}{\partial y} \quad (2.22)$$

whose discretized forms for (2.20) can be obtained using linear interpolations (2.17) and the expression for the first derivative (2.16):

$$\begin{aligned}
 E_{j,i+1}^x &= \left(\frac{u_{j,i+\frac{3}{2}}^n + u_{j,i+\frac{1}{2}}^n}{2} \right)^2 + \left(\frac{a_{xx,j+\frac{1}{2},i+\frac{1}{2}}^n + a_{xx,j-\frac{1}{2},i+\frac{1}{2}}^n + a_{xx,j+\frac{1}{2},i+\frac{3}{2}}^n + a_{xx,j-\frac{1}{2},i+\frac{3}{2}}^n}{4} \right) - \frac{1}{Re} \left(\frac{u_{j,i+\frac{3}{2}}^n - u_{j,i+\frac{1}{2}}^n}{x_{j,i+\frac{3}{2}} - x_{j,i+\frac{1}{2}}} \right) \\
 E_{j,i}^x &= \left(\frac{u_{j,i+\frac{1}{2}}^n + u_{j,i-\frac{1}{2}}^n}{2} \right)^2 + \left(\frac{a_{xx,j+\frac{1}{2},i+\frac{1}{2}}^n + a_{xx,j-\frac{1}{2},i+\frac{1}{2}}^n + a_{xx,j+\frac{1}{2},i-\frac{1}{2}}^n + a_{xx,j-\frac{1}{2},i-\frac{1}{2}}^n}{4} \right) - \frac{1}{Re} \left(\frac{u_{j,i+\frac{1}{2}}^n - u_{j,i-\frac{1}{2}}^n}{x_{j,i+\frac{1}{2}} - x_{j,i-\frac{1}{2}}} \right) \\
 F_{j+\frac{1}{2},i+\frac{1}{2}}^x &= \left(\frac{u_{j+1,i+\frac{1}{2}}^n (y_{j+\frac{1}{2},i+\frac{1}{2}} - y_{j,i+\frac{1}{2}}) + u_{j,i+\frac{1}{2}}^n (y_{j+1,i+\frac{1}{2}} - y_{j+\frac{1}{2},i+\frac{1}{2}})}{y_{j+1,i+\frac{1}{2}} - y_{j,i+\frac{1}{2}}} \right) \cdot \dots \\
 &\quad \dots \cdot \left(\frac{v_{j+\frac{1}{2},i+1}^n (x_{j+\frac{1}{2},i+\frac{1}{2}} - x_{j+\frac{1}{2},i}) + v_{j+\frac{1}{2},i}^n (x_{j+\frac{1}{2},i+1} - x_{j+\frac{1}{2},i+\frac{1}{2}})}{x_{j+\frac{1}{2},i+1} - x_{j+\frac{1}{2},i}} \right) - \frac{1}{Re} \left(\frac{u_{j+1,i+\frac{1}{2}}^n - u_{j,i+\frac{1}{2}}^n}{y_{j+1,i+\frac{1}{2}} - y_{j,i+\frac{1}{2}}} \right) + a_{xy,j+\frac{1}{2},i+\frac{1}{2}}^n \\
 F_{j-\frac{1}{2},i+\frac{1}{2}}^x &= \left(\frac{u_{j,i+\frac{1}{2}}^n (y_{j-\frac{1}{2},i+\frac{1}{2}} - y_{j-1,i+\frac{1}{2}}) + u_{j-1,i+\frac{1}{2}}^n (y_{j,i+\frac{1}{2}} - y_{j-\frac{1}{2},i+\frac{1}{2}})}{y_{j,i+\frac{1}{2}} - y_{j-1,i+\frac{1}{2}}} \right) \cdot \dots \\
 &\quad \dots \cdot \left(\frac{v_{j-\frac{1}{2},i+1}^n (x_{j-\frac{1}{2},i+\frac{1}{2}} - x_{j-\frac{1}{2},i}) + v_{j-\frac{1}{2},i}^n (x_{j-\frac{1}{2},i+1} - x_{j-\frac{1}{2},i+\frac{1}{2}})}{x_{j-\frac{1}{2},i+1} - x_{j-\frac{1}{2},i}} \right) - \frac{1}{Re} \left(\frac{u_{j,i+\frac{1}{2}}^n - u_{j-1,i+\frac{1}{2}}^n}{y_{j,i+\frac{1}{2}} - y_{j-1,i+\frac{1}{2}}} \right) + a_{xy,j-\frac{1}{2},i+\frac{1}{2}}^n
 \end{aligned}$$

2.1.5 Y momentum equation

The nondimensional Navier-Stokes momentum equation in y direction, already derived in (2.14), is :

$$\frac{\partial v}{\partial t} + \frac{\partial(uv)}{\partial x} + \frac{\partial(v^2)}{\partial y} + \frac{\partial p}{\partial y} + \frac{2}{3} \frac{\partial k}{\partial y} = \frac{1}{Re} \left(\frac{\partial^2 v}{\partial x^2} + \frac{\partial^2 v}{\partial y^2} \right) - \left(\frac{\partial a_{xy}}{\partial x} + \frac{\partial a_{yy}}{\partial y} \right) \quad (2.23)$$

where, in order to ease the writing, the superscript * has been omitted.

Integrating (2.23) over the v -control volume shown in Fig.(11) one has [20]:

$$\iint \frac{\partial v}{\partial t} dx dy + \iint \frac{\partial}{\partial x} \left(uv + a_{xy} - \frac{1}{Re} \frac{\partial v}{\partial x} \right) dx dy + \iint \frac{\partial}{\partial y} \left(v^2 + a_{yy} - \frac{1}{Re} \frac{\partial v}{\partial y} \right) dx dy + \iint \frac{\partial p_{eff}}{\partial y} dx dy = 0 \quad (2.24)$$

where we have substituted $p_{eff} = p + 2k/3$.

Application of the Green theorem to the above expression and use of MAC method for the time

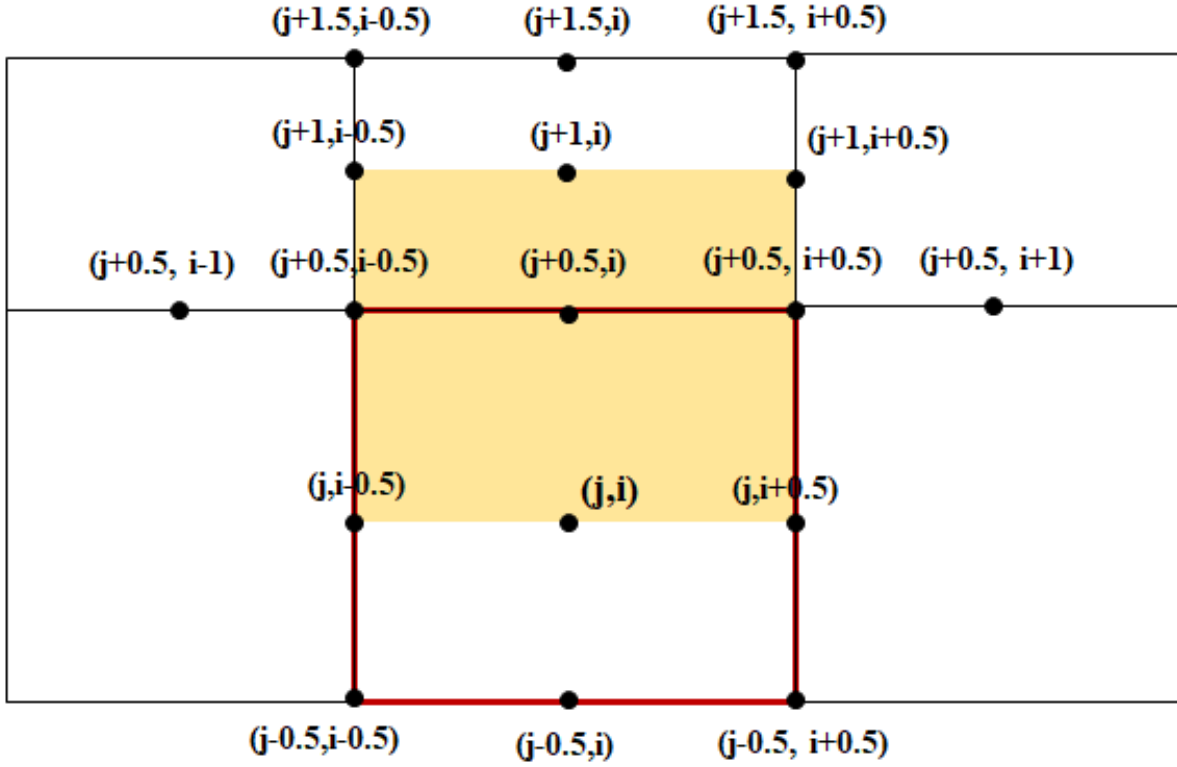


Figure 11: Control volume for the y-momentum equation

discretization leads to:

$$\frac{\Delta x \Delta y}{\Delta t} (v_{j+\frac{1}{2},i}^{n+1} - v_{j+\frac{1}{2},i}^n) + (E_{j,i+1}^y - E_{j,i}^y) \Delta y + \left(F_{j+\frac{1}{2},i+\frac{1}{2}}^y - F_{j-\frac{1}{2},i+\frac{1}{2}}^y \right) \Delta x + (p_{eff,j+1,i}^{n+1} - p_{eff,j,i}^{n+1}) \Delta x = 0 \quad (2.25)$$

or equivalently :

$$\frac{(v_{j+\frac{1}{2},i}^{n+1} - v_{j+\frac{1}{2},i}^n)}{\Delta t} + \frac{(E_{j,i+1}^x - E_{j,i}^x)}{\Delta x} + \frac{(F_{j+\frac{1}{2},i+\frac{1}{2}}^x - F_{j-\frac{1}{2},i+\frac{1}{2}}^x)}{\Delta y} + \frac{(p_{eff,j+1,i}^{n+1} - p_{eff,j,i}^{n+1})}{\Delta y} = 0 \quad (2.26)$$

where $\Delta x = x_{j+\frac{1}{2},i+\frac{1}{2}} - x_{j+\frac{1}{2},i-\frac{1}{2}}$ and $\Delta y = y_{j+1,i} - y_{j,i}$ are the x and y dimension of the (j,i) y-momentum Control Volume, $\Delta t = t^{n+1} - t^n$, E^y and F^y are the axial and transversal fluxes of y-momentum defined as:

$$E^y = uv + a_{xy} - \frac{1}{Re} \frac{\partial v}{\partial x} \quad F^y = v^2 + a_{yy} - \frac{1}{Re} \frac{\partial v}{\partial y} \quad (2.27)$$

whose discretized forms for (2.25) can be obtained using linear interpolations (2.17) and the expression for the first derivative (2.16):

$$\begin{aligned}
 F_{j+1,i}^y &= \left(\frac{v_{j+\frac{3}{2},i}^n + v_{j+\frac{1}{2},i}^n}{2} \right)^2 + \left(\frac{a_{yy,j+\frac{1}{2},i+\frac{1}{2}}^n + a_{yy,j+\frac{1}{2},i-\frac{1}{2}}^n + a_{yy,j+\frac{3}{2},i+\frac{1}{2}}^n + a_{yy,j+\frac{3}{2},i-\frac{1}{2}}^n}{4} \right) - \frac{1}{Re} \left(\frac{v_{j+\frac{3}{2},i}^n - v_{j+\frac{1}{2},i}^n}{y_{j+\frac{3}{2},i} - y_{j+\frac{1}{2},i}} \right) \\
 F_{j,i}^y &= \left(\frac{v_{j+\frac{1}{2},i}^n + v_{j-\frac{1}{2},i}^n}{2} \right)^2 + \left(\frac{a_{yy,j-\frac{1}{2},i+\frac{1}{2}}^n + a_{yy,j-\frac{1}{2},i-\frac{1}{2}}^n + a_{yy,j+\frac{1}{2},i+\frac{1}{2}}^n + a_{yy,j+\frac{1}{2},i-\frac{1}{2}}^n}{4} \right) - \frac{1}{Re} \left(\frac{v_{j+\frac{1}{2},i}^n - v_{j-\frac{1}{2},i}^n}{y_{j+\frac{1}{2},i} - y_{j-\frac{1}{2},i}} \right) \\
 E_{j+\frac{1}{2},i+\frac{1}{2}}^y &= \left(\frac{u_{j+1,i+\frac{1}{2}}^n (y_{j+\frac{1}{2},i+\frac{1}{2}} - y_{j,i+\frac{1}{2}}) + u_{j,i+\frac{1}{2}}^n (y_{j+1,i+\frac{1}{2}} - y_{j+\frac{1}{2},i+\frac{1}{2}})}{y_{j+1,i+\frac{1}{2}} - y_{j,i+\frac{1}{2}}} \right) \cdot \dots \\
 &\dots \left(\frac{v_{j+\frac{1}{2},i+1}^n (x_{j+\frac{1}{2},i+\frac{1}{2}} - x_{j+\frac{1}{2},i}) + v_{j+\frac{1}{2},i}^n (x_{j+\frac{1}{2},i+1} - x_{j+\frac{1}{2},i+\frac{1}{2}})}{x_{j+\frac{1}{2},i+1} - x_{j+\frac{1}{2},i}} \right) - \frac{1}{Re} \left(\frac{v_{j+\frac{1}{2},i+1}^n - v_{j+\frac{1}{2},i}^n}{x_{j+\frac{1}{2},i+1} - x_{j+\frac{1}{2},i}} \right) + a_{xy,j+\frac{1}{2},i+\frac{1}{2}}^n \\
 E_{j+\frac{1}{2},i-\frac{1}{2}}^y &= \left(\frac{u_{j+1,i-\frac{1}{2}}^n (y_{j+\frac{1}{2},i-\frac{1}{2}} - y_{j,i-\frac{1}{2}}) + u_{j,i-\frac{1}{2}}^n (y_{j+1,i-\frac{1}{2}} - y_{j+\frac{1}{2},i-\frac{1}{2}})}{y_{j+1,i-\frac{1}{2}} - y_{j,i-\frac{1}{2}}} \right) \cdot \dots \\
 &\dots \left(\frac{v_{j+\frac{1}{2},i}^n (x_{j+\frac{1}{2},i-\frac{1}{2}} - x_{j+\frac{1}{2},i-1}) + v_{j+\frac{1}{2},i-1}^n (x_{j+\frac{1}{2},i} - x_{j+\frac{1}{2},i-\frac{1}{2}})}{x_{j+\frac{1}{2},i} - x_{j+\frac{1}{2},i-1}} \right) - \frac{1}{Re} \left(\frac{v_{j+\frac{1}{2},i}^n - v_{j+\frac{1}{2},i-1}^n}{x_{j+\frac{1}{2},i} - x_{j+\frac{1}{2},i-1}} \right) + a_{xy,j+\frac{1}{2},i-\frac{1}{2}}^n
 \end{aligned}$$

2.1.6 k transport equation

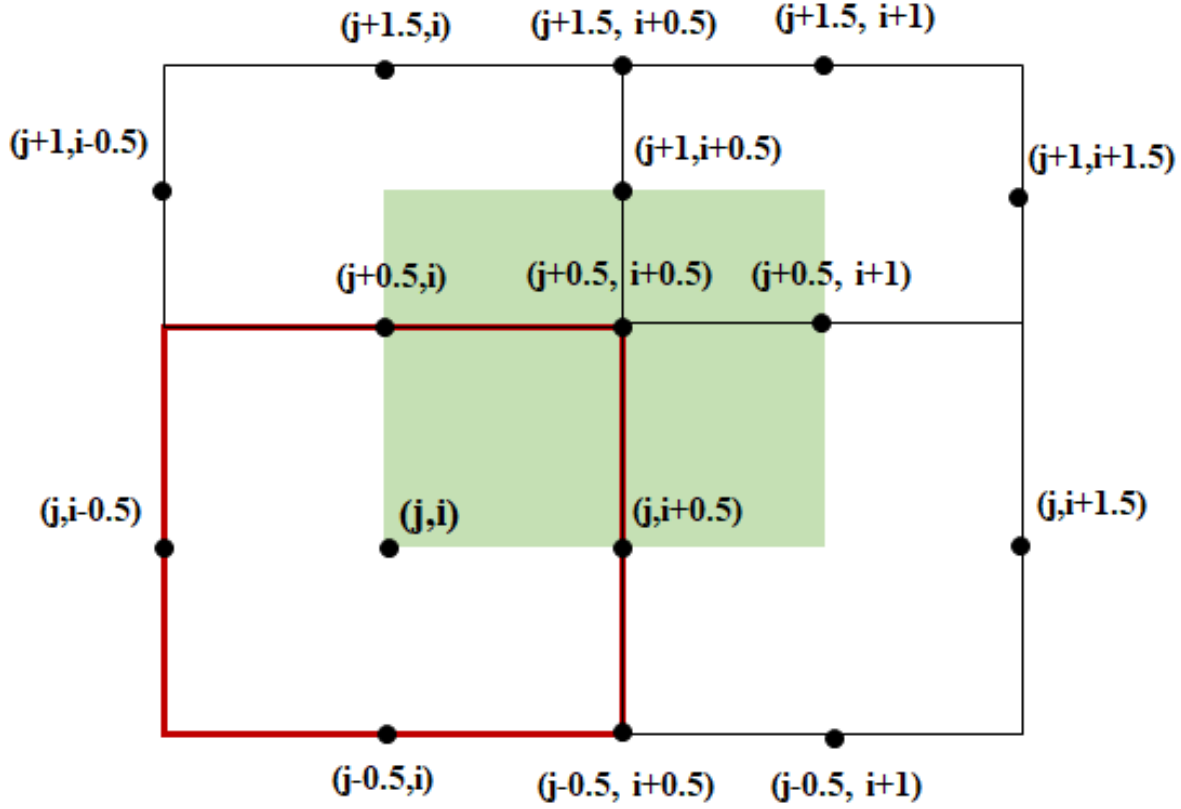
The nondimensional k transport equation, already derived in (2.14), is :

$$\frac{\partial k}{\partial t} + \frac{\partial(uk)}{\partial x} + \frac{\partial(vk)}{\partial y} = \frac{1}{Re} \frac{\partial}{\partial x} \left[\left(1 + \frac{\nu_T}{\sigma_k} \right) \frac{\partial k}{\partial x} \right] + \frac{1}{Re} \frac{\partial}{\partial y} \left[\left(1 + \frac{\nu_T}{\sigma_k} \right) \frac{\partial k}{\partial y} \right] + P - \varepsilon \quad (2.28)$$

where, in order to ease the writing, the superscript * has been omitted.

Integrating (2.23) over the k -control volume shown in Fig.(12):

$$\iint \frac{\partial k}{\partial t} dx dy + \iint \frac{\partial}{\partial x} \left[uk - \left(1 + \frac{\nu_T}{\sigma_k} \right) \frac{\partial k}{\partial x} \right] dx dy + \iint \frac{\partial}{\partial y} \left[vk - \left(1 + \frac{\nu_T}{\sigma_k} \right) \frac{\partial k}{\partial y} \right] dx dy + \iint (P - \varepsilon) dx dy = 0 \quad (2.29)$$



one has:

Figure 12: Control volume for the k-transport equation

Application of the Green theorem to the above expression and use of MAC method for the time discretization leads to:

$$\frac{\Delta x \Delta y}{\Delta t} (k_{j+\frac{1}{2},i+\frac{1}{2}}^{n+1} - k_{j+\frac{1}{2},i+\frac{1}{2}}^n) + (E_{j+\frac{1}{2},i+1}^k - E_{j+\frac{1}{2},i}^k) \Delta y + (F_{j+1,i+\frac{1}{2}}^k - F_{j,i+\frac{1}{2}}^k) \Delta x + \Delta x \Delta y (P_{j+\frac{1}{2},i+\frac{1}{2}}^n - \varepsilon_{j+\frac{1}{2},i+\frac{1}{2}}^n) = 0 \quad (2.30)$$

or equivalently :

$$\frac{(k_{j+\frac{1}{2},i+\frac{1}{2}}^{n+1} - k_{j+\frac{1}{2},i+\frac{1}{2}}^n)}{\Delta t} + \frac{(E_{j+\frac{1}{2},i+1}^k - E_{j+\frac{1}{2},i}^k)}{\Delta x} + \frac{(F_{j+1,i+\frac{1}{2}}^k - F_{j,i+\frac{1}{2}}^k)}{\Delta y} + P_{j+\frac{1}{2},i+\frac{1}{2}}^n - \varepsilon_{j+\frac{1}{2},i+\frac{1}{2}}^n = 0 \quad (2.31)$$

where $\Delta x = x_{j+\frac{1}{2},i+1} - x_{j+\frac{1}{2},i}$ and $\Delta y = y_{j+\frac{1}{2},i+\frac{1}{2}} - y_{j-\frac{1}{2},i+\frac{1}{2}}$ are the x and y dimension of the (j,i) k-transport Control Volume, $\Delta t = t^{n+1} - t^n$, E^k and F^k are the axial and transversal fluxes of k defined as:

$$E^k = uk - \left(1 + \frac{\nu_T}{\sigma_k}\right) \frac{\partial k}{\partial x} \quad F^k = vk - \left(1 + \frac{\nu_T}{\sigma_k}\right) \frac{\partial k}{\partial y} \quad (2.32)$$

whose discretized forms for (2.30) can be obtained using linear interpolations (2.17) and the expression for the first derivative (2.16):

$$\begin{aligned}
E_{j+\frac{1}{2},i+1}^k &= \left[\left(\frac{u_{j,i+\frac{1}{2}}^n + u_{j,i+\frac{3}{2}}^n}{2} \right) \left(\frac{y_{j+1,i+1} - y_{j+\frac{1}{2},i+1}}{y_{j+1,i+1} - y_{j,i+1}} \right) + \left(\frac{u_{j+1,i+\frac{1}{2}}^n + u_{j+1,i+\frac{3}{2}}^n}{2} \right) \left(\frac{y_{j+\frac{1}{2},i+1} - y_{j,i+1}}{y_{j+1,i+1} - y_{j,i+1}} \right) \right] \left[\frac{k_{j+\frac{1}{2},i+\frac{3}{2}}^n + k_{j+\frac{1}{2},i+\frac{1}{2}}^n}{2} \right] \dots \\
&\dots - \left(1 + \frac{\nu_{T,j+\frac{1}{2},i+\frac{3}{2}}^n + \nu_{T,j+\frac{1}{2},i+\frac{1}{2}}^n}{2\sigma_k} \right) \left(\frac{k_{j+\frac{1}{2},i+\frac{3}{2}}^n - k_{j+\frac{1}{2},i+\frac{1}{2}}^n}{x_{j+\frac{1}{2},i+\frac{3}{2}} - x_{j+\frac{1}{2},i+\frac{1}{2}}} \right) \\
E_{j+\frac{1}{2},i}^k &= \left[\left(\frac{u_{j,i-\frac{1}{2}}^n + u_{j,i+\frac{1}{2}}^n}{2} \right) \left(\frac{y_{j+1,i} - y_{j+\frac{1}{2},i}}{y_{j+1,i} - y_{j,i}} \right) + \left(\frac{u_{j+1,i-\frac{1}{2}}^n + u_{j+1,i+\frac{1}{2}}^n}{2} \right) \left(\frac{y_{j+\frac{1}{2},i} - y_{j,i}}{y_{j+1,i} - y_{j,i}} \right) \right] \left[\frac{k_{j+\frac{1}{2},i+\frac{1}{2}}^n + k_{j+\frac{1}{2},i-\frac{1}{2}}^n}{2} \right] \dots \\
&\dots - \left(1 + \frac{\nu_{T,j+\frac{1}{2},i+\frac{1}{2}}^n + \nu_{T,j+\frac{1}{2},i-\frac{1}{2}}^n}{2\sigma_k} \right) \left(\frac{k_{j+\frac{1}{2},i+\frac{1}{2}}^n - k_{j+\frac{1}{2},i-\frac{1}{2}}^n}{x_{j+\frac{1}{2},i+\frac{1}{2}} - x_{j+\frac{1}{2},i-\frac{1}{2}}} \right) \\
F_{j+1,i+\frac{1}{2}}^k &= \left[\left(\frac{\nu_{j+\frac{3}{2},i+1}^n + \nu_{j+\frac{1}{2},i+1}^n}{2} \right) \left(\frac{x_{j+1,i+\frac{1}{2}} - x_{j+1,i}}{x_{j+1,i+1} - x_{j+1,i}} \right) + \left(\frac{\nu_{j+\frac{3}{2},i}^n + \nu_{j+\frac{1}{2},i}^n}{2} \right) \left(\frac{x_{j+1,i+1} - x_{j+1,i+\frac{1}{2}}}{x_{j+1,i+1} - x_{j+1,i}} \right) \right] \left[\frac{k_{j+\frac{3}{2},i+\frac{1}{2}}^n + k_{j+\frac{1}{2},i+\frac{1}{2}}^n}{2} \right] \dots \\
&\dots - \left(1 + \frac{\nu_{T,j+\frac{3}{2},i+\frac{1}{2}}^n + \nu_{T,j+\frac{1}{2},i+\frac{1}{2}}^n}{2\sigma_k} \right) \left(\frac{k_{j+\frac{3}{2},i+\frac{1}{2}}^n - k_{j+\frac{1}{2},i+\frac{1}{2}}^n}{y_{j+\frac{3}{2},i+\frac{1}{2}} - y_{j+\frac{1}{2},i+\frac{1}{2}}} \right) \\
F_{j,i+\frac{1}{2}}^k &= \left[\left(\frac{\nu_{j+\frac{1}{2},i+1}^n + \nu_{j-\frac{1}{2},i+1}^n}{2} \right) \left(\frac{x_{j,i+\frac{1}{2}} - x_{j,i}}{x_{j,i+1} - x_{j,i}} \right) + \left(\frac{\nu_{j+\frac{1}{2},i}^n + \nu_{j-\frac{1}{2},i}^n}{2} \right) \left(\frac{x_{j,i+1} - x_{j,i+\frac{1}{2}}}{x_{j,i+1} - x_{j,i}} \right) \right] \left[\frac{k_{j+\frac{1}{2},i+\frac{1}{2}}^n + k_{j-\frac{1}{2},i+\frac{1}{2}}^n}{2} \right] \dots \\
&\dots - \left(1 + \frac{\nu_{T,j+\frac{1}{2},i+\frac{1}{2}}^n + \nu_{T,j-\frac{1}{2},i+\frac{1}{2}}^n}{2\sigma_k} \right) \left(\frac{k_{j+\frac{1}{2},i+\frac{1}{2}}^n - k_{j-\frac{1}{2},i+\frac{1}{2}}^n}{y_{j+\frac{1}{2},i+\frac{1}{2}} - y_{j-\frac{1}{2},i+\frac{1}{2}}} \right)
\end{aligned}$$

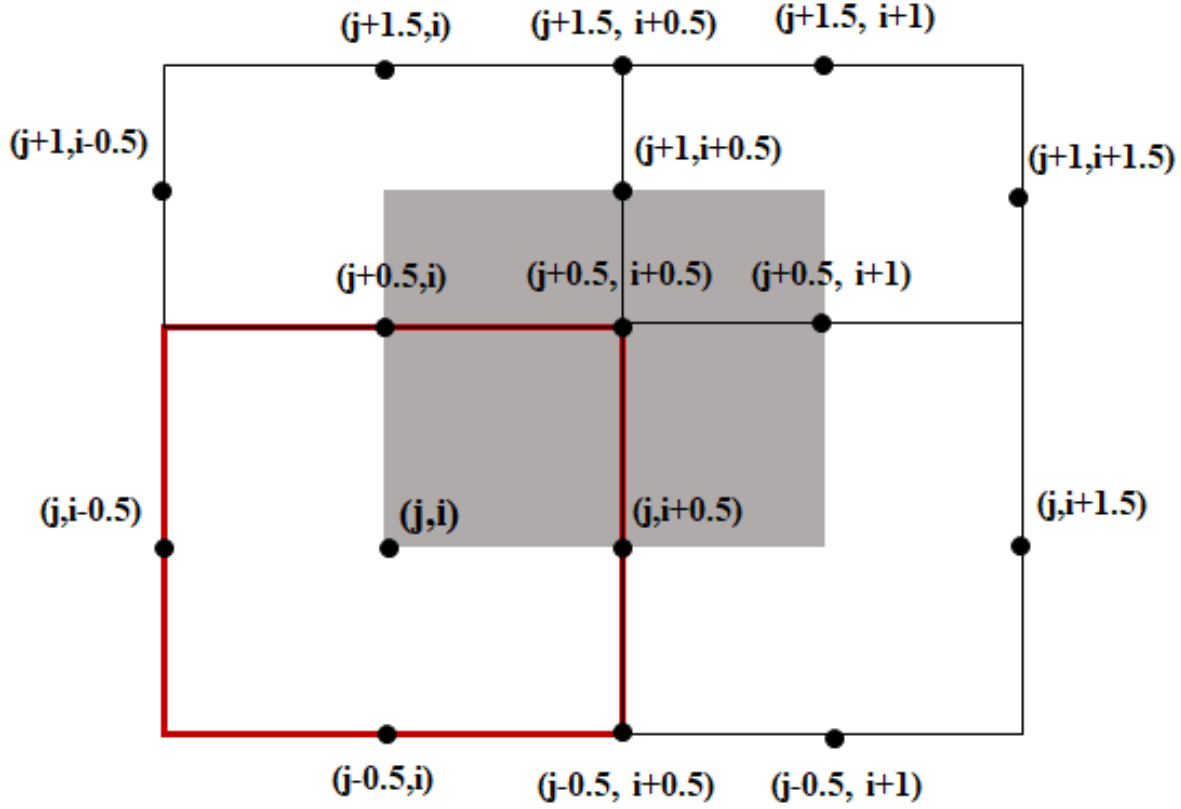
2.1.7 ε transport equation

The nondimensional ε transport equation, already derived in (2.14), is :

$$\frac{\partial \varepsilon}{\partial t} + \frac{\partial(u\varepsilon)}{\partial x} + \frac{\partial(v\varepsilon)}{\partial y} = \frac{1}{Re} \frac{\partial}{\partial x} \left[\left(1 + \frac{\nu_T}{\sigma_\varepsilon} \right) \frac{\partial \varepsilon}{\partial x} \right] + \frac{1}{Re} \frac{\partial}{\partial y} \left[\left(1 + \frac{\nu_T}{\sigma_\varepsilon} \right) \frac{\partial \varepsilon}{\partial y} \right] + C_{\varepsilon 1} \frac{P\varepsilon}{k} - C_{\varepsilon 2} \frac{\varepsilon^2}{k} \quad (2.33)$$

where, in order to ease the writing, the superscript * has been omitted.

Integrating (2.23) over the ε -control volume shown in Fig.(13):

Figure 13: Control volume for the ε -transport equation

one has:

$$\iint \frac{\partial \varepsilon}{\partial t} dxdy + \iint \frac{\partial}{\partial x} \left[u\varepsilon - \left(1 + \frac{\nu_T}{\sigma_\varepsilon} \right) \frac{\partial \varepsilon}{\partial x} \right] dxdy + \iint \frac{\partial}{\partial y} \left[v\varepsilon - \left(1 + \frac{\nu_T}{\sigma_\varepsilon} \right) \frac{\partial \varepsilon}{\partial y} \right] dxdy + \iint \frac{\varepsilon}{k} (C_{\varepsilon 1} P - C_{\varepsilon 2} \varepsilon) dxdy = 0 \quad (2.34)$$

Application of the Green theorem to the above expression and use of MAC method for the time discretization leads to:

$$\frac{\Delta x \Delta y}{\Delta t} (\varepsilon_{j+\frac{1}{2},i+\frac{1}{2}}^{n+1} - \varepsilon_{j+\frac{1}{2},i+\frac{1}{2}}^n) + \left(E_{j+\frac{1}{2},i+1}^\varepsilon - E_{j+\frac{1}{2},i}^\varepsilon \right) \Delta y + \left(F_{j+1,i+\frac{1}{2}}^\varepsilon - F_{j,i+\frac{1}{2}}^\varepsilon \right) \Delta x + \Delta x \Delta y \frac{\varepsilon_{j+\frac{1}{2},i+\frac{1}{2}}^n}{k_{j+\frac{1}{2},i+\frac{1}{2}}^n} (C_{\varepsilon 1} P_{j+\frac{1}{2},i+\frac{1}{2}}^n - C_{\varepsilon 2} \varepsilon_{j+\frac{1}{2},i+\frac{1}{2}}^n) = 0 \quad (2.35)$$

or equivalently :

$$\frac{(\varepsilon_{j+\frac{1}{2},i+\frac{1}{2}}^{n+1} - \varepsilon_{j+\frac{1}{2},i+\frac{1}{2}}^n)}{\Delta t} + \frac{(E_{j+\frac{1}{2},i+1}^\varepsilon - E_{j+\frac{1}{2},i}^\varepsilon)}{\Delta x} + \frac{(F_{j+1,i+\frac{1}{2}}^\varepsilon - F_{j,i+\frac{1}{2}}^\varepsilon)}{\Delta y} + \frac{\varepsilon_{j+\frac{1}{2},i+\frac{1}{2}}^n}{k_{j+\frac{1}{2},i+\frac{1}{2}}^n} (C_{\varepsilon 1} P_{j+\frac{1}{2},i+\frac{1}{2}}^n - C_{\varepsilon 2} \varepsilon_{j+\frac{1}{2},i+\frac{1}{2}}^n) = 0 \quad (2.36)$$

where $\Delta x = x_{j+\frac{1}{2},i+1} - x_{j+\frac{1}{2},i}$ and $\Delta y = y_{j+\frac{1}{2},i+\frac{1}{2}} - y_{j-\frac{1}{2},i+\frac{1}{2}}$ are the x and y dimension of the (j,i) ε transport Control Volume, $\Delta t = t^{n+1} - t^n$, E^ε and F^ε are the axial and transversal fluxes of ε defined

as:

$$E^\varepsilon = u\varepsilon - \left(1 + \frac{\nu_T}{\sigma_\varepsilon}\right) \frac{\partial \varepsilon}{\partial x} \quad F^\varepsilon = v\varepsilon - \left(1 + \frac{\nu_T}{\sigma_\varepsilon}\right) \frac{\partial \varepsilon}{\partial y} \quad (2.37)$$

whose discretized forms for (2.35) can be obtained using linear interpolations (2.17) and the expression for the first derivative (2.16):

$$\begin{aligned} E_{j+\frac{1}{2},i+1}^\varepsilon &= \left[\left(\frac{u_{j,i+\frac{1}{2}}^n + u_{j,i+\frac{3}{2}}^n}{2} \right) \left(\frac{y_{j+1,i+1} - y_{j+\frac{1}{2},i+1}}{y_{j+1,i+1} - y_{j,i+1}} \right) + \left(\frac{u_{j+1,i+\frac{1}{2}}^n + u_{j+1,i+\frac{3}{2}}^n}{2} \right) \left(\frac{y_{j+\frac{1}{2},i+1} - y_{j,i+1}}{y_{j+1,i+1} - y_{j,i+1}} \right) \right] \left[\frac{\varepsilon_{j+\frac{1}{2},i+\frac{3}{2}}^n + \varepsilon_{j+\frac{1}{2},i+\frac{1}{2}}^n}{2} \right] \dots \\ &\quad \dots - \left(1 + \frac{\nu_{T,j+\frac{1}{2},i+\frac{3}{2}}^n + \nu_{T,j+\frac{1}{2},i+\frac{1}{2}}^n}{2\sigma_\varepsilon} \right) \left(\frac{\varepsilon_{j+\frac{1}{2},i+\frac{3}{2}}^n - \varepsilon_{j+\frac{1}{2},i+\frac{1}{2}}^n}{x_{j+\frac{1}{2},i+\frac{3}{2}} - x_{j+\frac{1}{2},i+\frac{1}{2}}} \right) \\ E_{j+\frac{1}{2},i}^\varepsilon &= \left[\left(\frac{u_{j,i-\frac{1}{2}}^n + u_{j,i+\frac{1}{2}}^n}{2} \right) \left(\frac{y_{j+1,i} - y_{j+\frac{1}{2},i}}{y_{j+1,i} - y_{j,i}} \right) + \left(\frac{u_{j+1,i-\frac{1}{2}}^n + u_{j+1,i+\frac{1}{2}}^n}{2} \right) \left(\frac{y_{j+\frac{1}{2},i} - y_{j,i}}{y_{j+1,i} - y_{j,i}} \right) \right] \left[\frac{\varepsilon_{j+\frac{1}{2},i+\frac{1}{2}}^n + \varepsilon_{j+\frac{1}{2},i-\frac{1}{2}}^n}{2} \right] \dots \\ &\quad \dots - \left(1 + \frac{\nu_{T,j+\frac{1}{2},i+\frac{1}{2}}^n + \nu_{T,j+\frac{1}{2},i-\frac{1}{2}}^n}{2\sigma_\varepsilon} \right) \left(\frac{\varepsilon_{j+\frac{1}{2},i+\frac{1}{2}}^n - \varepsilon_{j+\frac{1}{2},i-\frac{1}{2}}^n}{x_{j+\frac{1}{2},i+\frac{1}{2}} - x_{j+\frac{1}{2},i-\frac{1}{2}}} \right) \\ F_{j+1,i+\frac{1}{2}}^\varepsilon &= \left[\left(\frac{v_{j+\frac{3}{2},i+1}^n + v_{j+\frac{1}{2},i+1}^n}{2} \right) \left(\frac{x_{j+1,i+\frac{1}{2}} - x_{j+1,i}}{x_{j+1,i+1} - x_{j+1,i}} \right) + \left(\frac{v_{j+\frac{3}{2},i}^n + v_{j+\frac{1}{2},i}^n}{2} \right) \left(\frac{x_{j+1,i+1} - x_{j+1,i+\frac{1}{2}}}{x_{j+1,i+1} - x_{j+1,i}} \right) \right] \left[\frac{\varepsilon_{j+\frac{3}{2},i+\frac{1}{2}}^n + \varepsilon_{j+\frac{1}{2},i+\frac{1}{2}}^n}{2} \right] \dots \\ &\quad \dots - \left(1 + \frac{\nu_{T,j+\frac{3}{2},i+\frac{1}{2}}^n + \nu_{T,j+\frac{1}{2},i+\frac{1}{2}}^n}{2\sigma_\varepsilon} \right) \left(\frac{\varepsilon_{j+\frac{3}{2},i+\frac{1}{2}}^n - \varepsilon_{j+\frac{1}{2},i+\frac{1}{2}}^n}{y_{j+\frac{3}{2},i+\frac{1}{2}} - y_{j+\frac{1}{2},i+\frac{1}{2}}} \right) \\ F_{j,i+\frac{1}{2}}^\varepsilon &= \left[\left(\frac{v_{j+\frac{1}{2},i+1}^n + v_{j-\frac{1}{2},i+1}^n}{2} \right) \left(\frac{x_{j,i+\frac{1}{2}} - x_{j,i}}{x_{j,i+1} - x_{j,i}} \right) + \left(\frac{v_{j+\frac{1}{2},i}^n + v_{j-\frac{1}{2},i}^n}{2} \right) \left(\frac{x_{j,i+1} - x_{j,i+\frac{1}{2}}}{x_{j,i+1} - x_{j,i}} \right) \right] \left[\frac{\varepsilon_{j+\frac{1}{2},i+\frac{1}{2}}^n + \varepsilon_{j-\frac{1}{2},i+\frac{1}{2}}^n}{2} \right] \dots \\ &\quad \dots - \left(1 + \frac{\nu_{T,j+\frac{1}{2},i+\frac{1}{2}}^n + \nu_{T,j-\frac{1}{2},i+\frac{1}{2}}^n}{2\sigma_\varepsilon} \right) \left(\frac{\varepsilon_{j+\frac{1}{2},i+\frac{1}{2}}^n - \varepsilon_{j-\frac{1}{2},i+\frac{1}{2}}^n}{y_{j+\frac{1}{2},i+\frac{1}{2}} - y_{j-\frac{1}{2},i+\frac{1}{2}}} \right) \end{aligned}$$

2.1.8 Poisson Equation

It is now important to explain how to deal with the pressure field, since it is involved in the computation of the components of the velocity field (2.26) and (2.21). Indeed the pressure difference represents the natural driving force for velocity field changes. By looking at the nondimensional Navier-Stokes system of equations (2.14), one can observe that the Continuity equation has not still

been explicitly discretized. By applying a Central-Space scheme -as for the momentum equations and the transport equations-, continuity equation can be discretized as:

$$\frac{u_{i+\frac{1}{2},j}^{n+1} - u_{i-\frac{1}{2},j}^{n+1}}{\Delta x} + \frac{v_{i,j+\frac{1}{2}}^{n+1} - v_{i,j-\frac{1}{2}}^{n+1}}{\Delta y} = 0 \quad (2.38)$$

where the Control Volume for continuity equation (2.38) is shown in the following Fig.(14):

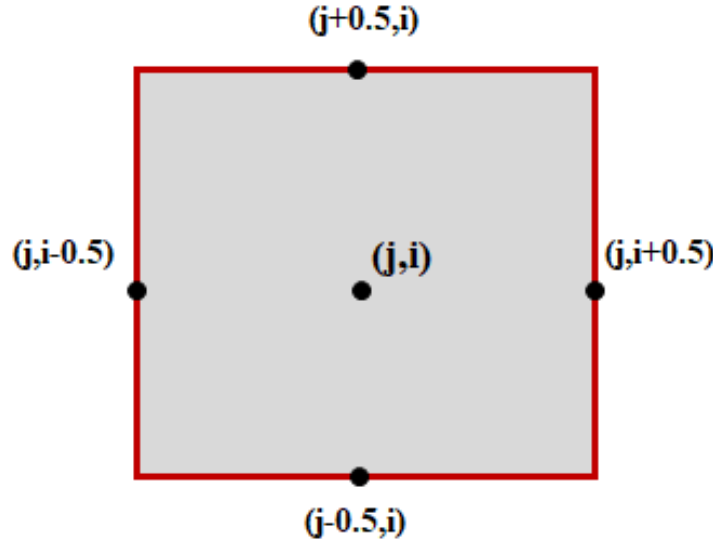


Figure 14: Control volume for the continuity equation

where $\Delta x = x_{j,i+\frac{1}{2}} - x_{j,i-\frac{1}{2}}$ and $\Delta y = y_{j+\frac{1}{2},i} - y_{j-\frac{1}{2},i}$ are the x and y dimension of the (j,i) continuity equation Control Volume. In order to further manipulate (2.38) we can observe that (2.21) and (2.26) can be rewritten as:

$$u_{j,i+\frac{1}{2}}^{n+1} = u_{j,i+\frac{1}{2}}^n - \Delta t \left[\frac{(E_{j,i+1}^x - E_{j,i}^x)}{\Delta x^u} + \frac{(F_{j+\frac{1}{2},i+\frac{1}{2}}^x - F_{j-\frac{1}{2},i+\frac{1}{2}}^x)}{\Delta y^u} \right] - \frac{\Delta t}{\Delta x^u} (p_{eff,j,i+1}^{n+1} - p_{eff,j,i}^{n+1})$$

$$v_{j+\frac{1}{2},i}^{n+1} = v_{j+\frac{1}{2},i}^n - \Delta t \left[\frac{(E_{j,i+1}^x - E_{j,i}^x)}{\Delta x^v} + \frac{(F_{j+\frac{1}{2},i+\frac{1}{2}}^x - F_{j-\frac{1}{2},i+\frac{1}{2}}^x)}{\Delta y^v} \right] - \frac{\Delta t}{\Delta y^v} (p_{eff,j+1,i}^{n+1} - p_{eff,j,i}^{n+1})$$

or equivalently:

$$u_{j,i+\frac{1}{2}}^{n+1} = X_{j,i+\frac{1}{2}}^n - \frac{\Delta t}{\Delta x^u} (p_{eff,j,i+1}^{n+1} - p_{eff,j,i}^{n+1}) \quad (2.39)$$

$$v_{j+\frac{1}{2},i}^{n+1} = Y_{j+\frac{1}{2},i}^n - \frac{\Delta t}{\Delta y^v} (p_{eff,j+1,i}^{n+1} - p_{eff,j,i}^{n+1}) \quad (2.40)$$

where:

$$X_{j,i+\frac{1}{2}}^n = u_{j,i+\frac{1}{2}}^n - \Delta t \left[\frac{(E_{j,i+1}^x - E_{j,i}^x)}{\Delta x^u} + \frac{(F_{j+\frac{1}{2},i+\frac{1}{2}}^x - F_{j-\frac{1}{2},i+\frac{1}{2}}^x)}{\Delta y^u} \right] \quad (2.41)$$

$$Y_{j+\frac{1}{2},i}^n = v_{j+\frac{1}{2},i}^n - \Delta t \left[\frac{(E_{j,i+1}^x - E_{j,i}^x)}{\Delta x^v} + \frac{(F_{j+\frac{1}{2},i+\frac{1}{2}}^x - F_{j-\frac{1}{2},i+\frac{1}{2}}^x)}{\Delta y^v} \right] \quad (2.42)$$

and where $\Delta x^u = x_{j,i+1} - x_{j,i}$ and $\Delta y^u = y_{j+\frac{1}{2},i+\frac{1}{2}} - y_{j-\frac{1}{2},i+\frac{1}{2}}$ are the dimensions of the (j,i) x-momentum Control Volume and $\Delta x^v = x_{j+\frac{1}{2},i+\frac{1}{2}} - x_{j+\frac{1}{2},i-\frac{1}{2}}$ and $\Delta y^v = y_{j+1,i} - y_{j,i}$ are the x and y dimension of the (j,i) y-momentum Control Volume. By substituting (2.39) and (2.40) in (2.38), one has:

$$\left[\frac{p_{eff,j,i-1} - 2p_{eff,j,i} + p_{eff,j,i+1}}{\Delta x \Delta x^u} + \frac{p_{eff,j-1,i} - 2p_{eff,j,i} + p_{eff,j+1,i}}{\Delta y \Delta y^v} \right]^{n+1} = \frac{1}{\Delta t} \left[\frac{X_{j,i+\frac{1}{2}}^n - X_{j,i-\frac{1}{2}}^n}{\Delta x} + \frac{Y_{j+\frac{1}{2},i}^n - Y_{j-\frac{1}{2},i}^n}{\Delta y} \right] = Q_{j,i}^n \quad (2.43)$$

which represents the discrete Poisson equation for pressure. It is interesting to notice that, by deriving the numerical formulation of the Poisson equation from the numerical formulation of the Navier Stokes equation, we do not have to worry that the two equations are discretized with the same scheme. It is also important to point out that, obtaining the solution of the discrete Poisson equation for pressure, ensures that the incompressibility property of the velocity field is transmitted from t^n to t^{n+1} through (2.21) and (2.26). This means that if \mathbf{U}^n is divergence free, then also \mathbf{U}^{n+1} computed with (2.21) and (2.26) will have the same property.

In equation (2.43), the values of the pressure field at t^{n+1} depend only on velocity field's values computed at t^n and summarized in the term $Q_{j,i}^n$. Hence the term $Q_{j,i}^n$, which in the Poisson equation corresponds to a source term, is known in each point of the grid when we have to compute $p_{eff,j,i}^{n+1}$. The discrete equation (2.43) corresponds to the discretization of the Poisson equation for pressure:

$$\nabla^2 p_{eff} = \frac{\partial^2 p_{eff}}{\partial x^2} + \frac{\partial^2 p_{eff}}{\partial y^2} = f(x,y) \quad (2.44)$$

where $Q_{j,i}^n \equiv f(x_i, y_j)$.

In order to solve the discrete Poisson equation (2.43), it is possible to transform (2.44) into a transient problem, as shown in the following section.

2.1.9 Poisson Equation Solver

Equation (2.43) is solved using the Gauss-Seidel iterative method. Starting from the unsteady Poisson equation for pressure and substituting $P = p_{eff}$ for ease of writing, one has:

$$\frac{\partial^2 P}{\partial x^2} + \frac{\partial^2 P}{\partial y^2} = f(x, y)$$

one can think of transforming it into a transient problem by looking for the steady state solution of equation

$$\frac{\partial P}{\partial t} = \frac{\partial^2 P}{\partial x^2} + \frac{\partial^2 P}{\partial y^2} - f(x, y) \quad (2.45)$$

since at steady state $\frac{\partial P}{\partial t} = 0$. Hence the steady state solution of (2.45) corresponds to the solution of (2.44). By applying a Finite Difference, Central-in-space and Forward-in-time discretization to (2.45), as shown above, one has:

$$\frac{P_{j,i}^{n+1} - P_{j,i}^n}{\Delta t} = \frac{P_{j,i-1}^n - 2P_{j,i}^n + P_{j,i+1}^n}{\Delta x \Delta x^u} + \frac{P_{j-1,i}^n - 2P_{j,i}^n + P_{j+1,i}^n}{\Delta y \Delta y^v} - Q_{j,i}^n \quad (2.46)$$

On a uniform grid with $\Delta = \Delta x = \Delta y$ and choosing $\Delta t = \Delta/4$ which corresponds to the maximum allowed Δt due to stability reasons, it follows:

$$P_{i,j}^{n+1} = \frac{1}{4} (P_{i-1,j}^n + P_{i,j-1}^n + P_{i+1,j}^n + P_{i,j+1}^n - \Delta^2 Q_{i,j}^n) \quad (2.47)$$

which is the Richardson Method. In the case of non-uniform grid -as the one here - the derivation is similar and straightforward, hence it will not be presented here.

The Gauss-Seidel method follows a similar derivation which leads to:

$$P_{i,j}^{n+1} = \frac{1}{4} (P_{i-1,j}^{n+1} + P_{i,j-1}^{n+1} + P_{i+1,j}^n + P_{i,j+1}^n - \Delta^2 Q_{i,j}^n) \quad (2.48)$$

It is important to notice that (2.48) is still an explicit method. Indeed, despite the quantity $P_{i-1,j}^{n+1} + P_{i,j-1}^{n+1}$ is involved, one can observe that the two values are already computed before calculating $P_{i,j}^{n+1}$.

Applying a successive over-relaxation one obtains:

$$\begin{cases} \widetilde{P}_{i,j}^{n+1} = \frac{1}{4} (P_{i-1,j}^{n+1} + P_{i,j-1}^{n+1} + P_{i+1,j}^n + P_{i,j+1}^n - \Delta^2 Q_{i,j}^n) \\ P_{i,j}^{n+1} = P_{i,j}^n + \omega (\widetilde{P}_{i,j}^{n+1} - P_{i,j}^n) \end{cases} \quad (2.49)$$

where ω is the relaxation factor. Here we chose $\omega = 1.6$ as it is the optimal value that, for this case, allows a fewer number of iterations to get to the steady-state solution. Again, equations in system (2.49) are both explicit.

Hence, in order to solve (2.43), one starts with a tentative pressure fields and applies (2.49) iteratively until the change between the pressure fields of two consecutive iterations is below a certain tolerance. At this point, the pressure field will correspond to the steady state solution of (2.45) and therefore to the solution of (2.44).

Once the pressure field has been calculated, the values of pressure can be used in (2.21) and (2.26) to compute the velocity field at the next time step. Since in general the pressure field does not change a lot between two consecutive times steps, as a good initial value of the pressure field one should use the pressure distribution at the previous time step.

A final remark is that when equations (2.49) are computed in correspondence of the boundary cells, some indices will exceed the physical domain. In this case, the pressure boundary conditions on the four walls must be used. These Boundary Conditions will be directly enforced on the ghost cells' layer as it will be explained in the following sections.

2.2 Turbulent fully-developed channel flow

Here we briefly review a few key concepts of the physics of turbulent channel flow, since it is a flow case to whom the RANS solver will be applied. Turbulent channel flow is a pressure-driven flow between two parallel planes where the fluid proceeds primarily along the x direction. The direction normal to the wall is the y direction [18]. If we assume an infinite width of the plates, so that any edge effect can be neglected, the flow results two-dimensional and can be analyzed in the x - y plane only, as showed in Fig.(15). When a pressure gradient $dp/dx < 0$ is applied, the fluid accelerates in the x direction and the velocity profile $U(y)$ assumes different shapes along the plate lenght. In particular, a velocity boundary layer develops from the channel inlet through the channel length. If the channel is sufficiently long, the velocity boundary layer reaches the channel axis: at that point the flow is said to be fully developed since the velocity profile remains steady and does not change anymore with x . Therefore, a fully-developed, turbulent channel flow shows a one-dimensional structure along the y direction. That is, after performing the averaging procedure, the flow quantities (such as average velocity) are only functions of the distance across the channel, y .

It is natural to normalize the wall-normal distance y and to work in viscous wall units which are denoted by:

$$y^+ = \frac{y}{h_\nu} \quad (2.50)$$

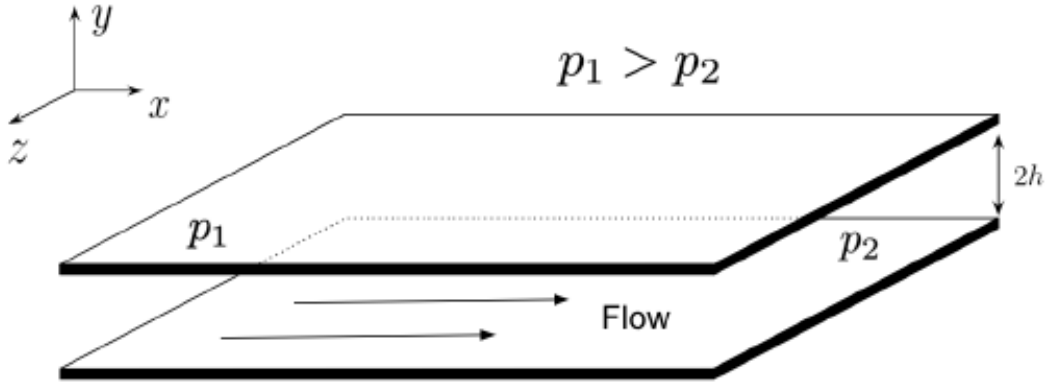


Figure 15: Geometry of the channel flow

where $h_v = \nu/u_\tau$ is the viscous lengthscale and:

$$u_\tau = \sqrt{\frac{\tau_w}{\rho}} \quad (2.51)$$

is called the friction velocity, with τ_w being the shear stress at the wall.

The dimensionless quantity:

$$Re_\tau = \frac{u_\tau h}{\nu} \quad (2.52)$$

where h is half the height of the channel, is called the friction Reynolds number.

Lastly, a key turbulence nondimensionalization used in channel flows is [38] :

$$u^+ = \frac{u}{u_\tau} \quad (2.53)$$

Working with y^+ units is a convenient normalization for wall-bounded flows, as it naturally reveals important regions of the flow field. In channel flows, the near-wall and bulk regions exhibit distinctly different flow features, with dissipation mostly localized within the former. Many simple eddy viscosity models do not make any distinction between these regions and therefore ad-hoc damping factors are used in low-Reynolds models - such as f_μ for the Abe-Kondoh-Nagano one [23].

In this present work, the turbulent channel flow at $Re_\tau = 544$ - corresponding to a $Re_b = 10000$ [6] based on the bulk mean flow u - is used both as a validation case for the RANS solver and as a test-case for the implementation of the proposed data driven approach. Indeed, the channel flow was the first geometries for which a Direct Numerical Simulation has been performed and therefore it represents a classical benchmark for testing CFD turbulent solvers.

In the simulations, the geometry consists only of half of the height of the channel due to symmetry reasons. Moreover, only the fully developed region is simulated, both because most of the validation DNS data are available for this region and in order to minimize the simulation time.

Lastly, it is important to choose the characteristic length and velocities used to nondimensionalize the main variables according to (2.2). Using the same notation of (2.2), for the channel flow it has been chosen:

$$U = u_\tau \quad L = h \quad (2.54)$$

where h is half the height of the channel. It is clear that with this choice $0 < y^* < 1$ where y^* correspond to the nondimensional distance from the wall. Moreover, with this choice one has that $u^* = u/u_\tau = u^+$

2.2.1 Mesh

The mesh used for the RANS solver is shown in the following Fig.(16):

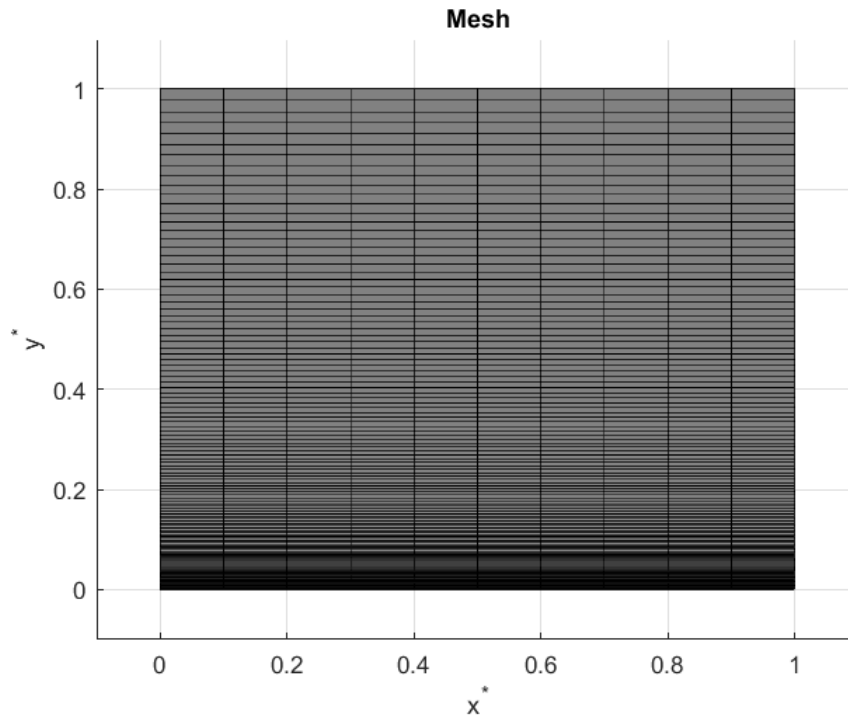


Figure 16: Mesh for the turbulent channel flow

where in Fig.(17) it is shown a magnification of Fig.(16) near the wall ($y^* = 0$) to highlight the near-wall resolution required by a wall resolved method.

The mesh consists of $N_y = 120$ cells along the y direction and $N_x = 10$ points along the x direction. This choice is motivated by the fact that, in the fully developed region, the quantities vary only with y and therefore the x direction is not relevant for the description of the flow. It is also important to mention that the horizontal size of the mesh $0 < x^* < 1$ could have been chosen differently, since the profile of the quantities is the same along x . The size value 1 was chosen in order to obtain an easy

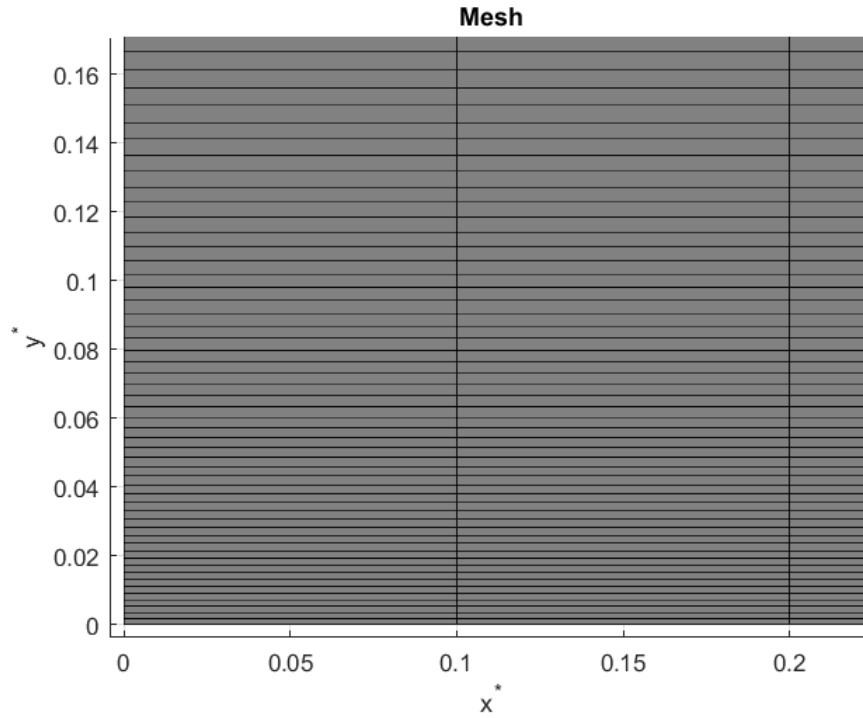


Figure 17: Magnification of the mesh for the turbulent channel flow, near-wall resolution

value of Δp^* to compute, as later shown.

As far as the cell dimension is concerned, the following distribution has been chosen:

- Δx is the same for all the cells, since the gradient of the quantities along the x direction is null.
- For the vertical dimension a growth-rate type of stretching is chosen. This stretching along y satisfies:

$$\frac{\Delta y_{i+1}}{\Delta y_i} = g = \text{const}$$

where Δy_i is the vertical dimension of a generic cell, Δy_{i+1} is the vertical dimension of the cell above and $g=1.02$ is a constant. This stretching of the cell's vertical dimension is justified by the attempt to reduce the numerical discretization error. Indeed, when a numerical approximation is introduced, like the one of the first derivative (2.16), the difference between the real value of the discretized quantity and the value of its numerical approximation is proportional to the gradient of the quantity and to the cell size. Hence, the general idea driving a mesh realization is to refine it in regions where the gradients of the quantities is steeper - in order to catch these steep variations - and to make it coarser where the quantities are almost constant. Since in a turbulent channel flow the gradient of all quantities is very steep near the wall and null at the channel's centerline, it is a general practice to refine the mesh size near the wall and to have a coarser mesh near the centerline, as the growth-rate relation above ensures.

Since a low-Reynolds model is employed, one has to ensure that the first cell falls well into the viscous sublayer. The usual value is $y^+ \simeq 1$.

From the definition of $h_\nu = \nu/u_\tau$, one has:

$$h_\nu^* = \frac{h_\nu}{h} = \frac{\nu}{u_\tau h} = \frac{1}{Re_\tau} \quad (2.55)$$

from which:

$$y^{+*} = \frac{y^*}{h_\nu^*} = y^* Re_\tau \quad (2.56)$$

Hence $y^+ \simeq 1$ will correspond, in nondimensional units, to:

$$y^* = \frac{1}{Re_\tau} = 0.00184$$

By using $g=1.02$ and $N_y = 120$, the first cell's height corresponds to $y^* = 0.00175 \simeq 0.00184$ and therefore the condition on the mesh wall resolution is satisfied.

2.2.2 Boundary Conditions

A scheme of the boundary conditions is presented in the following Fig.(18).

At $y^* = 0$ a wall boundary condition is enforced to reproduce the presence of the physical wall. At $y^* = 1$ a symmetry boundary condition is enforced since this boundary corresponds to the channel axis and the problem is symmetric with respect to it. At $x^* = 1$ and $x^* = 0$ a Zero Gradient boundary condition is enforced because the flow is simulated in the fully-developed region, where the variation of velocity and turbulent quantities along x is null. Yet, it is important to stress that the Zero Gradient condition does not apply to pressure. Indeed, pressure represents the 'driving force' of the fluid, and to keep to fluid in motion along the channel a negative pressure gradient dp/dx is necessary - Fig.(15). By manipulating the axial mean-momentum equation (2.18) under the assumptions of boundary-layer flow, and by recalling that $u_\tau = \sqrt{\tau_w/\rho}$ one has for the channel flow:

$$-\frac{dp}{dx} = \frac{\tau_w}{h} = \frac{\rho u_\tau^2}{h} \quad (2.57)$$

where one can also demonstrate that the axial pressure gradient dp/dx is uniform across the flow. By recalling the nondimensionalization (2.2), Equation (2.57) can be rewritten as:

$$\frac{d\left(\frac{p}{\rho u_\tau^2}\right)}{d(x/h)} = \frac{dp^*}{dx^*} = -1 \quad (2.58)$$

and, since the mean axial pressure gradient is uniform across the flow:

$$\Delta p^* = p_{in}^* - p_{out}^* = \int dx^* = L^* \quad (2.59)$$

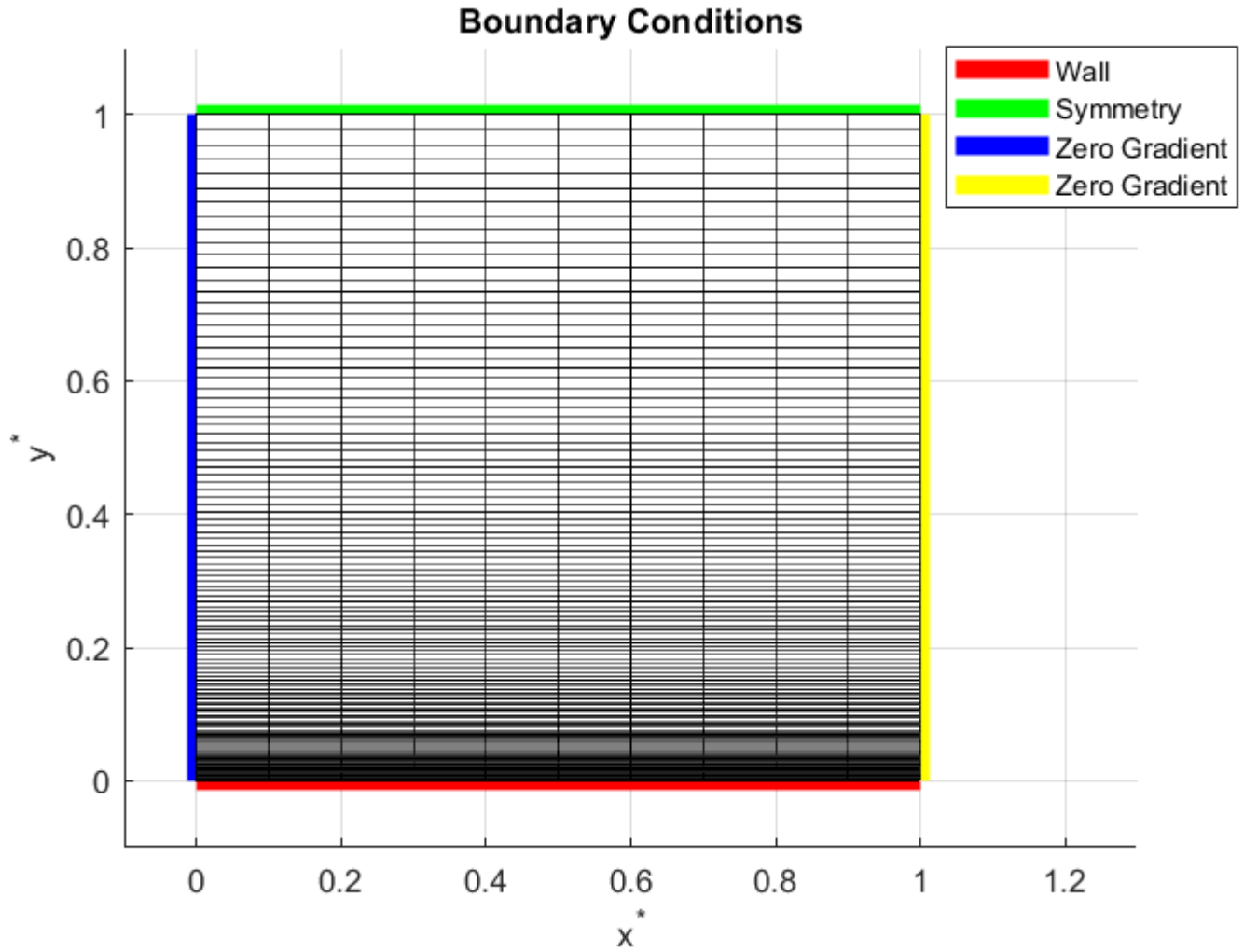


Figure 18: Channel flow boundary conditions

where L^* is the length of the channel portion simulated - in this case $L^* = 1$.

Another important aspect to mention is the 'relative' nature of pressure in the Marker and Cell method. Indeed, from the passages above, it emerges clearly that the computation of the pressure field represents simply an intermediate step for the computation of the velocity field. One can observe that equation (2.44) yields infinite solutions when only one boundary condition is specified, all of them differing for a constant (??). Hence, unless the value of the actual pressure field is of interest, the solution of the Poisson equation can be regarded as a 'pseudo-pressure' field that leads to the solution of the real velocity field. In (2.21) and (2.26), only the gradients of the 'pseudo-pressure' field are involved, thus all the solutions of the Poisson equation produce the same effect on the computation of the velocity components. As a consequence, the values of the pressure imposed at the inlet and at the outlet of the domain are not relevant, it is only their relation (2.59) that matters and that must be satisfied.

In order to enforce the boundary conditions sketched in Fig.(18), it is convenient to define an additional layer of cells outside the physical domain. We will refer to those control volumes as *ghost cells*. The velocity components u and v , the pressure and the turbulence quantities in correspondence of the ghost cell will be computed by directly enforcing the corresponding boundary conditions, as it will be explained in the following section. Another possibility would consist in modifying expressions (2.21), (2.26), (2.31) and (2.36) in correspondence of the boundary cells through the relations derived by the boundary conditions. It is however much easier to extend the computational domain of one layer of cells and to use the same expressions for each cell of the internal grid. A simplified scheme -with uniform cells - of the resulting grid is sketched in the Fig.19, where the ghost cell layer is drawn with the red color.

$\cdot (0, N_y + 1)$	\cdot	\cdot	\cdot	$(N_x + 1, N_y + 1)$
\cdot	$(1, N_y)$ \cdot	\cdot	(N_x, N_y) \cdot	\cdot
\cdot	\cdot	\cdot	\cdot	\cdot
\cdot	\cdot	\cdot	\cdot	\cdot
\cdot	\cdot	\cdot	\cdot	\cdot
\cdot	\cdot	\cdot	\cdot	\cdot
\cdot	\cdot	\cdot	\cdot	\cdot
\cdot	\cdot	\cdot	\cdot	\cdot
\cdot	$\cdot (1, 1)$	\cdot	$\cdot (N_x, 1)$	\cdot
$\cdot (0, 0)$	\cdot	\cdot	\cdot	\cdot

Figure 19: Ghost cells

In the following paragraphs, a detailed explanation of the four boundary conditions will be presented. Since $\mathbf{U} = (u, v)$ is a two-dimensional vector, the boundary conditions have to be specified for: each component of the velocity vector; the pressure; the turbulent kinetic energy; the dissipation rate; the components of the anisotropy stress tensor.

1) Wall boundary condition $y^* = 0$

First of all, we need to derive the continuous boundary conditions for all the quantities involved. After that, these expressions will be discretized so that they can be enforced numerically in the solver.

In correspondence of a wall, the velocity boundary conditions derive from the no-slip and the no-

compensation condition. In particular, the first one implies that, in correspondence of each wall, the fluid velocity's component parallel to the wall must be equal to the velocity of the wall itself (in this case 0). The second one implies that, in correspondence of each wall, the flow velocity's component normal to the wall must be null, since no outgoing or ingoing mass flow rate is allowed by the solid boundary.

From the no-slip condition and from the impermeability condition, it is also possible to demonstrate that, in correspondence of a physical wall boundary, all the components of the Reynolds stress tensor are null. In particular, one has that for $y^* \rightarrow 0$:

$$\begin{aligned}\langle u^2 \rangle &\sim y^2 \\ \langle v^2 \rangle &\sim y^4 \\ \langle w^2 \rangle &\sim y^2 \\ \langle uv \rangle &\sim y^3\end{aligned}\tag{2.60}$$

and therefore for $y^* = 0$ all the anisotropy stress tensor components satisfy $a_{ij}(y^* = 0) = 0$. Moreover, since the turbulent kinetic energy, corresponds to half of the trace of the Reynolds stress tensor, then also $k(y^* = 0) = 0$.

Lastly, from the prescriptions of the Abe-Kondoh-Nagano model, one has:

$$\varepsilon(y = 0) = 2\nu \left(\frac{\partial k}{\partial y} \right)_{y=0}^2$$

which differs from the dissipation rate boundary condition that would normally derive by the k transport equation:

$$\varepsilon(y = 0) = \nu \frac{d^2 k}{dy^2}$$

due to the introduction of the blending coefficients f_1 and f_2 in the ε transport equation, that affect the expression near the wall.

The boundary conditions on pressure are derived from the Momentum Equations in correspondence of the four walls and by combining the velocity boundary conditions.

The Momentum equation along y of the Navier-Stokes system written in non-conservative form is:

$$\frac{\partial v}{\partial t} + u \frac{\partial v}{\partial x} + v \frac{\partial v}{\partial y} + \frac{1}{\rho} \frac{\partial p}{\partial y} + \frac{2}{3} \frac{\partial k}{\partial y} = \nu \left(\frac{\partial^2 v}{\partial x^2} + \frac{\partial^2 v}{\partial y^2} \right) - \left(\frac{\partial a_{xy}}{\partial x} - \frac{\partial a_{yy}}{\partial y} \right)\tag{2.61}$$

Yet, in correspondence of the horizontal bottom wall $v=0$, $\frac{\partial v}{\partial x} = 0$, $a_{ij} = 0$, $k=0$. Hence (2.61) becomes for the $y=0$ wall:

$$\frac{\partial p}{\partial y} = \rho \nu \frac{\partial^2 v}{\partial y^2} = \mu \frac{\partial^2 v}{\partial y^2}\tag{2.62}$$

It is interesting to notice that the boundary condition for the pressure involves the velocity field.

Now, by recalling all the reasoning above, the bottom wall boundary condition at $y^* = 0$ can be expressed as:

$$\left\{ \begin{array}{l} u = 0 \\ v = 0 \\ \frac{\partial p}{\partial y} = \mu \frac{\partial^2 v}{\partial y^2} \\ k = 0 \\ a_{ij} = 0 \\ \varepsilon = 2\nu \left(\frac{\partial k}{\partial y} \right)_{y=0}^2 \end{array} \right. \quad (2.63)$$

By introducing the nondimensionalization parameters (2.2), the set of boundary conditions (2.63) can be nondimensionalized as follows:

$$\left\{ \begin{array}{l} u^* = 0 \\ v^* = 0 \\ \frac{\partial p^*}{\partial y^*} = \frac{1}{Re} \frac{\partial^2 v^*}{\partial y^{*2}} \\ k^* = 0 \\ a_{ij}^* = 0 \\ \varepsilon^* = \frac{2}{Re} \left(\frac{\partial k^*}{\partial y^*} \right)_{y^*=0}^2 \end{array} \right. \quad (2.64)$$

Equations (2.64) correspond to the nondimensional boundary conditions on the bottom wall. As mentioned earlier, the boundary conditions are enforced by adding an extra layer of ghost cells. In this way, the expressions (2.21), (2.26) and so on must not be modified for the boundary cells since the equations will simply access the values of ghost cells. Now (2.64) must be discretized in order to derive relations to enforce on the ghost cells of the bottom wall.

In the following Fig.(20) the cells involved in the following discussion are sketched:

For ease of writing, in the following discretizations the suffix * will be omitted. However, all the discretization are performed on the nondimensional quantities.

The boundary condition (2.64) on v leads to:

$$v_{i,\frac{1}{2}} = 0$$

From a simple interpolation, the boundary condition (2.63) on u leads to:

$$u_{wall,i+\frac{1}{2}} = \frac{u_{i+\frac{1}{2},0} + u_{i+\frac{1}{2},1}}{2}$$

(2,i-1) .	(2,i) .	(2,i+1) .
(1,i-1) .	(1,i) .	(1,i+1) .
(0,i-1) .	(0,i) .	(0,i+1) .

Figure 20: Ghost cells for bottom wall boundary condition

from which for the ghost cell:

$$u_{i+\frac{1}{2},0} = 2u_{wall,i+\frac{1}{2}} - u_{i+\frac{1}{2},1} = -u_{i+\frac{1}{2},1}$$

For the pressure instead, by recalling the continuity equation of (2.1) one has:

$$\frac{\partial p}{\partial y} = \frac{1}{Re} \frac{\partial^2 v}{\partial y^2} = \frac{1}{Re} \frac{\partial}{\partial y} \left(\frac{\partial v}{\partial y} \right) = \frac{1}{Re} \frac{\partial}{\partial y} \left(-\frac{\partial u}{\partial x} \right) = -\frac{1}{Re} \frac{\partial}{\partial x} \left(\frac{\partial u}{\partial y} \right)$$

from which:

$$\left[\frac{\partial p}{\partial y} = -\frac{1}{Re} \frac{\partial}{\partial x} \left(\frac{\partial u}{\partial y} \right) \right]_{i,\frac{1}{2}}$$

By discretizing the equation above in correspondance of the wall with a Central-Space scheme one obtains:

$$\frac{p_{i,1} - p_{i,0}}{\Delta y} = -\frac{1}{Re} \frac{\left(\frac{\partial u}{\partial y} \right)_{i+\frac{1}{2},\frac{1}{2}} - \left(\frac{\partial u}{\partial y} \right)_{i-\frac{1}{2},\frac{1}{2}}}{\Delta x} = -\frac{1}{Re} \frac{\left(u_{i+\frac{1}{2},1} - u_{i+\frac{1}{2},0} \right) - \left(u_{i-\frac{1}{2},1} - u_{i-\frac{1}{2},0} \right)}{\Delta x \Delta y}$$

and applying the Boundary Condition on u mentioned above:

$$\frac{p_{i,1} - p_{i,0}}{\Delta y} = -\frac{2}{Re} \frac{u_{i+\frac{1}{2},1} - u_{i-\frac{1}{2},1}}{\Delta x \Delta y} + \frac{2}{Re} \frac{u_{wall,i+\frac{1}{2}} - u_{wall,i-\frac{1}{2}}}{\Delta x \Delta y}$$

where $\Delta x = x_{0,i+\frac{1}{2}} - x_{0,i-\frac{1}{2}}$ and $\Delta y = y_{1,i} - y_{0,i}$.

Now, by applying the Continuity Equation on the cell (i,1) and the Boundary Condition on v mentioned above:

$$\frac{u_{i+\frac{1}{2},1} - u_{i-\frac{1}{2},1}}{\Delta x} = -\frac{v_{i,\frac{3}{2}} - v_{i,\frac{1}{2}}}{\Delta y} = -\frac{v_{i,\frac{3}{2}}}{\Delta y}$$

By substituting above and recalling that $\Delta x = \Delta y$ one has:

$$p_{i,0} = p_{i,1} - \frac{2}{Re} \frac{v_{i,\frac{3}{2}}}{\Delta y} - \frac{2}{Re} \frac{u_{wall,i+\frac{1}{2}} - u_{wall,i-\frac{1}{2}}}{\Delta y} = p_{i,1} - \frac{2}{Re} \frac{v_{i,\frac{3}{2}}}{\Delta y}$$

Since the turbulent kinetic energy and the anisotropy stress tensor components of the ghost cell (0,i) are defined in correpsondence of the wall - at position $\left(\frac{1}{2}, i + \frac{1}{2} \right)$, their discretized boundary condition follows immediately:

$$k_{\frac{1}{2},i+\frac{1}{2}} = 0$$

$$a_{ij,\frac{1}{2},i+\frac{1}{2}} = 0$$

Lastly, for the dissipation rate one has:

$$\varepsilon_{\frac{1}{2},i+\frac{1}{2}} = \frac{2}{Re} \left(\frac{\sqrt{k_{\frac{3}{2},i+\frac{1}{2}}} - \sqrt{k_{-\frac{1}{2},i+\frac{1}{2}}}}{y_{\frac{3}{2},i+\frac{1}{2}} - y_{-\frac{1}{2},i+\frac{1}{2}}} \right)^2$$

where the index $j = -\frac{1}{2}$ is out of the geometric domain. However, since k is half the trace of the Reynolds stress tensor, from (2.60) one has that $k \sim y^2$ for $y \rightarrow 0$. Hence, using a centered-difference scheme:

$$\frac{k_{\frac{3}{2},i+\frac{1}{2}} - k_{-\frac{1}{2},i+\frac{1}{2}}}{y_{\frac{3}{2},i+\frac{1}{2}} - y_{-\frac{1}{2},i+\frac{1}{2}}} = 0$$

from which:

$$k_{\frac{3}{2},i+\frac{1}{2}} = -k_{-\frac{1}{2},i+\frac{1}{2}}$$

and therefore:

$$\varepsilon_{\frac{1}{2},i+\frac{1}{2}} = 0$$

To sum up, discretizing boundary conditions (2.64) for the bottom wall leads to the following relations to enforce at a generic bottom cell (0,i):

$$\left\{ \begin{array}{l} u_{i+\frac{1}{2},0} = -u_{i+\frac{1}{2},1} \\ v_{i,\frac{1}{2}} = 0 \\ p_{i,0} = p_{i,1} - \frac{2}{Re} \frac{v_{i,\frac{3}{2}}}{y_{1,i} - y_{0,i}} \\ k_{\frac{1}{2},i+\frac{1}{2}} = 0 \\ a_{ij,\frac{1}{2},i+\frac{1}{2}} = 0 \\ \varepsilon_{\frac{1}{2},i+\frac{1}{2}} = 0 \end{array} \right. \quad (2.65)$$

2) Symmetry boundary condition $y^* = 1$

As before, first the continuous boundary conditions will be derived for all the quantities and , after that, the expressions will be discretized for the layer of ghost cells. In correspondence of the channel axis, the profile of all the quantities are specular due to the symmetry of the problem. Mathematically, this constraint translates into a zero-gradient condition for all the variables, except the component v of the velocity which is normal to the channel axis. Again, due to the symmetry of the problem, the component of velocity normal to the symmetry axis -here v - must be null.

Recalling the reasoning above, the top symmetry boundary condition at $y^* = 1$ can be expressed as:

$$\left\{ \begin{array}{l} \frac{\partial u}{\partial y} = 0 \\ v = 0 \\ \frac{\partial p}{\partial y} = 0 \\ \frac{\partial k}{\partial y} = 0 \\ \frac{\partial a_{ij}}{\partial y} = 0 \\ \frac{\partial \varepsilon}{\partial y} = 0 \end{array} \right. \quad (2.66)$$

By introducing the nondimensionalization parameters (2.2), the set of boudary conditions (2.63) can be nondimensionalized as follows:

$$\left\{ \begin{array}{l} \frac{\partial u^*}{\partial y^*} = 0 \\ v^* = 0 \\ \frac{\partial p^*}{\partial y^*} = 0 \\ \frac{\partial k^*}{\partial y^*} = 0 \\ \frac{\partial a_{ij}^*}{\partial y^*} = 0 \\ \frac{\partial \varepsilon^*}{\partial y^*} = 0 \end{array} \right. \quad (2.67)$$

Now (2.67) must be discretized in order to derive relations to enforce on the ghost cells of the top boundary of the domain. In the following Fig.(21) the cells involved in the following discussion are sketched:

$(N_y+1, i-1)$.	(N_y+1, i) .	$(N_y+1, i+1)$.
$(N_y, i-1)$.	(N_y, i) .	$(N_y, i+1)$.
$(N_y-1, i-1)$.	(N_y-1, i) .	$(N_y-1, i+1)$.

Figure 21: Ghost cells for top symmetry boundary condition

For ease of writing, in the following discretizations the suffix * will be omitted. However, all the discretization are performed on the nondimensional quantities.

The boundary condition (2.67) on v leads to:

$$v_{N_y+1,i} = 0$$

whereas the zero-gradient condition on u is discretized as:

$$\frac{u_{N_y+1,i+\frac{1}{2}} - u_{N_y,i+\frac{1}{2}}}{y_{N_y+1,i+\frac{1}{2}} - y_{N_y,i+\frac{1}{2}}} = 0$$

from which:

$$u_{N_y+1,i+\frac{1}{2}} = u_{N_y,i+\frac{1}{2}}$$

Analogue zero-gradient boundary condition applied on k leads to:

$$\frac{k_{N_y+\frac{3}{2},i+\frac{1}{2}} - k_{N_y+\frac{1}{2},i+\frac{1}{2}}}{y_{N_y+\frac{3}{2},i+\frac{1}{2}} - y_{N_y+\frac{1}{2},i+\frac{1}{2}}} = 0$$

from which it follows:

$$k_{N_y+\frac{3}{2},i+\frac{1}{2}} = k_{N_y+\frac{1}{2},i+\frac{1}{2}}$$

A similar condition to the one above applies to ε and a_{ij} , since like k they are defined at the cell vertex.

Lastly, the zero-gradient condition applied to the pressure leads to:

$$p_{N_y+1,i} = p_{N_y,i}$$

To sum up, discretizing boundary conditions (2.67) for the top boundary leads to the following relations to enforce at a generic ghost cell $(N_y + 1, i)$:

$$\left\{ \begin{array}{l} u_{N_y+1,i+\frac{1}{2}} = u_{N_y,i+\frac{1}{2}} \\ v_{N_y+1,i} = 0 \\ p_{N_y+1,i} = p_{N_y,i} \\ k_{N_y+\frac{3}{2},i+\frac{1}{2}} = k_{N_y+\frac{1}{2},i+\frac{1}{2}} \\ a_{ij,N_y+\frac{3}{2},i+\frac{1}{2}} = a_{ij,N_y+\frac{1}{2},i+\frac{1}{2}} \\ \varepsilon_{N_y+\frac{3}{2},i+\frac{1}{2}} = \varepsilon_{N_y+\frac{1}{2},i+\frac{1}{2}} \end{array} \right. \quad (2.68)$$

3) Zero-gradient boundary condition $x^* = 0$

As before, first the continuous boundary conditions will be derived for all the quantities and , after that, the expressions will be discretized for the layer of ghost cells. In correspondence of the inlet boundary of the domain a zero-gradient boundary condition is applied to all the variables except the pressure. Indeed, the flow is simulated in the fully developed region in which the quantities do not vary along the axial direction, their gradient along x being null. The pressure represents the only variable with a non null variation along x since a negative pressure gradient dp/dx is necessary to drive the flow in the channel. As for the inlet value of the pressure $p_{in} = p_{x=0}$, the relative nature of the pressure has already been discussed above. Since only the gradient of the pressure field affect the computation of u and v - (2.21), (2.26) - then the actual value of the pressure p_{in} is irrelevant. What really matters is that the pressure at the inlet and the one at the outlet satisfy (2.59). Recalling the reasoning above, the left zero-gradient condition at $x^* = 0$ can be expressed as:

$$\left\{ \begin{array}{l} \frac{\partial u}{\partial x} = 0 \\ \frac{\partial v}{\partial x} = 0 \\ p = p_{in} \\ \frac{\partial k}{\partial x} = 0 \\ \frac{\partial a_{ij}}{\partial x} = 0 \\ \frac{\partial \varepsilon}{\partial x} = 0 \end{array} \right. \quad (2.69)$$

where the value of p_{in} can be chosen arbitrarily.

By introducing the nondimensionalization parameters (2.2), the set of boudary conditions (2.63) can be nondimensionalized as follows:

$$\left\{ \begin{array}{l} \frac{\partial u^*}{\partial x^*} = 0 \\ \frac{\partial v^*}{\partial x^*} = 0 \\ p^* = p_{in}^* \\ \frac{\partial k^*}{\partial x^*} = 0 \\ \frac{\partial a_{ij}^*}{\partial x^*} = 0 \\ \frac{\partial \varepsilon^*}{\partial x^*} = 0 \end{array} \right. \quad (2.70)$$

Now (2.70) must be discretized in order to derive relations to enforce on the ghost cells of the left inlet boundary of the domain. In the following Fig.(22) the cells involved in the following discussion are sketched:

$(j+1,0)$	$(j+1,1)$	$(j+1,2)$
$(j,0)$	$(j,1)$	$(j,2)$
$(j-1,0)$	$(j-1,1)$	$(j-1,2)$

Figure 22: Ghost cells for left zero-gradient boundary condition

For ease of writing, in the following discretizations the suffix * will be omitted. However, all the discretization are performed on the nondimensional quantities.

The boundary condition (2.70) on u leads to:

$$\frac{u_{j,\frac{3}{2}} - u_{j,\frac{1}{2}}}{x_{j,\frac{3}{2}} - x_{j,\frac{1}{2}}} = 0$$

from which:

$$u_{j,\frac{1}{2}} = u_{j,\frac{3}{2}}$$

Similarly, for the v component of velocity one has:

$$v_{j+\frac{1}{2},0} = v_{j+\frac{1}{2},1}$$

Analogue zero-gradient boundary condition applied on k leads to:

$$\frac{k_{j+\frac{1}{2},\frac{3}{2}} - k_{j+\frac{1}{2},\frac{1}{2}}}{x_{j+\frac{1}{2},\frac{3}{2}} - x_{j+\frac{1}{2},\frac{1}{2}}} = 0$$

from which it follows:

$$k_{j+\frac{1}{2},\frac{3}{2}} = k_{j+\frac{1}{2},\frac{1}{2}}$$

A similar condition to the one above applies to ε and a_{ij} , since like k they are defined at the cell vertex.

Lastly, the inlet boundary condition applied to the pressure leads to:

$$p_{N_y+1,i} = p_{in}$$

To sum up, discretizing boundary conditions (2.67) for the top boundary leads to the following relations to enforce at a generic ghost cell $(j, 0)$:

$$\left\{ \begin{array}{l} u_{j, \frac{1}{2}} = u_{j, \frac{3}{2}} \\ v_{j+\frac{1}{2}, 0} = v_{j+\frac{1}{2}, 1} \\ p_{N_y+1, i} = p_{in} \\ k_{j+\frac{1}{2}, \frac{3}{2}} = k_{j+\frac{1}{2}, \frac{1}{2}} \\ a_{ij, j+\frac{1}{2}, \frac{3}{2}} = a_{ij, j+\frac{1}{2}, \frac{1}{2}} \\ \varepsilon_{j+\frac{1}{2}, \frac{3}{2}} = \varepsilon_{j+\frac{1}{2}, \frac{1}{2}} \end{array} \right. \quad (2.71)$$

4) Zero-gradient boundary condition $x^* = 1$

For the right boundary of the domain at $x^* = 1$, the boundary condition is analogue to the one enforced at $x^* = 0$ boundary. In correspondence of the outlet boundary of the domain a zero-gradient boundary condition is applied to all the variables except the pressure, which must satisfy (2.59). The set of nondimensional boundary conditions is equivalent to (2.69), except for the pressure. By recalling (2.59), one has:

$$p^* = p_{out}^* = p_{in}^* - 1 \quad (2.72)$$

since the horizontal size of the domain L has been chosen $L = h$, where h corresponds also to the characteristic length of the problem.

The derivation of the discrete boundary condition for the right outlet boundary is analogue to the one already performed on the inlet boundary and therefore will be omitted.

In the following Fig.(22) the cells involved in the discretization are sketched:

$(j+1, N_x-1)$	$(j+1, N_x)$	$(j+1, N_x+1)$
(j, N_x-1)	(j, N_x)	(j, N_x+1)
$(j-1, N_x-1)$	$(j-1, N_x)$	$(j-1, N_x+1)$

Figure 23: Ghost cells for left zero-gradient boundary condition

The discretization of the continuous outlet zero-gradient boundary condition on the right boundary of

the domain leads to the following conditions to enforce at generic ghost cell $(j, N_x + 1)$:

$$\left\{ \begin{array}{l} u_{j, N_x + \frac{3}{2}} = u_{j, N_x + \frac{1}{2}} \\ v_{j + \frac{1}{2}, N_x} = v_{j + \frac{1}{2}, N_x + 1} \\ p_{N_y + 1, i} = p_{in} - 1 \\ k_{j + \frac{1}{2}, N_x + \frac{3}{2}} = k_{j + \frac{1}{2}, N_x + \frac{1}{2}} \\ a_{ij, j + \frac{1}{2}, N_x + \frac{3}{2}} = a_{ij, j + \frac{1}{2}, N_x + \frac{1}{2}} \\ \varepsilon_{\frac{1}{2}, N_x + \frac{3}{2}} = \varepsilon_{j + \frac{1}{2}, N_x + \frac{1}{2}} \end{array} \right. \quad (2.73)$$

2.2.3 Validation of the solver

Before trying to embed a neural network, it has to be ensured that the standard version of the solver -the one using the Linear Eddy Viscosity Model- yields satisfactory results.

The validation case chosen is the turbulent channel flow at $Re_\tau = 544$ or equivalently $Re_\delta = 10000$.

The choiche was motivated by the following facts:

- The application of the neural network will be tested on the same flow, hence the code can be reused by just replacing the LEVM with the machine learning architecture.
- The turbulent channel flow is a canonical flow which has been extensively studied numerically. Indeed, it is the first class of flows to which DNS methods were applied. As a result, it has been used for long time as a benchmark problem to test and validate numerical CFD solvers and a wide literature of results is available for comparing the results obtained [6].

Most of the results for the turbulent channel flow cases available in literature derive from the application of DNS methods [6]. Benchmark data obtained with RANS $k - \varepsilon$ methods are quite rare. In particular, no available data obtained with the same low-Re Abe-Kondoh-Nagano model have been found. However, in many publications it is shown that the model yields satisfactory results - comparable to a DNS - for most of the turbulent quantities and for the mean axial velocity [27], [24].

Consequently, when validating the code, the following aspects must be looked upon:

1. The mean adimensional velocity $u^+(y^+)$ profile must be close to the reference DNS one.
2. The tubulent quantities $\langle uv \rangle(y^+)$ and $k(y^+)$ profiles must be close to the reference DNS one.
3. The value:

$$\kappa = \frac{1}{y^+} \left(\frac{du^+}{dy^+} \right)^{-1} \quad (2.74)$$

must be approximately constant in the log-law region - for $y^+ > 30$. Such a value is called von Karman constant [38] and it is characteristic of the log-law region of wall bounded flows where the following expression holds for the mean axial velocity:

$$u^+ = \frac{1}{\kappa} \ln y^+ + B \quad (2.75)$$

where both κ and B are constants. In literature, there is some variation in the values ascribed to the log-law von Karman constant, but it proves being near the value 0.41 for a broad range of Reynolds numbers. Equation (2.75) holds for a big portion of the height of the channel for low-Reynolds flows, however near the channel's mid-plane the velocity profile deviates from (2.75).

The results of the solver are shown in the following charts and compared with the reference DNS data available. In Fig.(24) and Fig.(25), the mean velocity profile is analyzed, both in dependence on y^+ and y/δ . The plot in Fig.(24) is logarithmic as in standard charts, in order to highlight the logarithmic trend of velocity in the log-law region. In fig (26), the profiles of turbulent kinetic energy and of $\langle uv \rangle$ Reynolds stress are compared to their DNS counterpart. Lastly, in (27), the computed value of (2.74) is plotted.

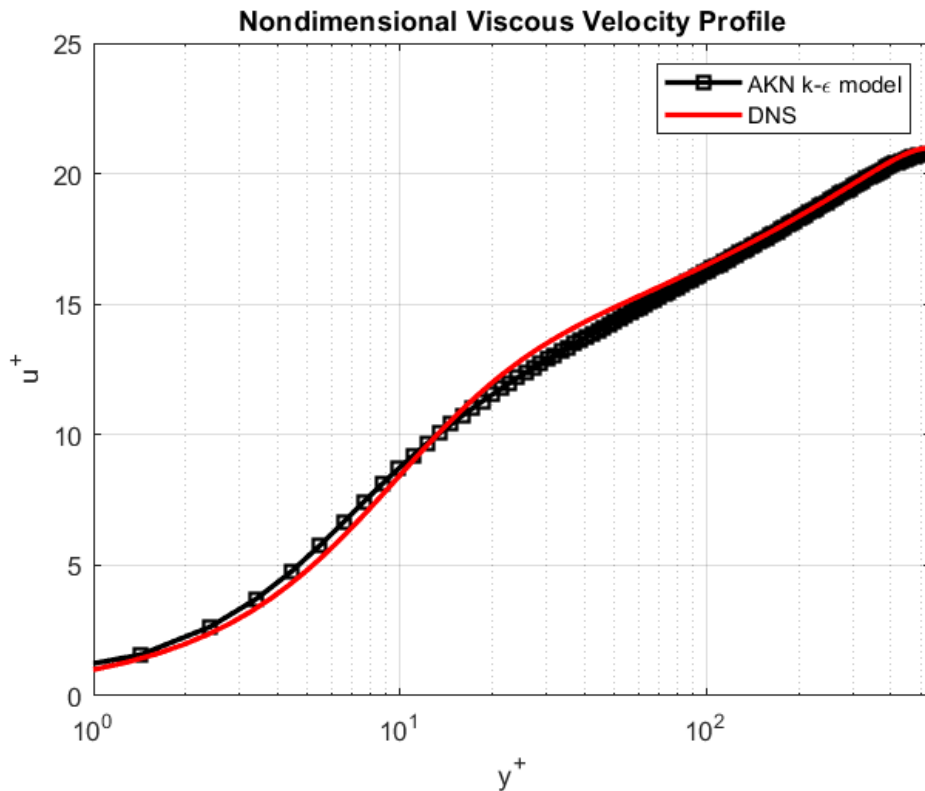
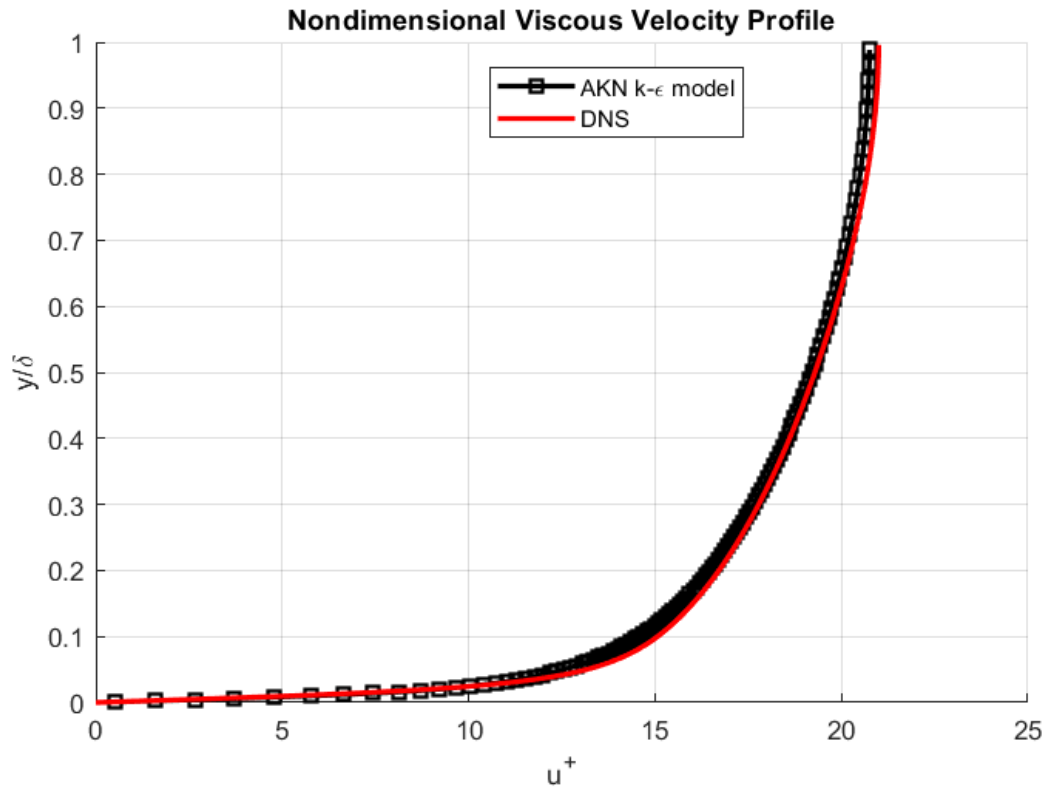
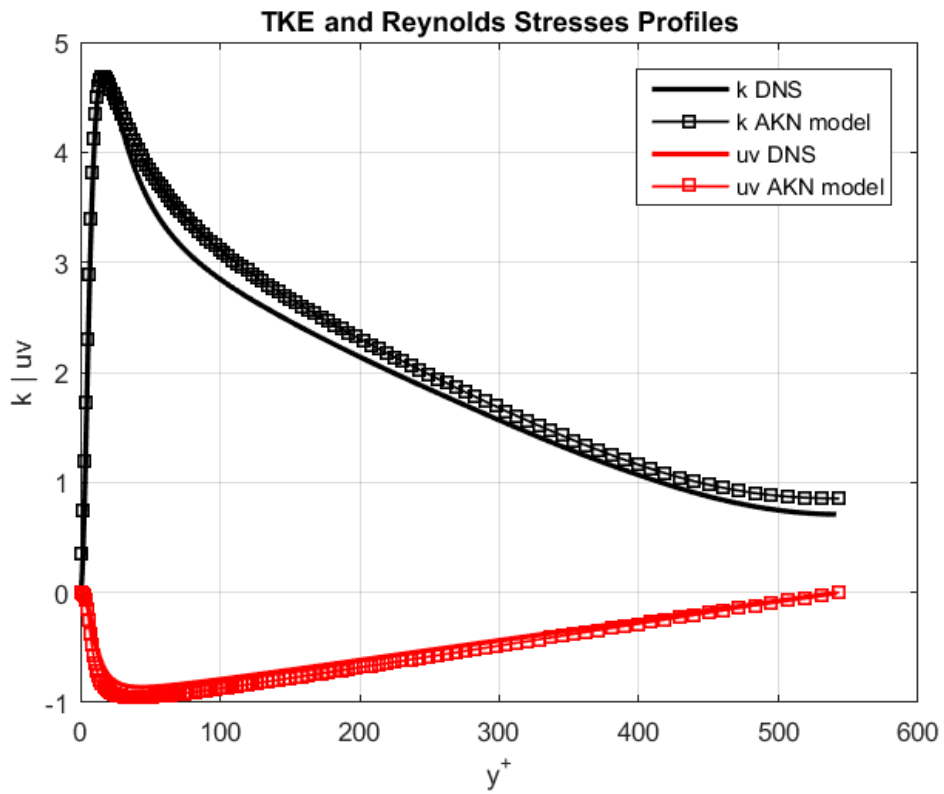


Figure 24: Solver validation: Channel flow $u^+(y^+)$ profile

Figure 25: Solver validation: Channel flow $u^+(y/\delta)$ profileFigure 26: Solver validation: Channel flow $k^+(y^+)$ and $\langle uv(y^+) \rangle$ profiles

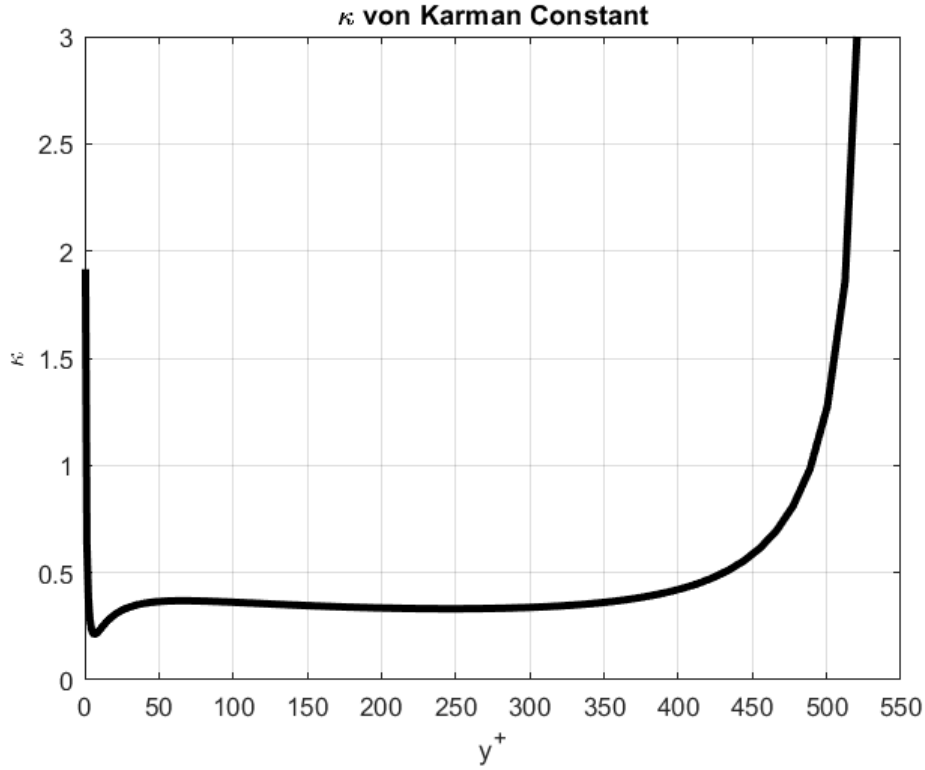


Figure 27: Solver validation: von Karman constant

From the charts above, we can observe that the results obtained are fully satisfactory. Indeed:

- The solver gives an acceptable prediction of the axial velocity profile. One must also consider that the benchmark data derive from a DNS and therefore a small discrepancy between them and the RANS results obtained is to be expected.
- Despite a small discrepancy compared to the DNS profile, the model predicts successfully the peak of turbulent kinetic energy and its global trend across channel's height. The turbulent shear stress $\langle uv \rangle$ is accurately predicted as well.
- The value computed for (2.74) is almost constant in a broad range of the channel's height, in particular for $y^+ > 30$ - the log-law region. As expected, κ deviates from the log-law value approaching the channel's mid-plane.

2.3 Artificial Neural Network

In this section, further details will be given about the building and training of the Tensor Basis Neural Network used to replace the LEVM in the solver. The network introduced in Chapter 1 has been

implemented in Python, using Keras library [32] with Tensorflow backend. The choice is motivated by the fact that the network has a very standard layers' architecture (feed-forward, fully connected) and Keras provides many tools to easily build canonical networks. Moreover, at the time of the work, Tensorflow is among the most used libraries for machine learning techniques.

In the following table, the key terminology of neural networks is introduced:

TABLE I: NEURAL NETWORKS' KEY TERMINOLOGY

TERM	EXPLANATION
Layer	A vector-valued variable serving as input, output, or intermediate output in a neural network
Node	Individual element of a vector represented by a layer
Fully connected network	Each neuron receives input from every element of the previous layer
Feed-forward network	Network wherein the connections between the nodes do not form a cycle
Activation Function	Function applied to the output of a layer element-wise
Model Parameters	Nodes' weights and biases tuned during training
Loss function	A scalar-valued function to be minimized during the training process
Learning rate	Step size of the iterative gradient-based optimization algorithm
Epoch	A full pass through all training data in stochastic algorithms
Optimizer	Method used to find the model parameters that minimize the loss function
Batch size	Data points used to estimate the gradient in one iteration of the optimizer
Model hyperparameters	Parameters defining the configuration of a neural network and of the training process, such as the number of hidden layers, the number of nodes per layers, activation functions, learning rate..
Train dataset	Data using during training to optimize model parameters
Validation dataset	Data used to evaluate the performance of the model at each iteration
Overfitting	The network fits the training data very well but not the validation data
Early Stopping	technique that controls the training time to prevent overfitting

2.3.1 High-Fidelity datasets

With the terminology introduced above, we are now ready to introduce the deep neural network described in Chapter 1. The Tensor Basis Neural Network (TBNN) has two input layers: the five invariants input layers -main input - and the ten basis tensors input layers. A series of hidden layers is used to predict coefficient $g^{(n)}$ for $n=1,..10$ of (1.29). The tensor basis input layer is composed by the 10 invariant tensors $\mathbf{T}^{(n)}$ for $n=1,..10$ of (1.29) from the five invariants λ_i . The merge output layer takes the element-wise products of the final hidden layer and of the basis tensors input layer and sums the results to give the final prediction for \mathbf{b} - which is the same as taking the dot product between the two layers [9]. All the quantities mentioned - the five invariants, the tensor basis, the nondimensional anisotropy tensor - are derived from DNS or highly resolved LES datasets. Since the relation sought by the model has the aspiration of generality, the flows database used represents a wide variety of different flow configurations. We are therefore testing the ability of the neural network to do more than just interpolate between similar flow configurations at different Reynolds numbers; we are evaluating the ability of the neural network to learn about the underlying flow regimes present in these configurations [9].

The nine flows in the database were selected because of the availability of high-fidelity data and because they represent canonical flow cases. All of the high-fidelity simulation results have been previously reported in the literature. The same dataset has been used both for training and validation, with a train-validation split factor of 0.8 as is common practice. In the following table, the flows composing the dataset are listed:

TABLE II: NEURAL NETWORK'S TRAINING AND VALIDATION DATASET

Flow type	Simulation	Reynolds	Source
Flow in a Square Duct	DNS	$Re_\tau = 600$	[5]
Hot Jet in Cold Channel Crossflow	DNS	$Re = 3333$	[1]
Converging-Diverging Channel	DNS	$Re = 12600$	[4]
Periodic Hill	LES	$Re = 10595$	[2]
Curved Backward-Facing Step	LES	$Re = 13700$	[3]
Channel Flow	DNS	$Re_\tau = 5200$	[6]
Boundary Layer Flow	DNS	$Re_\theta = 4060$	[7]
Couette Flow	DNS	$Re_\tau = 500$	[8]

Of course, due to the different complexity of the flows, a different number of observations has been used for each class of flows depending on the available data. For example, in the channel flow case there is only one direction along which the quantities vary - the one normal to the plates - and therefore only around 750 different points with different values were available. On the other side, the Hot Jet in Cold Channel Crossflow is a 3D simulation (actually all DNS simulations are 3D but in some cases the variation of the statistics occurs only along one or two directions) and therefore many more data points were included in the dataset - around 160000.

2.3.2 Input layers' normalizations

The data listed in Table II were not directly inputted into the neural network. Indeed, it is an usual practice in machine learning algorithms to perform a data normalization first when features may have different ranges of values [35].

As mentioned above, to ensure non-dimensionality of the raw inputs, the normalization scheme for the mean rate of strain $\langle \mathbf{S} \rangle$ (1.25) and rate of rotation $\langle \mathbf{R} \rangle$ (1.26) tensors proposed by Pope is adopted. In this way, all raw features are normalized by local quantities, as is preferred in the practice of traditional turbulence modeling. In CFD simulations these would be quantities based on the same grid point as the raw feature variable. Now, since all components of the nondimensional Reynolds stress tensor lie in the range $[-1/2, 2/3]$, the basis tensors have been normalized in the following way:

$$\begin{aligned}
 \tilde{\mathbf{T}}^{(1)} &= \frac{1}{a} [\langle \mathbf{s} \rangle] = \frac{1}{a} \mathbf{T}^{(1)} & \tilde{\mathbf{T}}^{(6)} &= \frac{1}{ab^2} \left[\langle \mathbf{r} \rangle^2 \langle \mathbf{s} \rangle + \langle \mathbf{r} \rangle \langle \mathbf{s} \rangle^2 - \frac{2}{3} \mathbf{I} \cdot \text{Tr}(\langle \mathbf{s} \rangle \langle \mathbf{r} \rangle^2) \right] = \frac{1}{ab^2} \mathbf{T}^{(6)} \\
 \tilde{\mathbf{T}}^{(2)} &= \frac{1}{ab} [\langle \mathbf{s} \rangle \langle \mathbf{r} \rangle - \langle \mathbf{r} \rangle \langle \mathbf{s} \rangle] = \frac{1}{ab} \mathbf{T}^{(2)} & \tilde{\mathbf{T}}^{(7)} &= \frac{1}{ab^3} \left[\langle \mathbf{r} \rangle \langle \mathbf{s} \rangle \langle \mathbf{r} \rangle^2 - \langle \mathbf{r} \rangle^2 \langle \mathbf{s} \rangle \langle \mathbf{r} \rangle \right] = \frac{1}{ab^3} \mathbf{T}^{(7)} \\
 \tilde{\mathbf{T}}^{(3)} &= \frac{1}{a^2} \left[\langle \mathbf{s} \rangle^2 - \frac{1}{3} \mathbf{I} \cdot \text{Tr}(\langle \mathbf{s} \rangle^2) \right] = \frac{1}{a^2} \mathbf{T}^{(3)} & \tilde{\mathbf{T}}^{(8)} &= \frac{1}{a^3 b} \left[\langle \mathbf{s} \rangle \langle \mathbf{r} \rangle \langle \mathbf{s} \rangle^2 - \langle \mathbf{s} \rangle^2 \langle \mathbf{r} \rangle \langle \mathbf{s} \rangle \right] = \frac{1}{a^3 b} \mathbf{T}^{(8)} \\
 \tilde{\mathbf{T}}^{(4)} &= \frac{1}{b^2} \left[\langle \mathbf{r} \rangle^2 - \frac{1}{3} \mathbf{I} \cdot \text{Tr}(\langle \mathbf{r} \rangle^2) \right] = \frac{1}{b^2} \mathbf{T}^{(4)} & \tilde{\mathbf{T}}^{(9)} &= \frac{1}{a^2 b^2} \left[\langle \mathbf{r} \rangle^2 \langle \mathbf{s} \rangle^2 - \langle \mathbf{s} \rangle^2 \langle \mathbf{r} \rangle^2 - \frac{2}{3} \mathbf{I} \cdot \text{Tr}(\langle \mathbf{s} \rangle^2 \langle \mathbf{r} \rangle^2) \right] = \frac{1}{a^2 b^2} \mathbf{T}^{(9)} \\
 \tilde{\mathbf{T}}^{(5)} &= \frac{1}{a^2 b} \left[\langle \mathbf{r} \rangle \langle \mathbf{s} \rangle^2 - \langle \mathbf{s} \rangle^2 \langle \mathbf{r} \rangle \right] = \frac{1}{a^2 b} \mathbf{T}^{(5)} & \tilde{\mathbf{T}}^{(10)} &= \frac{1}{a^2 b^3} \left[\langle \mathbf{r} \rangle \langle \mathbf{s} \rangle^2 \langle \mathbf{r} \rangle^2 - \langle \mathbf{r} \rangle^2 \langle \mathbf{s} \rangle^2 \langle \mathbf{r} \rangle \right] = \frac{1}{a^2 b^3} \mathbf{T}^{(10)}
 \end{aligned}$$

where:

$$a = \sqrt{\frac{|\text{Tr}(\langle \mathbf{s} \rangle^2)|}{2}} \quad b = \sqrt{\frac{|\text{Tr}(\langle \mathbf{r} \rangle^2)|}{2}} \quad (2.76)$$

and where $\tilde{\mathbf{T}}^{(n)}$ refers to basis tensor $\mathbf{T}^{(n)}$ normalized through (2.76).

In order to justify the normalization described above, it is useful to provide an example with a generic

2D nondimensional mean strain rate tensor:

$$\langle \mathbf{s} \rangle^{2D} = \begin{bmatrix} s_{11} & s_{12} & 0 \\ s_{21} & s_{22} & 0 \\ 0 & 0 & 0 \end{bmatrix}$$

where $s_{12} = s_{21}$ due to symmetry and the zeros are due to the fact that in a 2D flow $u_3 = 0$ and $\frac{\partial}{\partial x_3} = 0$.

Now, using simple matrix multiplication:

$$\langle \mathbf{s} \rangle^2 = \langle \mathbf{s} \rangle^{2D} \langle \mathbf{s} \rangle^{2D} = \begin{bmatrix} s_{11}^2 + s_{12}^2 & s_{11}s_{12} + s_{12}s_{22} & 0 \\ s_{11}s_{12} + s_{12}s_{22} & s_{12}^2 + s_{22}^2 & 0 \\ 0 & 0 & 0 \end{bmatrix}$$

from which:

$$a = \sqrt{\frac{|\text{Tr}(\langle \mathbf{s} \rangle^2)|}{2}} = \sqrt{\frac{s_{11}^2 + 2s_{12}^2 + s_{22}^2}{2}}$$

and recalling the basis tensors normalization above:

$$\tilde{\mathbf{T}}^{(1)} = \frac{1}{a} [\langle \mathbf{s} \rangle] = \sqrt{\frac{2}{s_{11}^2 + 2s_{12}^2 + s_{22}^2}} \begin{bmatrix} s_{11} & s_{12} & 0 \\ s_{21} & s_{22} & 0 \\ 0 & 0 & 0 \end{bmatrix} \quad (2.77)$$

from which it emerges clearly that the components of the first basis tensor fall approximately in the interval $[-1,1]$. Since the components of \mathbf{b} - the output of the neural network - lie in the interval $[-1/2, 2/3]$ and since \mathbf{b} is expressed as a linear combination of the basis tensors, this seems a reasonable result for the normalization process. Indeed, using normalization factors (2.76) for the tensor basis, the Mean Squared Error of the network has been almost halved compared to the case of non-normalized inputs.

A crucial aspect to observe is that the normalization parameters (2.76) are functions of the invariants $\lambda_1 = \text{Tr}(\langle \mathbf{s} \rangle^2)$ and $\lambda_2 = \text{Tr}(\langle \mathbf{r} \rangle^2)$ introduced in (1.31). In particular:

$$a = \sqrt{\frac{|\lambda_1|}{2}} \quad b = \sqrt{\frac{|\lambda_2|}{2}}$$

As a result, the invariance properties embedded into the output tensor of the network are not lost. Indeed, the neural network tries to learn the relationship between the invariants and the ten coefficients of the basis tensors' linear combination $g^{(n)} = g^{(n)}(\lambda_i)$ where $n=1,2,\dots,10$ and $i=1,2,\dots,5$. Hence, one could think of the normalization above applied to the coefficients rather than the tensor basis. This means

that the function learned by the network is $\tilde{g}^{(n)} = \tilde{g}^{(n)}(\lambda_i)$ where:

$$\begin{aligned}\tilde{g}^{(1)} &= \frac{g^{(1)}}{a} & \tilde{g}^{(6)} &= \frac{g^{(6)}}{ab^2} \\ \tilde{g}^{(2)} &= \frac{g^{(2)}}{ab} & \tilde{g}^{(7)} &= \frac{g^{(7)}}{ab^3} \\ \tilde{g}^{(3)} &= \frac{g^{(3)}}{a^2} & \tilde{g}^{(8)} &= \frac{g^{(8)}}{a^3b} \\ \tilde{g}^{(4)} &= \frac{g^{(4)}}{b^2} & \tilde{g}^{(9)} &= \frac{g^{(9)}}{a^2b^2} \\ \tilde{g}^{(5)} &= \frac{g^{(5)}}{a^2b} & \tilde{g}^{(10)} &= \frac{g^{(10)}}{a^2b^3}\end{aligned}$$

where coefficients $\tilde{g}^{(n)}$ still depend only on invariants λ_i (since factors a,b are functions of them).

Another normalization as well- a standard one- was applied to the invariants input layers. In particular the z-scores normalization was chosen. Standardization or z-scores is one of the most common normalization methods. It converts all data to a common scale with an average of zero and standard deviation of one [36]. The choice of is justified by the practice of machine learning where the inputs are usually normalized to the range [-1, 1] or [0, 1]. This helps avoiding clustering of training data along certain directions within the input feature space and improves the convergence rate in the training process. The z-scores normalization was applied invariant by invariant; namely, it has been applied on all data points to each invariant λ_i separately. The standardization formula is the following:

$$\lambda_{i,j}^z = \frac{\lambda_{i,j} - \bar{\lambda}_i}{\sigma_i} \quad i = 1, 2, \dots, 5 \quad j = 1, 2, \dots, N \quad (2.78)$$

where:

- N is the number of data points or observations
- $\lambda_{i,j}$ is the value of invariant i of the general data point j
- $\bar{\lambda}_i$ is the mean of invariant λ_i over all data points $j=1, 2, \dots, N$.
- σ_i is the standard deviation of the value of invariant λ_i
- $\lambda_{i,j}^Z$ is the normalized value of invariant i of the general data point j

Again, through the application of z-score normalization to invariants layer a significant reduction of the network's final loss function was achieved.

2.3.3 Network's hyperparameters and architecture

The neural network was trained using the Nadam (Nesterov-accelerated Adaptive Moment Estimation) optimizer. Nadam optimizer falls within the class of gradient descent optimization algorithms. The principles of mini-batch Stochastic Gradient Descent methods have already been explained in Chapter 1 and are summarized by (1.43) formula. One problem with Stochastic Gradient Descent Methods (SGD) is that they have trouble navigating ravines, i.e. areas where the loss function's surface curves much more steeply in one dimension than in another, which are common around local optima. In these scenarios, SGD oscillates across the slopes of the ravine while only making hesitant progress along the bottom towards the local minima [33]. Momentum is a method that helps accelerate SGD in the relevant direction and dampens oscillations. It does this by adding a fraction γ of the update vector of the past time step to the current update vector:

$$\begin{aligned}\Delta W^k &= \gamma \Delta W^{k-1} + \eta \nabla L_m(W^k - 1) \\ W^k &= W^{k-1} - \Delta W^k\end{aligned}\tag{2.79}$$

where the meaning of the terms in (2.79) is the same as in (1.43). The momentum term γ is usually set to a value near the $[0,1]$ range. When $\gamma=0$ the standard mini-batch SGD expression (1.43) is recovered. Essentially, we can think of using momentum as pushing a ball -the model's parameters - down a hill - the loss function curve. The ball accumulates momentum as it rolls downhill, becoming faster and faster on the way (until it reaches its terminal velocity if there is air resistance, i.e. $\gamma < 1$). The same thing happens to the model parameter updates: The momentum term increases the parameter change for dimensions whose gradients point in the same directions and reduces updates for dimensions whose gradients change directions. As a result, faster convergence and reduced oscillation are achieved. However, a ball that rolls down a hill, blindly following the slope, is highly unsatisfactory. It would be much better to have a smarter ball that has a notion of where it is going so that it knows to slow down before the hill slopes up again. Nesterov accelerated gradient (NAG) is a technique to give the momentum term this kind of prescience. We know that we will use our momentum term $\gamma \Delta W^{k-1}$ to move parameters W . Computing $W^k - \gamma \Delta W^{k-1}$ thus gives us an approximation of the next position of the parameters (the gradient is missing for the full update), a rough idea where the parameters are going to be. We can now effectively look ahead by calculating the gradient not with respect to our current parameters W but with respect to the approximate future position of our parameters:

$$\begin{aligned}\Delta W^k &= \gamma \Delta W^{k-1} + \eta \nabla L_m(W^{k-1} - \gamma \Delta W^{k-1}) \\ W^k &= W^{k-1} - \Delta W^k\end{aligned}\tag{2.80}$$

Nadam (Nesterov-accelerated Adaptive Moment Estimation) is a combination of Adam and NAG methods. Adam is an adaptive learning rate method, that computes individual adaptive learning rates for different parameters [34]. Indeed, SGD maintains a single learning rate (termed η) for all weight updates and the learning rate does not change during training. A learning rate is maintained for each network weight (parameter) and separately adapted as learning unfolds. The authors describe Adam as combining the advantages of two other extensions of stochastic gradient descent. Specifically:

- Adaptive Gradient Algorithm (AdaGrad) that maintains a per-parameter learning rate that improves performance on problems with sparse gradients (e.g. natural language and computer vision problems).
- Root Mean Square Propagation (RMSProp) that also maintains per-parameter learning rates that are adapted based on the average of recent magnitudes of the gradients for the weight (e.g. how quickly it is changing). This means the algorithm does well on online and non-stationary problems (e.g. noisy)

Adam realizes the benefits of both AdaGrad and RMSProp. Instead of adapting the parameter learning rates based on the average first moment (the mean) as in RMSProp, Adam also makes use of the average of the second moments of the gradients (the uncentered variance) [34].

The choice of the optimizer was made after testing different possibilities: SGD, Adam, Adadelta.... from which Nadam proved the method with better results in terms of final term loss.

In order to measure the neural network predictive performance, a loss function must be chosen. As in [9], the Root Mean Squared Error (RMSE) was chosen:

$$\text{RMSE} = \sqrt{\frac{1}{N_{data}} \sum_{m=1}^{N_{data}} \sum_{i=1}^3 \sum_{j=1}^i (b_{ij,m}^{NN} - b_{ij,m}^{DNS})^2} \quad (2.81)$$

where N_{data} is the total number of observations, $b_{ij,m}^{NN}$ is the nondimensional anisotropy tensor predicted by the neural network from inputs of observation m and $b_{ij,m}^{DNS}$ is the DNS anisotropy stress tensor corresponding to data point m . In order to time the training, early-stopping was used, in which a portion of the training data are held out as validation data and the validation error is monitored during training. The training process terminates once the validation error begins to increase.

For the neural network, there were four main parameters to tune: the number of hidden layers, the number of nodes per layer, the batch size and the activation function. Indeed, contrarily to Ling's work, a different activation function has been chosen for different layers. This choice allowed to

achieve a reduction of the final error compared to the use of only one activation function for all layers (like ReLu). It is important to notice that, when using adaptive learning rate algorithms such as Nadam, only initial values of learning rate and momentum must be chosen, hence they do not represents actual parameters to tune. As for them, the default Keras value were used ($\eta = 0.001$ and $\gamma = 0.9$) as suggested in the documentation [32].

As far as the hyperparameters tuning of a neural network is concerned, two methods are commonly followed: either one starts from a configuration already implemented for a similar problem and proceeds by trial and error or one can use Bayesian optimization, in the parameter space is sampled and at each sample, a neural network with those hyper-parameters is constructed and trained [18]. The network performance is then evaluated on a validation data set separate from both the training data and the test data. However, the latter method is rather computationally expensive and therefore the first solution was adopted. In particular, an architecture similar to the one of TBNN in [9] was chosen and then changed by trial and error. After trying different configurations, the following network structure was defined:

TABLE III: NEURAL NETWORK'S ARCHITECTURE

Layer	Type	Nodes	Activation Funtion
Invariants λ_i	Input 1	5	Linear
Tensor Basis $\mathbf{T}^{(n)}$	Input 2	10	Linear
Hydden 1	Dense	60	Linear
Hydden 2	Dense	60	Softsign
Hydden 3	Dense	60	ReLu
Hydden 4	Dense	60	ReLu
Hydden 5	Dense	60	ReLu
Hydden 6	Dense	60	ReLu
Hydden 7	Dense	60	Linear
Hydden 8	Dense	60	Linear
Coefficients $g^{(n)}$	Dense	10	Linear
\mathbf{b} components	Output	6	Linear

The activation functions mentioned in Table III are defined by the following expressions:

- Linear activation function $\Phi_L(x) = x$
- ReLu activation function $\Phi_R(x) = \max(0, x)$
- Softsign activation function $\Phi_S(x) = \frac{x}{1 + |x|}$

where each function operates element wise on $(\mathbf{W}^k \mathbf{x}^{k-1} + \mathbf{b}^k)$ of generic layer k . The distribution of activation functions has been chosen by fixing the same number of hidden layers of Ling's TBNN [9]- namely 8 - and through trial and error. The chosen configuration is the one that allowed to achieve the lowest final RMSE. The general principal driving the trial and error procedure was that the function $g^{(n)}(\lambda_i)$ had to be highly non-linear to be able to fit a wide variety of different flows. This justify the use of nonlinear activation functions Softsign and ReLu.

The other crucial characteristic of the model are listed and summed up in the following Table IV

TABLE IV: MODEL'S CHARACTERISTICS

Characteristic	Choice
Optimizer	Nadam
η_0 Nadam	0.001
γ_0 Nadam	0.9
Batch Size	256
Loss	RMSE
Early stopping	Yes
Shuffling	Yes
Biases Initializer	Zeros
Weight Initializer	Glorot Uniform
Train-Validation split factor	0.8

where:

- *Shuffling* refers to the practice of shuffling validation data after each epoch of the training phase. This technique avoids the network to learn a pattern linked to the order in which the data are presented in batches.
- *Zeros biases initialization* means that all layers' biases are initialized to 0 before training [32].

- *Glorot Uniform* is a standard weight initialization; draws samples from a uniform distribution within $[-\text{limit}, \text{limit}]$ where limit is $\sqrt{6/(\text{in} + \text{out})}$ where *in* is the number of input units in the weight tensor and *out* is the number of output units in the weight tensor [32].

2.3.4 Training phase and a priori result

As in most data driven turbulence modelling approaches, the use of machine learning can be divided into two phases:

1. The neural network or the other machine learning tool is trained offline- namely separately from the CFD code - on a certain flows dataset. The result of the training phase are usually called *a priori results* since the network has not still been used in conjunction with a CFD code to improve its performances.
2. The network is used in some way to improve the CFD solver performances. The results of the CFD solver in conjunction with the machine learning technique is usually referred to as a posteriori results.

In this section, the result of the training phase will be analyzed, namely the a priori result of the neural network in predicting anisotropy stress tensor components from the corresponding inputs.

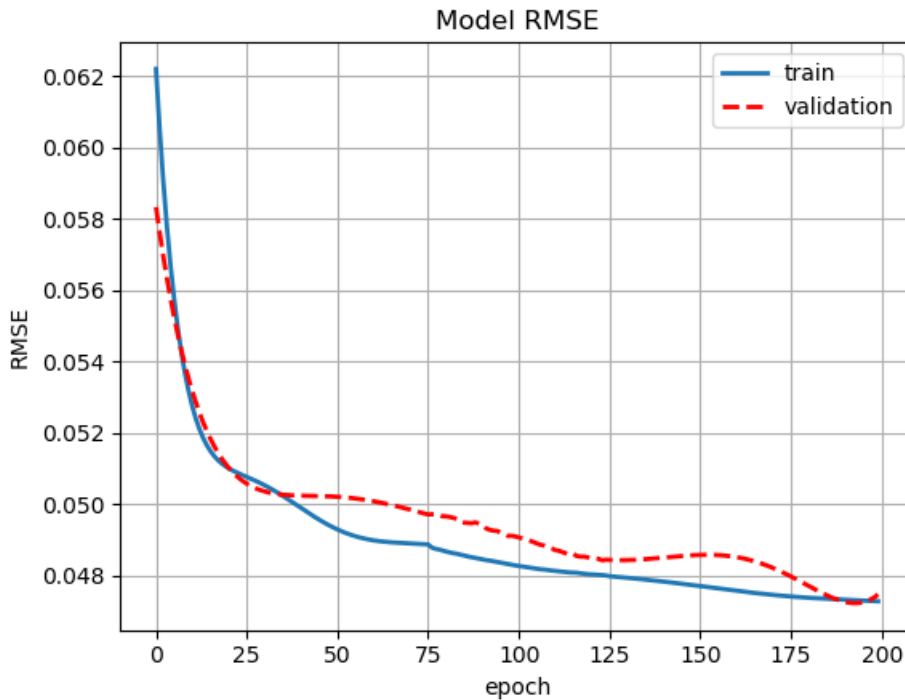


Figure 28: Train and validation RMSE

In the above Fig.(28) the validation and training losses are shown. As one can observe, the train and validation RMSE are close during the training. This represents a sign that overfitting did not occur. The final RMSE is around 0.0475 both for validation and training dataset. The final RMSE is almost half the best Ling's model's a priori results [9], yet this result should be expected since the model was trained with the DNS inputs - therefore way more accurate than the RANS ones. In order to visualize the result, the model was used to predict the anisotropy stress tensor for one flow of the dataset - the Square Duct Flow. The outcome is showed in the following Fig.29.

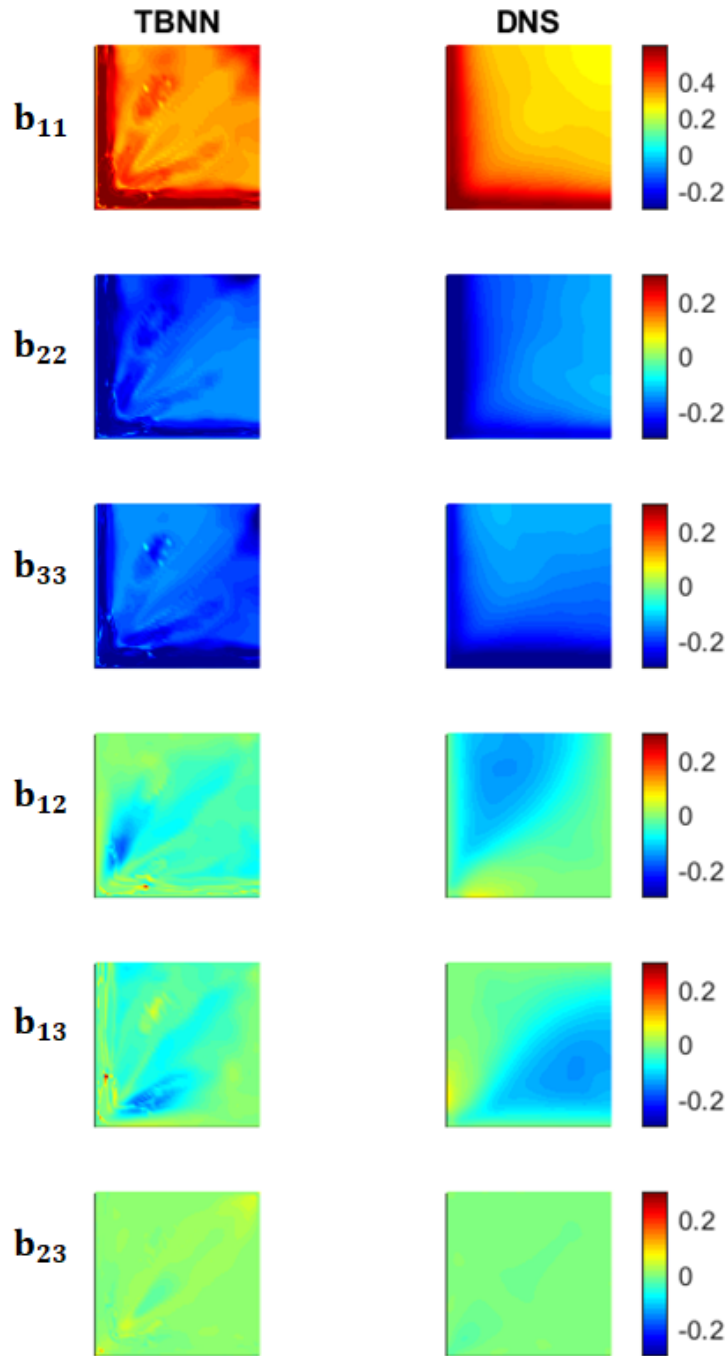


Figure 29: A priori Predictions of Reynolds stress anisotropy tensor on the Duct Flow case

Only the lower left quadrant of the duct is shown, and the streamwise flow direction is out of the page. The first column show the predictions of the TBNN and the true DNS anisotropy values are shown in the right column for comparison.

In comparison, the baseline LEVM completely fails to predict the anisotropy values. It predicts zero anisotropy for b_{11} , b_{22} , and b_{12} . This is due to the fact that the LEVM does not predict any secondary flows in the duct, so the mean velocity in the x_1 and x_2 directions - the one sin the transverse plane shown above-is zero, causing S_{11} , and S_{22} to be zero. Since the flow is periodic in the x_3 direction, S_{33} is also zero. As a result, b components are all zeros as shown below in Fig.(30).

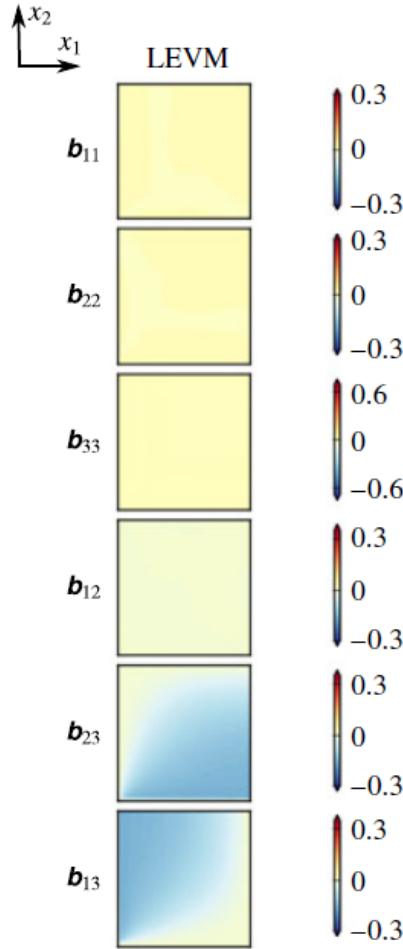


Figure 30: Baseline LEVM Predictions of Reynolds stress anisotropy tensor on the Duct Flow case

On the contrary, the TBNN is not only able to predict the value of the anisotropy stress tensor components, but also to pick its trends on the transverse section of the square duct.

2.3.5 Embedment of the neural network into the CFD solver

A scheme of the approach proposed in this work has already been shown in Fig.(4). In the following figure Fig.(31), the steps involved in the embedment of the neural network into the CFD solver (b) are shown in comparison to the standard LEVM approach (a). All the passages have already been explained in detail above. The steps differing from the standard LEVM model have been highlighted in red. Basically, insted of directly applying (1.27) to the inputs listed on top of Fig.(31a), deriving from previous computations of the solver at iteration n, a different set of inputs - top of Fig.(31a)- are nondimensionalized, normalized and fed to the TBNN. The output is the anisotropy stress tensor predicted by the network.

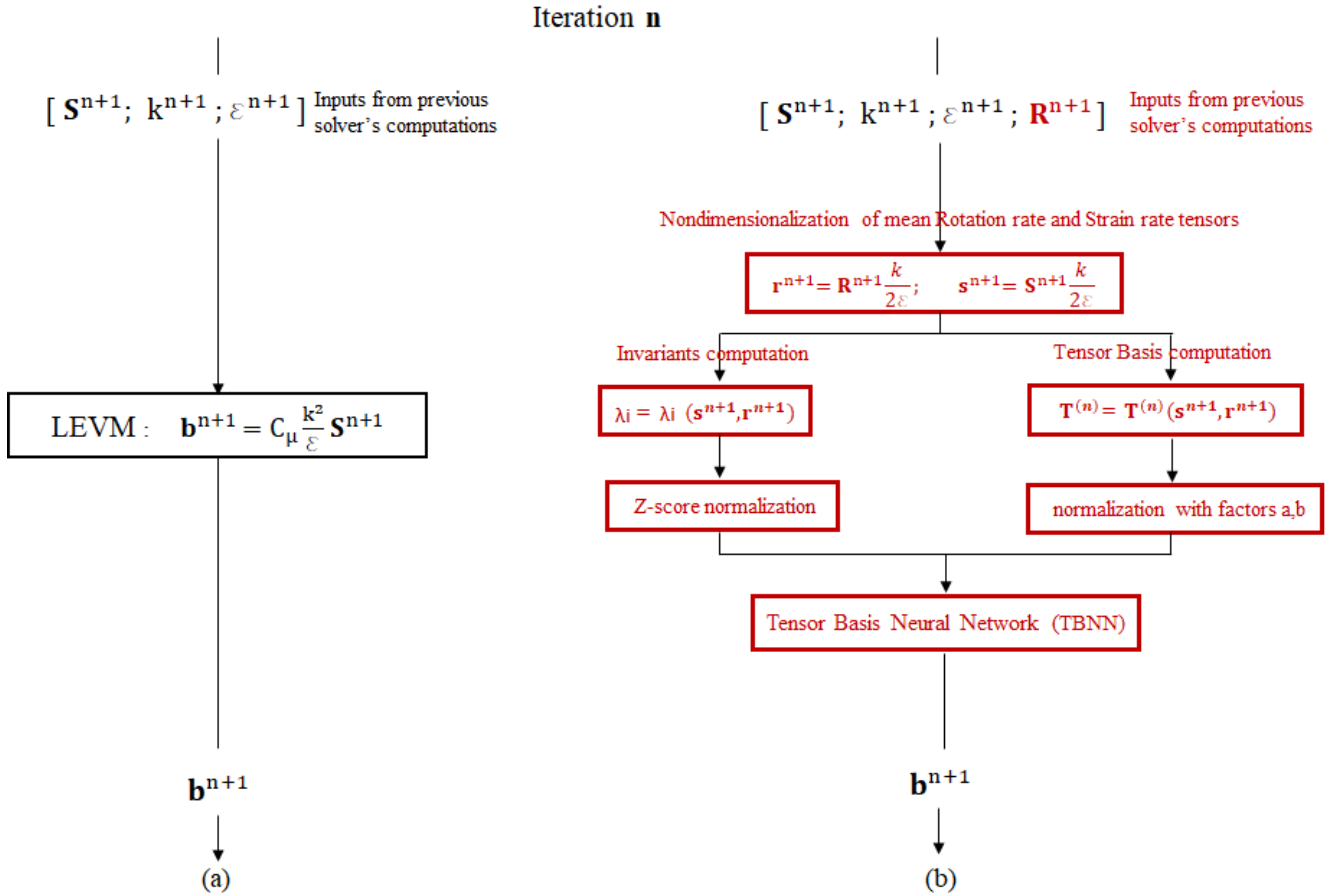


Figure 31: Embedment of the neural network into the CFD solver

It is important to stress again that the use of the neural network as described in Fig.(31) differs from the standard application of machine learning methods in the data driven turbulence modelling approaches. Indeed, the machine learning method is usually used as a post-processing technique to correct the RANS anisotropy stress tensor; it receives in input the quantities of interest of the converged standard

RANS model and predicts an anisotropy stress tensor field that is imposed as fixed in the further iteration of the RANS model. Here, instead, the machine learning is used to replace the LEVM function correlating \mathbf{b} to velocity gradients and turbulent quantities, and therefore it must be called at each iteration of the solver. As for this last practical aspect, one problem that had to be faced was that the model was trained using Python- in particular Keras library - whereas the CFD solver was coded in Matlab. One possibility consisted in computing the network's inputs in the Matlab solver and pass to the Python code at each iteration. However, calling the Python script from Matlab and reloading the Keras model proved extremely time expensive, compared to the solver's iteration time. As a solution, the weights and biases of the model were extracted from the Keras network and the matrices and vectors were imported in matlab. After that, the same model architecture was coded in matlab - it simply consists of matrices multiplications. In this way, the LEVM iteration time and the iteration time with the NN model proved absolutely comparable.

Chapter 3

RESULTS AND CONCLUSIONS

3.1 Application to the turbulent channel flow case

The Tensor Basis Neural Network' performance was analyzed on the same case on which the CFD RANS solver was validated- namely the fully developed turbulent channel flow at $Re_\tau = 544$ - due to the availability of reference DNS data for comparison [6]. Moreover, the channel flow was chosen because, in this case, the performance of the LEVM in predicting the Reynolds stress tensor's components yields good result only for the shear stress $\langle uv \rangle$, as it will be later shown. This is due to the intrinsic limits of the relation (1.27), in which the anisotropy stress tensor components are assumed to be in a linear relation with the mean strain rate tensor. Yet, in the fully developed region of the channel flow, such a tensor is reduced to:

$$\langle \mathbf{S} \rangle = \begin{bmatrix} 0 & \frac{1}{2} \frac{\partial \langle u \rangle}{\partial y} & 0 \\ \frac{1}{2} \frac{\partial \langle u \rangle}{\partial y} & 0 & 0 \\ 0 & 0 & 0 \end{bmatrix} \quad (3.1)$$

since $\langle v \rangle = 0$, $\langle w \rangle = 0$ and the variation of the variables occurs only on the direction orthogonal to the walls y , namely $\frac{\partial}{\partial x} = 0$ and $\frac{\partial}{\partial z} = 0$.

Now, since according to the LEVM:

$$\mathbf{a}^{LEVM} = C_\mu \frac{k^2}{\varepsilon} \langle \mathbf{S} \rangle$$

with \mathbf{a}^{LEVM} being the anisotropy stress tensor predicted with the LEVM, it is clear that the only non-zero component of such a tensor will be a_{12} and that therefore tensor \mathbf{a}^{LEVM} will have the following

form:

$$\mathbf{a}^{LEVM} = \begin{bmatrix} 0 & a_{12} & 0 \\ a_{12} & 0 & 0 \\ 0 & 0 & 0 \end{bmatrix} \quad (3.2)$$

As a consequence, by recalling (1.13), the Reynolds stress tensor predicted by the LEVM will be:

$$u_i u_j^{LEVM} = \begin{bmatrix} \frac{2}{3}k & a_{12} & 0 \\ a_{12} & \frac{2}{3}k & 0 \\ 0 & 0 & \frac{2}{3}k \end{bmatrix} \quad (3.3)$$

Hence, when applying a RANS model using the LEVM to the turbulent channel flow case, all the diagonal components of the Reynolds stress tensor will be predicted with the same value. In the following Fig.(32) the Reynolds stresses' profiles obtained with the CFD RANS solver run with the standard LEVM are shown.

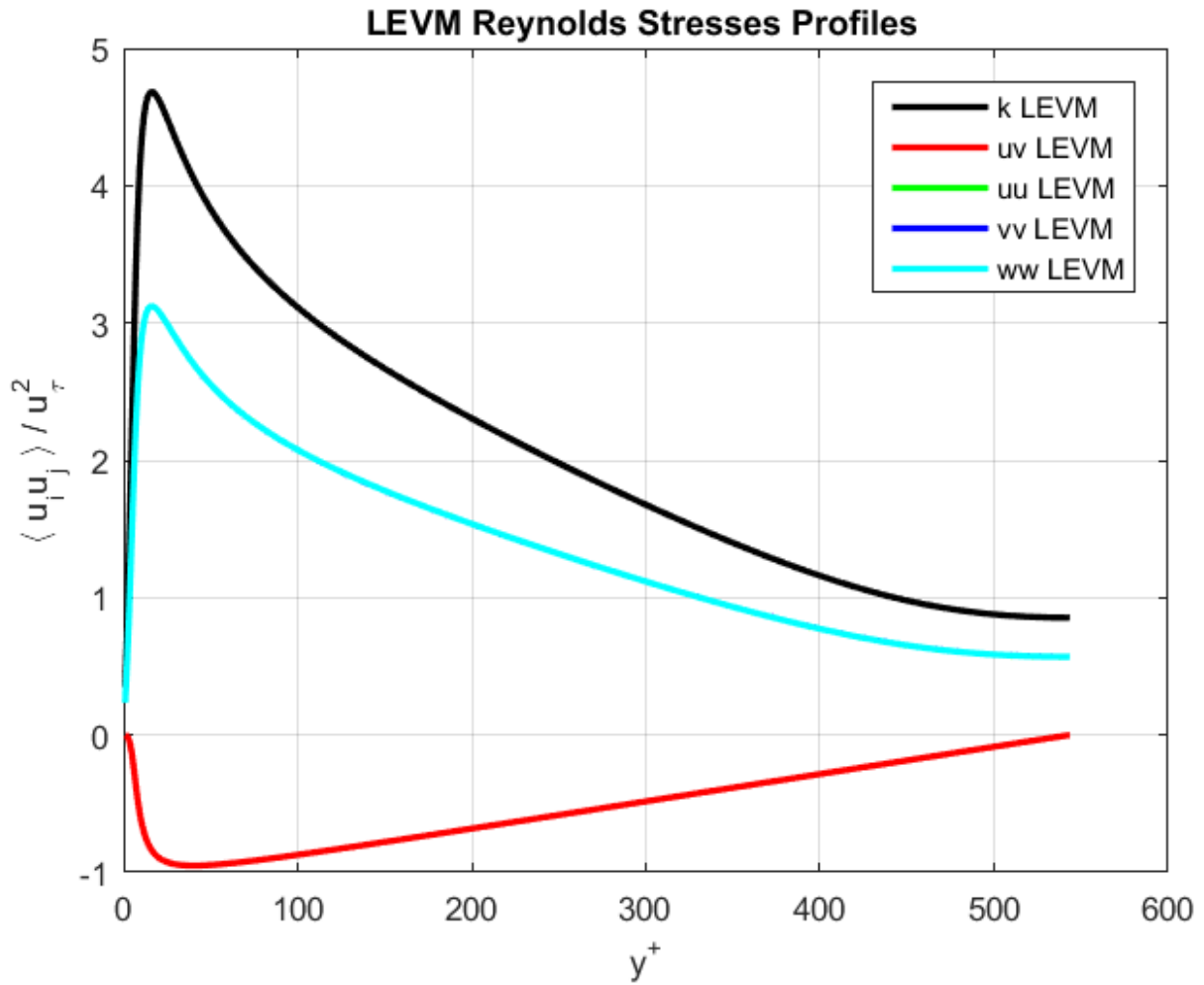


Figure 32: Turbulent Channel Flow: Reynolds stresses profiles with LEVM

One can observe that, as expected, the profiles of the normal Reynolds stresses are superposed. This outcome is the result of the linearity of LEVM relation (3.3). However, as shown in the following figure, the actual normal Reynolds stresses profiles [6] are significantly different in the channel flow case:

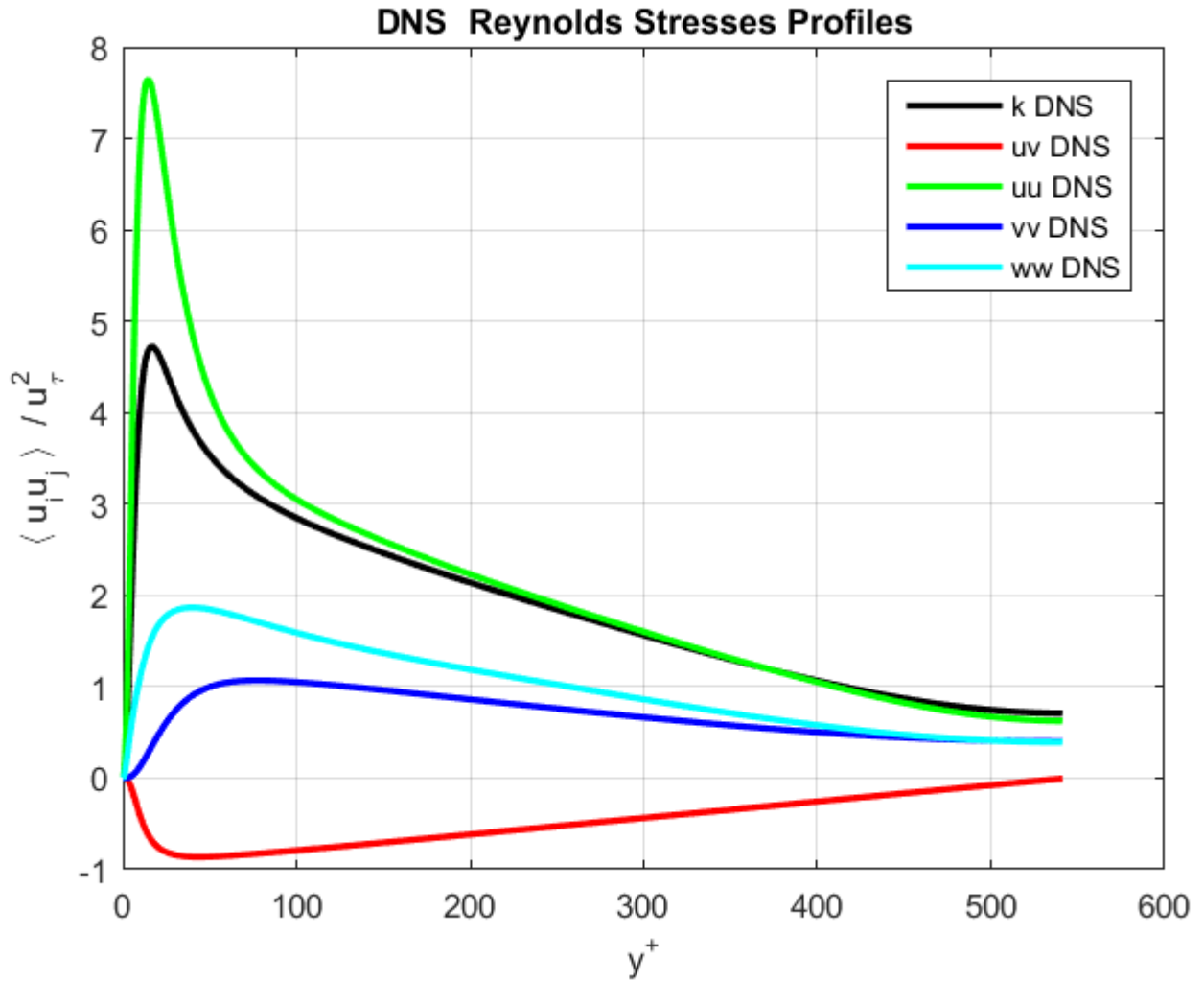


Figure 33: Turbulent Channel Flow: DNS Reynolds stresses profiles

By comparing Fig.(32) with Fig.(33) it emerges clearly that, apart from the shear stress $\langle uv \rangle$, the Reynolds stresses prediction resulting from the LEVM is unsatisfactory for all the other components of the Reynolds stress tensor. Interestingly, an analogue result would be obtained with all fully developed flow cases in which the variation of the quantities occurs only in one direction - such as for example the Couette Flow. In most of this cases, however, the normal stress profiles are not the same, and therefore the prediction of LEVM proves flawed.

It is now interesting to compare the predictive performances of LEVM and TBNN in terms of Reynolds stresses. In the following figure, the DNS and LEVM Reynolds stresses profiles are compared with

the *first* prediction of the TBNN, namely on the prediction of the network based on the inputs of the converged standard RANS.

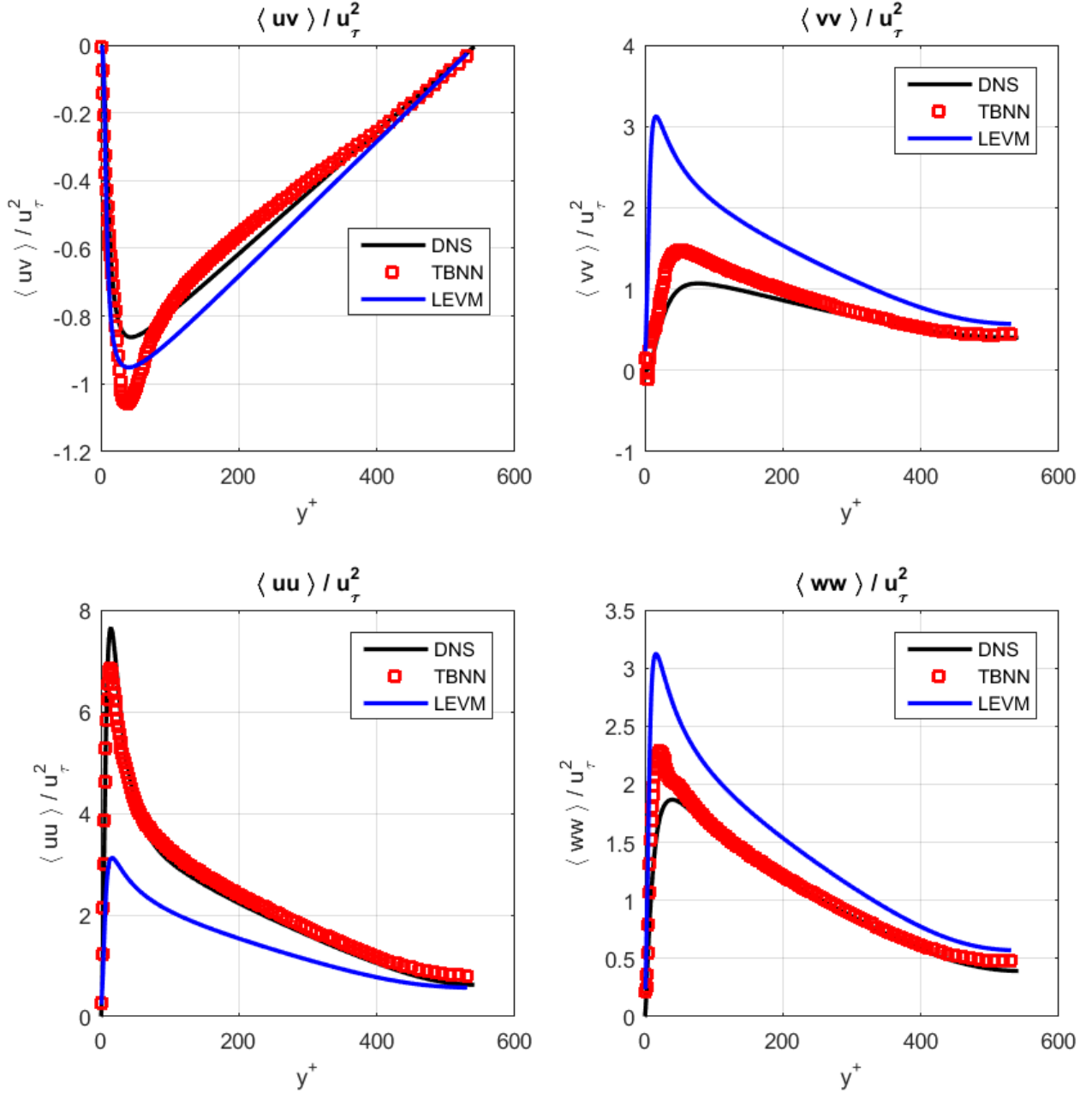


Figure 34: Turbulent Channel Flow: DNS, LEVM and TBNN Reynolds Stresses profiles' comparison

As one can easily observe in Fig.(34) the first prediction of the TBNN significantly outperforms the LEVM in all zones of the channel height, apart from the shear stress $\langle uv \rangle$ for a certain y^+ range. In particular, as one can observe in Fig.(35), the Reynolds normal stresses' profiles differ from each other and are much more accurate than the LEVM ones. This is due to the fact that the General Eddy Vis-

cosity model (1.29) involves not only the mean strain rate tensor $\langle \mathbf{S} \rangle = \mathbf{T}^{(1)}$ but a basis of 10 symmetric and invariant tensors derived from second and third order products of $\langle \mathbf{S} \rangle$ and $\langle \mathbf{R} \rangle$. This formulation of the Reynolds stresses model incorporates non-linear terms and therefore, even when the $\langle \mathbf{S} \rangle$ has only one non-zero component, the contribution of the other tensors allows to predict distinct profiles for the Reynolds normal stresses.

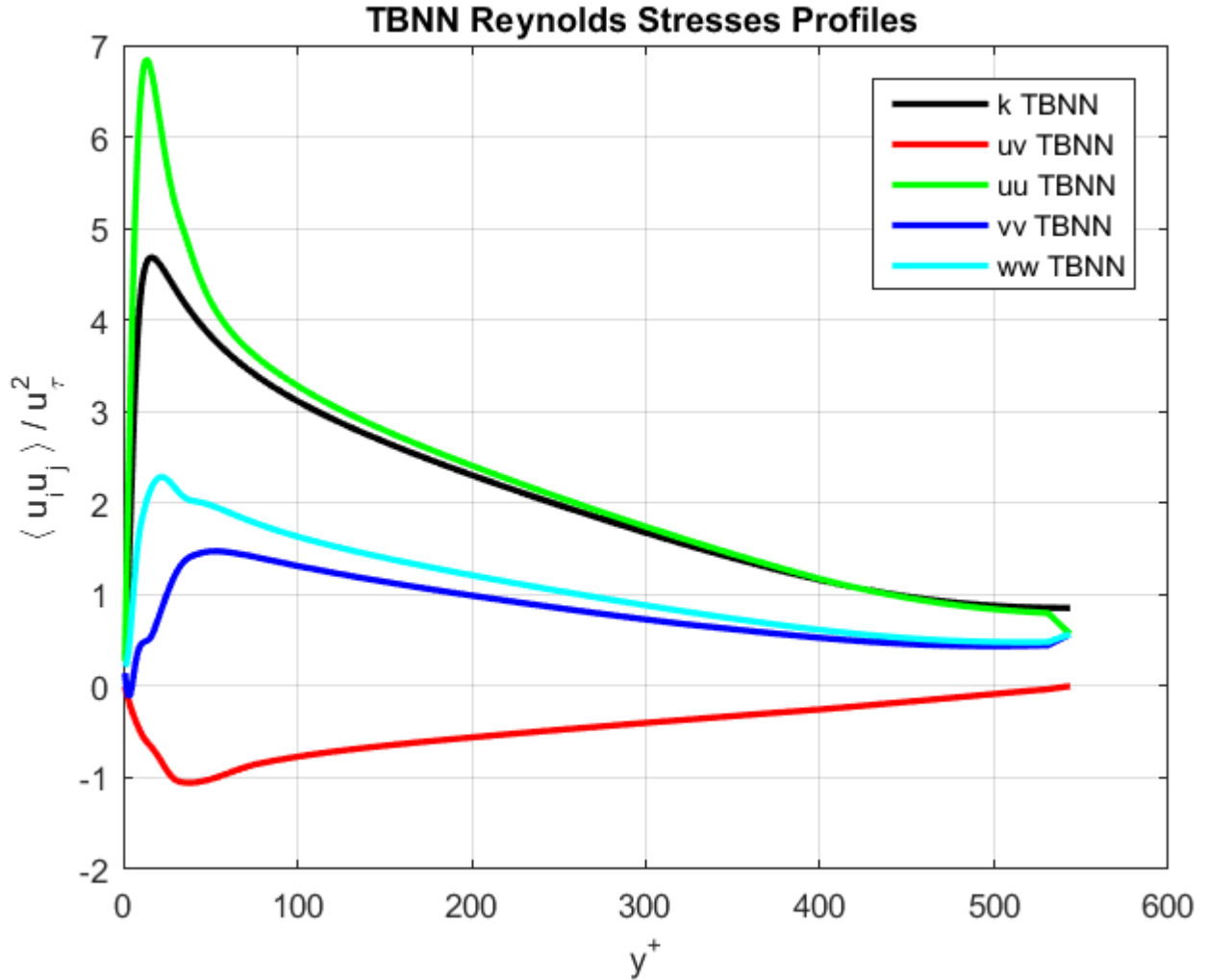


Figure 35: Turbulent Channel Flow: TBNN Reynolds stresses profiles

It is yet important to stress that the General Eddy Viscosity formulation (1.29) assuming a universal functional mapping between the anisotropy stress tensor \mathbf{a} and $\langle \mathbf{S} \rangle$ and $\langle \mathbf{R} \rangle$ tensors represents a simplified model. Indeed, the turbulence is also influenced by pressure gradients. On the other hand, the general form (1.29) assumes equilibrium turbulence, i.e., the turbulence production balances dissipation everywhere in the field. With such an assumption, the Reynolds stress at location \mathbf{x} only depends on the local gradients of mean velocity at the same location $\nabla \langle \mathbf{U} \rangle(\mathbf{x})$. However, the convection and diffusion of turbulence exist in many real applications, indicating strong non-equilibrium effects and

making this single-point-based turbulent constitutive law invalid. Hence, a certain discrepancy between the TBNN and the DNS data is justified by the limits of the assumptions leading to (1.29).

It is now interesting to observe how the different tensors $\mathbf{T}^{(n)}$ contribute to the final nondimensional anisotropy stress tensor \mathbf{a} . It is crucial to recall that, if $g^{(1)} = -C_\mu = -0.09$ and $g^{(n)} = 0$ for $n > 1$, the General Eddy Viscosity model reduces itself to the LEVM. Hence, it is also interesting to observe the coefficient $g^{(1)}$ predicted by the TBNN and compare it to the value that results in the LEVM. This is shown in the following Fig.(36):

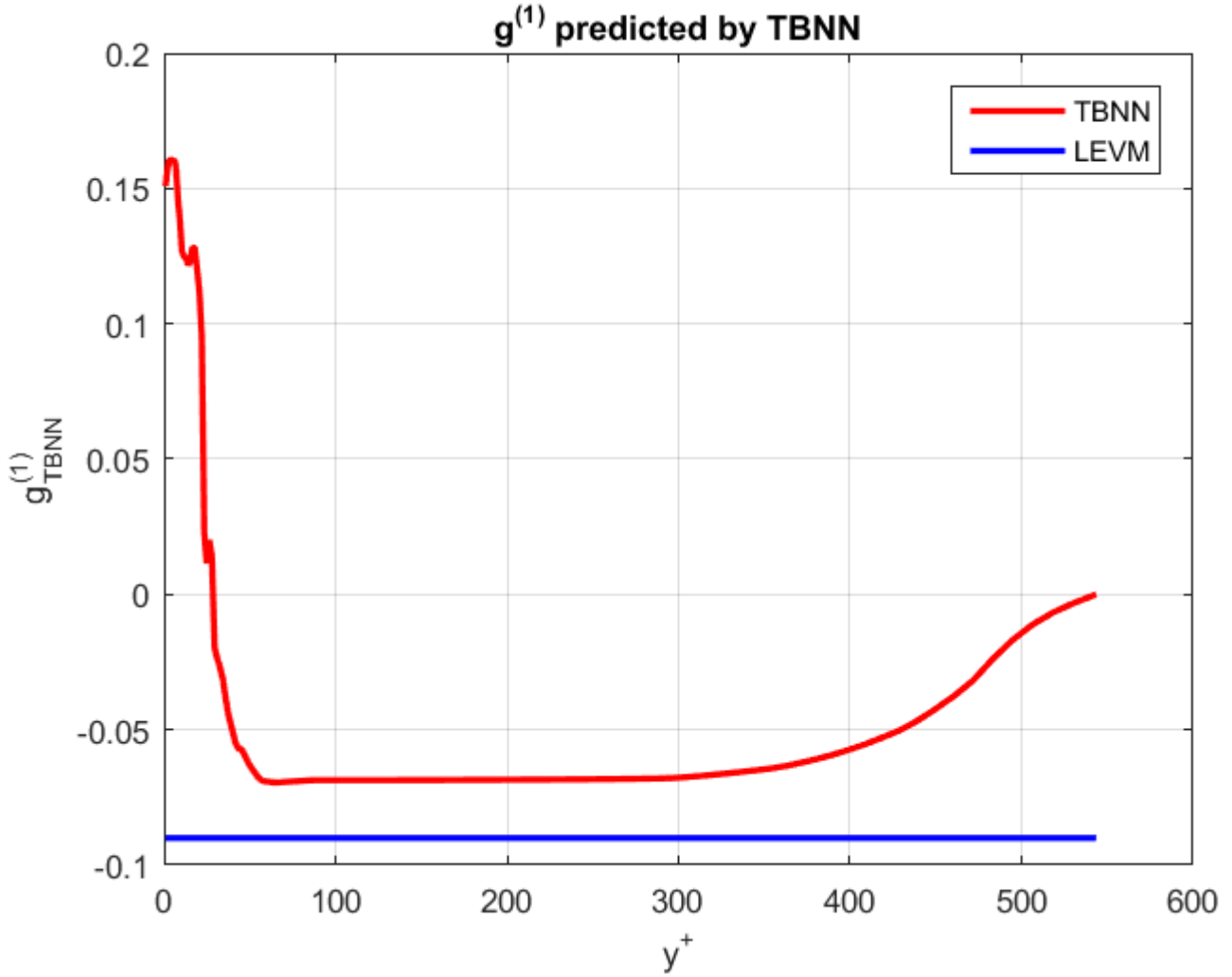


Figure 36: Coefficient $g^{(1)}$ predicted by TBNN at first solver iteration

As it can be observed, the coefficient $g^{(1)}$ predicted by the TBNN has a value close to the LEVM one, yet not on the whole channel height. Indeed, the two values are particularly close in the log-law region - approximately for $y^+ > 30$ - where $g_{TBNN}^{(1)}$ holds an almost constant value. Instead, near the wall and near the channel's axis, the coefficient deviates significantly from the value $-C_\mu$. This result is perfectly reasonable: the value of constant C_μ for the LEVM has been calibrated to match

experimental results obtained in the log-law region of turbulent channel flows, and the LEVM proves correct in this flow region; as a consequence, one can expect the TBNN to look for a model similar to the LEVM. On the contrary, LEVM fails in the near-wall region and this is the reason why a low-Re $k - \varepsilon$ model with damping functions was adopted. The damping function f_μ of Abe-Kondoh-Nagano model depends, among other quantities, from the wall distance y^+ , which is not an input in the General Eddy Viscosity model (1.29). It is therefore clear that, in the near wall-region, the neural network has to find a model fairly distant from the LEVM one.

Lastly, it is interesting to analyze the contribution of the other basis tensors $\mathbf{T}^{(n)}$ for $n > 1$. In the following figure, the nondimensional coefficients $\tilde{g}^{(n)}$ explained in Chapter 2 are shown:

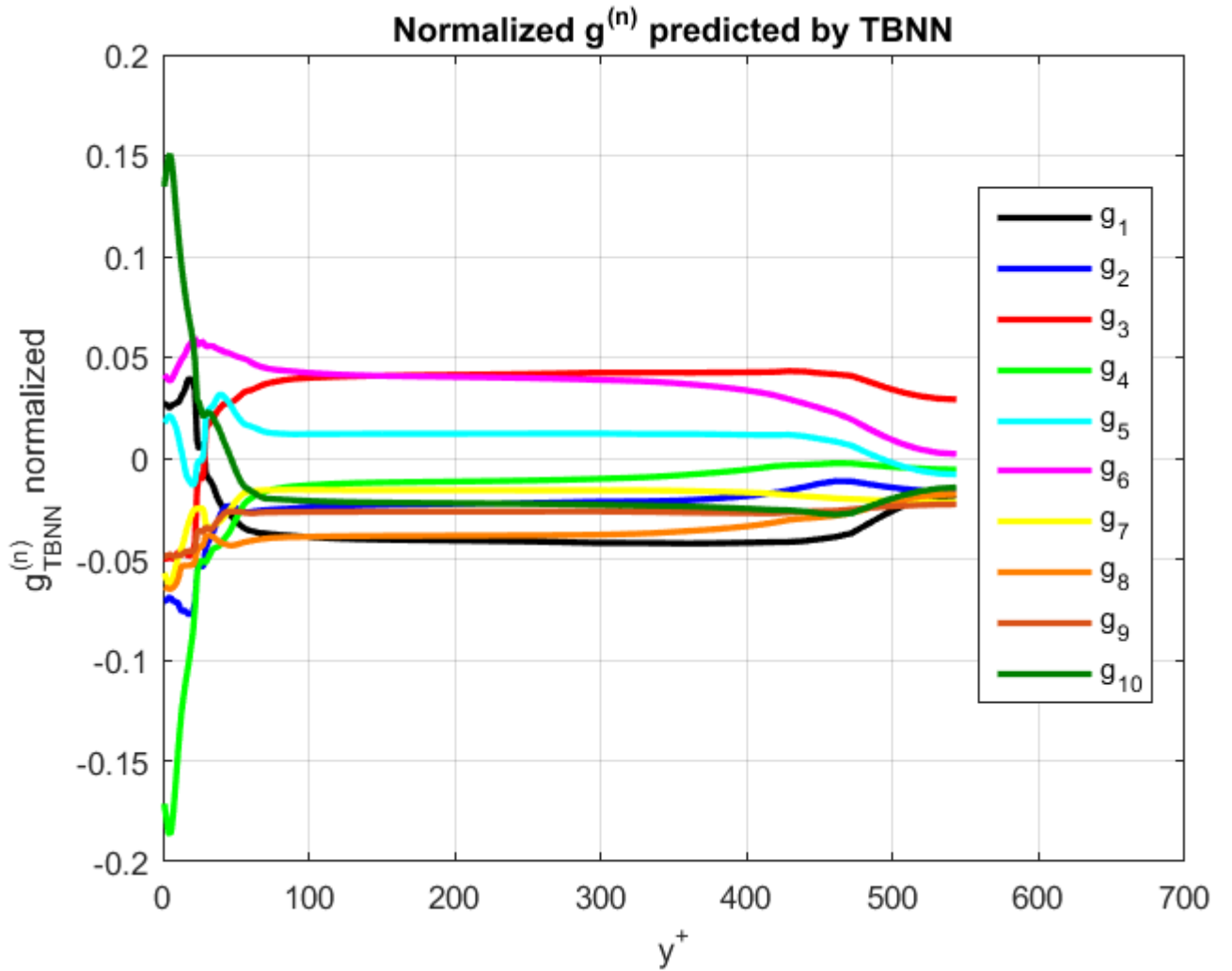


Figure 37: Coefficients $g^{(n)}$ predicted by TBNN at first solver iteration

It is interesting to observe that:

- None of the coefficient is identically null, and therefore all the basis tensors contribute to \mathbf{b} .

Since the LEVM is outperformed by the TBNN in the Reynolds stresses prediction, it is fair to

conclude that the linear relation of LEVM is limited and that including higher order non-linear tensors into the prediction of \mathbf{b} can significantly improves the CFD RANS solver performance. This is true, even though the Reynolds stress anisotropy is not the only source of uncertainty in the RANS equations, which also rely on approximate transport equations for k and ε .

- All the coefficients hold an approximately constant value in the log-law region, whereas near the wall their profiles are much more noisy. This may be an indication of the fact that, in the near wall region, an important variable is the wall distance y^+ , and that it should be included in the General Eddy Viscosity model as an additional input. Indeed, for $y^+ < 30'$ the TBNN has to look for a less smooth function in compensation to accomodate the prediction to the DNS values.
- Near the channel axis $y = \delta$, all coefficients $g^{(n)} \rightarrow 0$. This can be explained by the fact that:

$$\left(\frac{\partial \langle u \rangle}{\partial y} \right)_{y=\delta} = 0 \quad (3.4)$$

and therefore, since all the velocity gradients are null at the channel axis, then $\mathbf{T}^{(n)} = \mathbf{0}$ for $n = 1, ..10$. Hence, the prediction of \mathbf{b} would be the same for every vector of coefficients $g^{(n)}$.

So far, however, only the *first prediction* of the TBNN has been analyzed. In order to test the proposed approach, it is necessary to run the RANS solver with the use of the TBNN at every iteration. In particular, it is interesting to observe whether the improved predictions of Reynolds stresses can have a significant impact on the real quantity of interest, namely the mean velocity $\langle u \rangle$. Notwithstanding, by analyzing the TBNN Reynolds stresses first prediction it emerges clearly that the use of a General Eddy Viscosity model tuned through machine learning techniques can provide a significantly more complete model for the Reynolds stresses than the LEVM.

3.2 Effect on the mean velocity

Given the significantly improved Reynolds stress anisotropy predictions of the TBNN, it was of interest to determine whether these improved anisotropy values would translate to improved mean velocity predictions. To do so, the CFD RANS solver should be run on the same flow case using the TBNN integration scheme described in Fig.(31). In order to speed convergence, the TBNN scheme should be run starting from a converged RANS simulation as initial conditions.

Notably, the Reynolds stress anisotropy is not the only source of uncertainty in the RANS equations, which also rely on approximate transport equations for k and ε . Therefore, the true DNS anisotropy

stress tensors were also implemented in the RANS solver as fixed fields as a point of comparison. This DNS anisotropy model shows the flow predictions that would be achieved by using the correct normalized anisotropy tensor \mathbf{b} , given the other RANS model assumptions. It therefore represents the upper performance limit of an improved Reynolds stress anisotropy model. In this case, only the a_{12} component of the anisotropy stress tensor from the DNS data was enforced as a fixed field in the RANS solver. Indeed, the component a_{11} has a negligible effect on $\langle u \rangle$ since in the corresponding momentum equation the $\frac{\partial}{\partial x}$ derivative cancels its effect for the fully developed flow. The other component a_{22} has only effect on the $\langle v \rangle$ equation, and therefore its effect is negligible since $\langle v \rangle = 0$ in the fully developed region of turbulent channel flow. The result of enforcing the a_{12} anisotropy stress tensor field on the RANS solver is shown in the following Fig.(38):

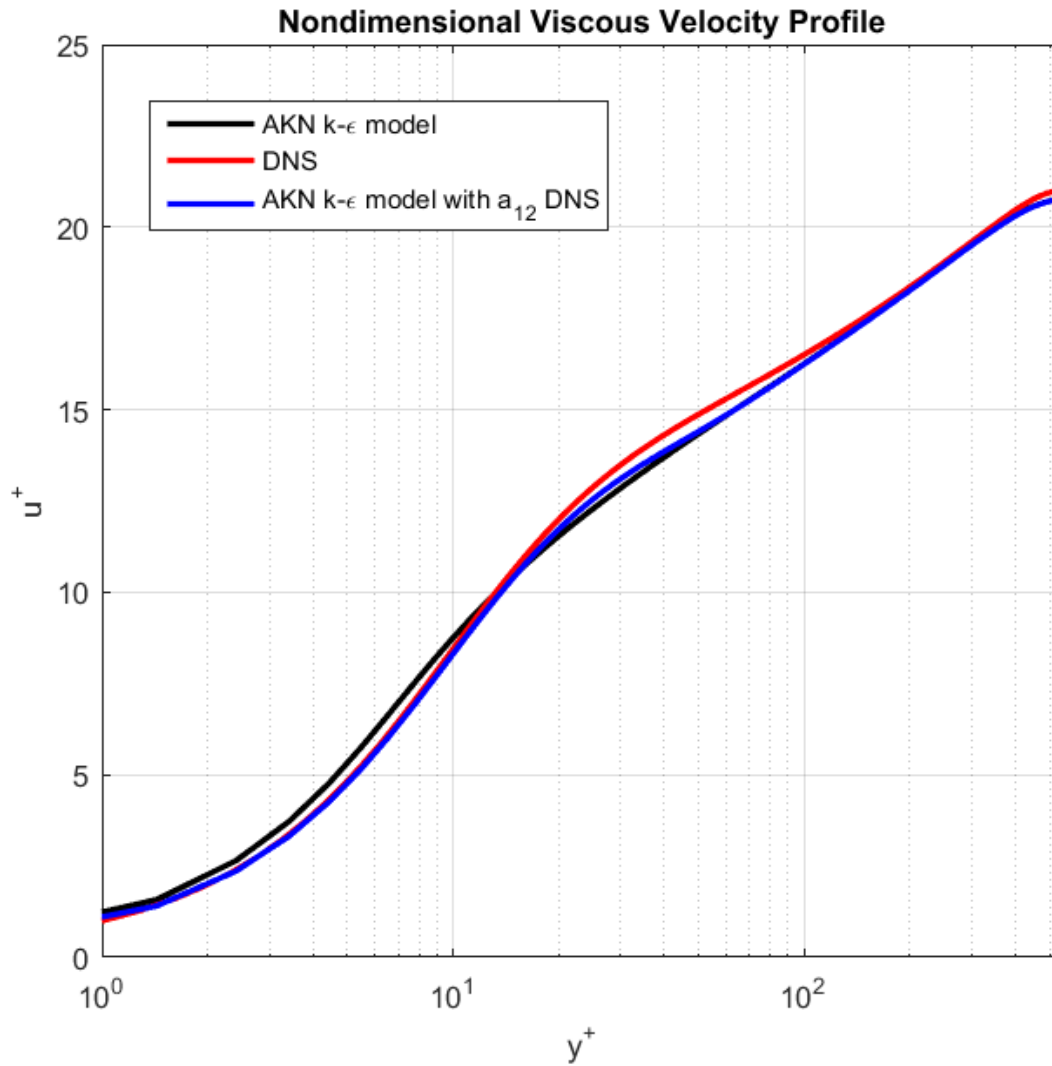


Figure 38: Mean velocity field resulting from enforcing true DNS anisotropy tensor

As one can observe, enforcing the true anisotropy stresses field leads only to a slight improvement

of mean velocity prediction. The discrepancy between the DNS data and the ones obtained imposing the DNS stresses is due to the other approximations of RANS $k - \varepsilon$ model, in particular regarding the model transport equations for k and ε .

Now, by running the CFD RANS solver on the turbulent channel flow case using the TBNN integration scheme described in Fig.(31), it has been obtained:

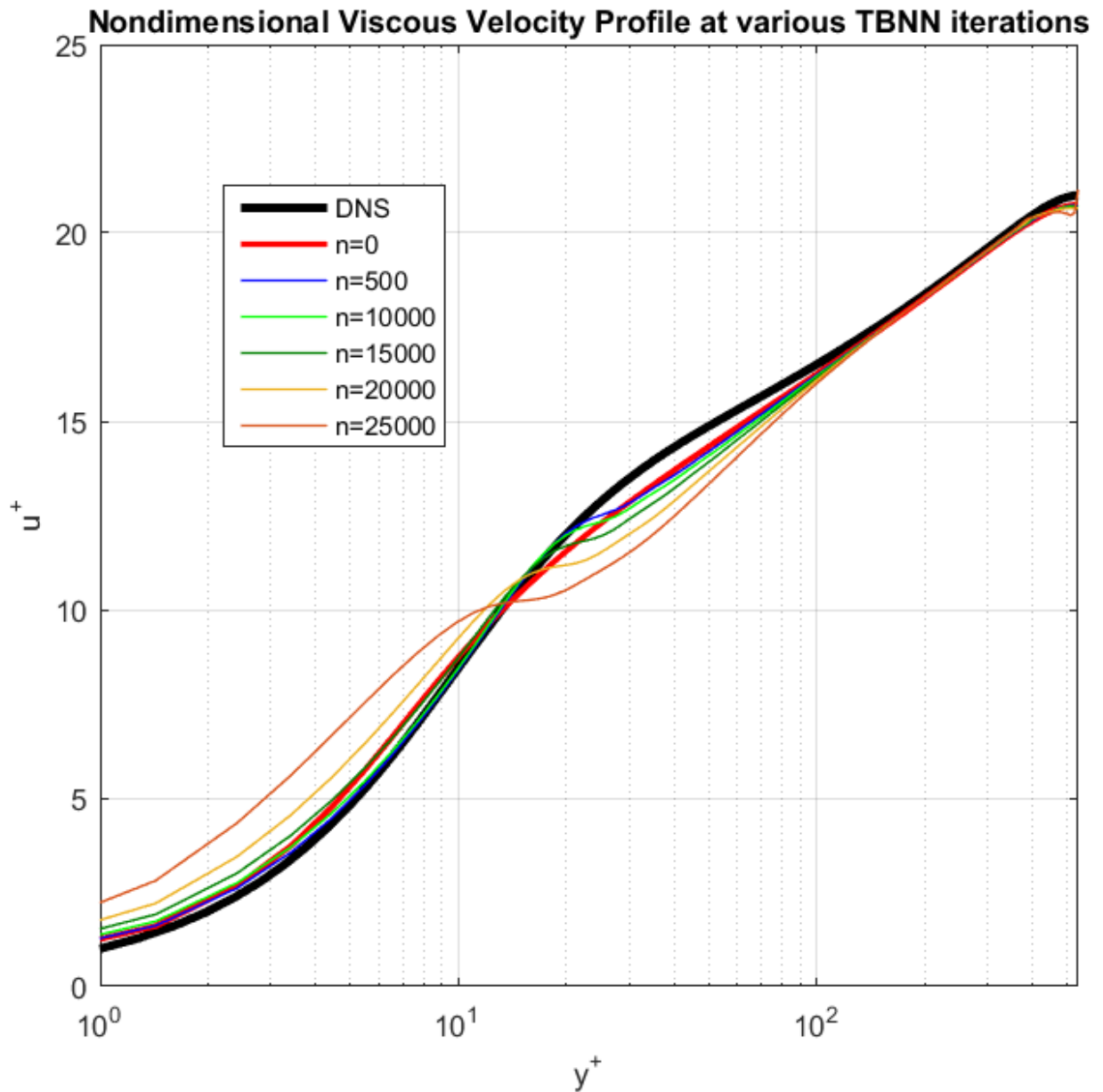


Figure 39: Mean velocity field resulting from the TBNN approach

In Fig.(39) above, the predicted mean velocity field $\langle u \rangle$ at various iterations n of the CFD RANS solver running with the TBNN scheme is shown. Iterations $n=0$ correspond to the converged RANS solution obtained with the standard LEVM. As one can observe, the mean velocity profile tend to

diverge from the correct DNS one as the iterations increase. This result is surprisingly negative, if one considers the improvement in the anisotropy stress tensor prediction showed by the TBNN in Fig.(34) compared to the LEVM. In order to interpret the results, a magnification of the $\langle uv \rangle$ component in Fig.(34) predicted by TBNN at first iteration is shown below in a semilogarithmic plot - as the mean velocity one:

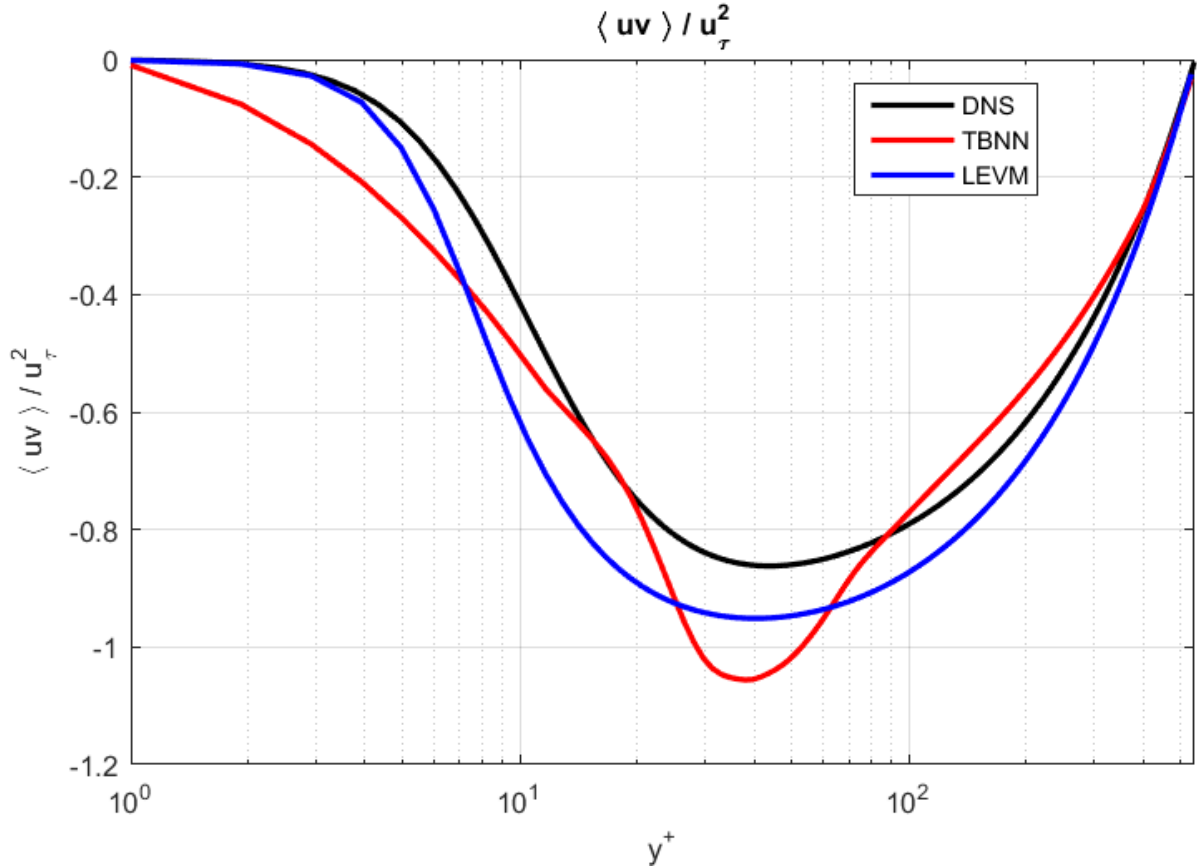


Figure 40: Turbulent Channel Flow: TBNN $\langle uv \rangle$ predicted profile

This $\langle uv \rangle$ component of the Reynolds stress tensor is particularly relevant since, in this particular flow case, it is the only one affecting the mean velocity field. By observing the comparison between the LEVM and TBNN profiles, one can observe that in two regions - $y^+ < 8$ and $y^+ \in [20, 90]$ - of the channel's height the TBNN performs worse than the LEVM in the prediction. Interestingly enough, the TBNN outperforms the LEVM in all the flow regions for all the other tensor's components as it results from Fig.(34). Yet, the normal stresses do not have any effect on the x momentum equation for $\langle u \rangle$. Comparing Fig.(40) and Fig.(39) one can observe that the regions of the flow where the TBNN and the DNS profiles diverges are the one where the $\langle uv \rangle$ prediction of the TBNN is less accurate than the LEVM one. As a consequence one can infer that:

- The TBNN significantly outperforms the LEVM at iteration 1 in the prediction of normal

stresses but the shear Reynolds stress prediction is worse in the near wall region and in the first part of the log-law region.

- The only Reynolds stresses component that affects the $\langle u \rangle$ field is the shear one and therefore the $\langle u \rangle$ profile predicted with the TBNN is worsened in the regions where the predictions of $\langle uv \rangle$ are worse.
- The worsened $\langle u \rangle$ profile brings to a worsened $\frac{\partial \langle u \rangle}{\partial y}$ profile, which is the main input to the TBNN. Indeed, by observing the different profiles in Fig.(39), it emerges clearly that in the viscous wall region the slope of $\langle u \rangle$ curve deviates significantly from the true one.
- The worsened input to the TBNN leads to an even worse prediction of the shear Reynolds stress and, iteratively, the solver diverges from the correct profile. One should also consider, indeed, that the TBNN can be much more unstable than an analytical function and therefore it is not granted that the model will have relevant convergence issues.

3.3 Conclusions

A deep learning approach to RANS turbulence modelling was presented. In an attempt to improve the standard LEVM for the closure of two-equations RANS models, a neural network with an architecture analogue to Ling's work [9] was trained on a large dataset of flows and then tested on the turbulent channel flow case. The network's architecture allows to embed Galilean invariance into the output tensor using a higher-order multiplicative layer. This ensures that predicted anisotropy tensor lay on a invariant tensor basis. The invariant Tensor Basis Neural Network was shown by Ling to have significantly more accurate predictions than a generic MLP that did not have any embedded invariance properties [18].

Yet, differently from the major approaches followed so far in the data driven turbulence modelling field, the TBNN was not used as a post-processing corrector tool to predict the Reynolds stresses field $\mathbf{b}(\mathbf{x})$ from the inputs of a converged standard RANS solution. Indeed, the TBNN was trained on DNS data only, in the attempt to find a machine learning mapping between the anisotropy stress tensor and the inputs of Pope's General Eddy Viscosity model to replace the LEVM model at each iteration of the CFD RANS solver. Interestingly, the LEVM can be seen as the Pope's GEVM where only one of the 10 coefficients have been tuned. Hence, in this approach we tested the ability of the network to learn about the underlying flow regimes present in various flow configurations and to provide a general, more complete model for the RANS closure problem. The accuracy of the TBNN was explored

in both an a priori and an a posteriori sense.

In the a priori results, corresponding to the training phase of the network, the TBNN showed a significant improvement in accuracy compared to [9] in terms of Root Mean Squared Error. From a visual analysis of the prediction performance for the Square Duct Flow case, it emerged how the TBNN model is able to predict both the qualitative and quantitative trends of the Reynolds stresses, significantly outperforming the LEVM.

As for the a posteriori evaluation, the TBNN was used as a replacement of the LEVM in a self-coded RANS solver using the low-Re Abe-Kondoh-Nagano version of $k - \varepsilon$ model. The approach was tested on a turbulent channel flow case for which DNS data were available for comparison [6]. We began our analysis by assessing the performance of the TBNN in predicting various components of the anisotropic Reynolds stress tensor and found that, at first iteration, the TBNN outperforms the classical LEVM except for the shear component in some flow regions. Now, it was of interest to determine whether the improved Reynolds stresses prediction would translate into better predictions of the mean axial velocity field $\langle u \rangle$. Unfortunately, in this flow case, the only Reynolds stress tensor component affecting the mean velocity field is the shear one. Hence, in the flow regions where the TBNN Reynolds stresses prediction proved worse than the LEVM ones, the $\langle u \rangle$ profiles deviates from the true DNS one, thus leading to a global worse result in terms of mean velocity. The convergence properties of the network resulted as well in a serious issue, with the $\langle u \rangle$ profile deviating from the DNS one more and more as the iterations went on.

To sum up, the approach yielded very promising a priori results yet, when tested on the specific flow case, the globally improved Reynolds stress predictions did not translate into an improved prediction of the mean flow field. Several avenues for future exploration can however be devised. First of all, it would be interesting to test the TBNN on a different flow configuration, maybe a more complex one, in which all the Reynolds stress components affect the mean velocity fields. Another further aspect to improve would be the convergence properties arising from the substitution of an analytical function with a TBNN at each iteration of a code. Lastly, another possible way to explore would be to include more inputs in the Pope's GEVM that the network tries to reply, to account for example for pressure gradient and non-locality of the Reynolds stress tensor. As far as the last solution is concerned, it is important to mention that, adding tensors and gradients as inputs of the GEVM significantly enlarge the tensor basis [15], thus making both more complex and computationally expensive than the TBNN.

CITED LITERATURE

- [1] Wu, Z., Laurence, D., and Afgan, I.: Direct simulation of hot jet in cold channel crossflow with temperature mixing. <https://doi.org/10.17632/7nx4prgjzz.4> [Online; accessed 13/03/2019]
- [2] Temmerman, L., Bentaleb, Y., and Leschziner, M.: Large Eddy Simulation of the flow over periodic hills. <https://turbmodels.larc.nasa.gov> [Online; accessed 14/03/2019]
- [3] Lardeau, S.: The interaction of round synthetic jets with a turbulent boundary layer separating from a rounded ramp. <https://turbmodels.larc.nasa.gov> [Online; accessed 14/03/2019]
- [4] Laval, J.-P.: Direct Numerical Simulations of Converging-Diverging Channel Flow. <https://turbmodels.larc.nasa.gov> [Online; accessed 14/03/2019]
- [5] Huser, A.: Direct Numerical Simulation of a Flow in a Square Duct. In Ph.D Thesis, University of Colorado at boulder (1992)
- [6] Lee, M., and Moser, R.: Direct numerical simulation of turbulent channel flow up to $Re_\tau = 5200$,. Journal of Fluid Mechanics, vol. 774, pp. 395-415 (2015)
- [7] Schlatter, P., and Orlu, R.: Assessment of direct numerical simulation data of turbulent boundary layers. Journal of Fluid Mechanics, vol. 842, pp. 128-145 (2018)
- [8] Lee, M., and Moser, R.: Extreme-scale motions in turbulent plane Couette flows. Journal of Fluid Mechanics, vol. 659, pp. 116 - 126 (September 2010)
- [9] Ling, J., Kurzwski, A., and Templeton, J.: Reynolds averaged turbulence modelling using deep neural networks with embedded invariance. In J. Fluid Mech. (2016), vol. 807, pp. 155-166 (2016)
- [10] Ling, J., Templeton, J., and Reese, J.: Machine Learning Strategies for Systems with Invariance Properties. In Journal of Computational Physics (2016)
- [11] Pope, S.B.: A more general effective-viscosity hypothesis. In J. Fluid Mech. (1975), vol. 72 part 2, pp. 331-340

- [12] Duraisamy,K.: Status, Emerging Ideas and Future Directions of Turbulence Modeling Research in Aeronautics. In NASA Technical Memorandum (November 2017)
- [13] Duraisamy,K., Alonso,J., and Durbin,P.: A Framework for Turbulence Modeling using Big Data. In Summary of Research, University of Michigan
- [14] Xiao,H.,Wu,J.,and Paterson,E.,: Physics-informed machine learning approach for augmenting turbulence models: A comprehensive framework. In Physical Review Fluids (July 2018)
- [15] Wang,J.-X., Wu,J.-L., and Xiao,H.: A Physics Informed Machine Learning Approach for Reconstructing Reynolds Stress Modeling Discrepancies Based on DNS Data. In Physical Review Fluids (February 2017)
- [16] Duraisamy,K., Iaccarino,G., and Xiao,J.: Turbulence Modeling in the Age of Data. In Annual Review of Fluid Mechanics, vol. 51, pp. 357-377 (2019).
- [17] Tracey,B.,Duraisamy,K.,Alonso,J.J.: A Machine Learning Strategy to Assist Turbulence Model Development. In AIAA SciTech Forum (January 2015)
- [18] Fang,R.,Sondak,D.Protopapas,P. and Succi,S.: Deep learning for turbulent channel flow. <https://arxiv.org/abs/1812.02241> [Online; accessed 15/04/2019]
- [19] Kuzmin, D. and Mierka, O.: On the implementation of the $k-\varepsilon$ turbulence model in incompressible flow solvers based on a finite element discretization In International Journal of Computing Science and Mathematics (January 2007)
- [20] Nptel:Solution of Navier-Stokes Equations for Incompressible Flows Using SIMPLE and MAC Algorithms. <https://nptel.ac.in/courses/112104030/pdf/lecture27.pdf> [Online; accessed 03/04/2019]
- [21] Harlow, F.H., and Welch,J.E.: Numerical Calculation of Time-Dependent Viscous Incompressible Flow of Fluid with Free Surface In Physics of Fluids, Volume 8, Issue 12, p.2182-2189, (1965).
- [22] Rechial,A. , Naji, H., Mompean,G.,El Marjani, A.: Numerical simulation of turbulent flow through a straight square duct using a near wall linear $k-\varepsilon$ model In Int. Jnl. of Multiphysics Volume 1, Number 3 (2007)

- [23] Abe,K.,Kondoh,K.Nagano,Y.: A new turbulence model for predicting fluid flow and heat transfer in separating and reattaching flows-I. Flow field calculations. In *Int. J. Heat and Mass Transfer* 37(1), pp 138-151 (1994)
- [24] Gorji,A.,Seddighi,M.,Ariyaratne,C.,Vardy,A.E.,O'Donoghue,T.,Pokrajac,D., and He,S.: A comparative study of turbulence models in a transient channel flow. In *Computer & Fluids*, vol.89, pp. 111-123 (2014)
- [25] Jagadeesh,P., and Murali,K.: Application of low-Re turbulence models for flow simulations past underwater vehicle hull forms. *Journal of Naval Architecture and Marine Engineering* (January 2005)
- [26] Sondak,D.,Pletcher,R.H.,Vandalsem,W.R.: Wall functions for the $k - \varepsilon$ turbulence model in generalized nonorthogonal curvilinear coordinates. <https://doi.org/10.31274/rtd-180813-11746> [Online;accessed 06/04/2019]
- [27] Suga,K.: Recent Developments in Eddy Viscosity Modelling of Turbulence. *R & D Review of Toyota CRDL*, vol.33, No.1 (1998)
- [28] Liu,F. and Zheng,X.: A Strongly Coupled Time-Marching Method for Solving the Navier-Stokes and $k - \omega$ Turbulence Model Equations with Multigrid In *Journal of Computational Physics*, vol.128, pp. 289-300 (1996)
- [29] LEAP CFD Team: Tips & Tricks: Estimating the First Cell Height for correct y^+ . <https://www.computationalfluidynamics.com.au/tips-tricks-cfd-estimate-first-cell-height/> [Online; accessed 15/05/2019]
- [30] ANSYS Theory Guide: Enhanced Wall Treatment.
<https://www.afs.enea.it/project/neptunius/docs/fluent/html/th/node101.htm> [Online; accessed 15/05/2019]
- [31] ANSYS support - Davoudabadi P.: The Most Accurate and Advanced Turbulence Capabilities. <https://support.ansys.com/staticassets/ANSYS/Conference/Confidence/Chicago/Downloads/most-accurate-advanced-turbulence-capabilities.pdf> [Online;accessed 01/05/2019]
- [32] Keras Documentation: Keras, The Python Deep Learning library. <https://keras.io/> [Online;accessed 15/02/2019]

- [33] Ruder,S: An overview of gradient descent optimization algorithms. <https://ruder.io/optimizing-gradient-descent/> [Online;accessed 15/02/2019]
- [34] Bushaev,V.: Adam,latest trends in deep learning optimization. <https://towardsdatascience.com/> [Online;accessed 15/02/2019]
- [35] Jaitley,U.: Why Data Normalization is necessary for Machine Learning models. <https://medium.com/@urvashilluniya/why-data-normalization-is-necessary-for-machine-learning-models-681b65a05029> [Online;accessed 15/02/2019]
- [36] Almaliki,Z.A.: Standardization VS Normalization <https://medium.com/@zaidalissa/standardization-vs-normalization-da7a3a308c64>[Online; accessed 15/02/2019]
- [37] Ferziger,J.H.,and Peric,M.: Computational methods for fluid dynamics Springer (2002).
- [38] Pope,S.B: Turbulent Flows. Cambridge University Press (2000)
- [39] Patankars,S.V.: Numerical Heat Transfer and Fluid Flow. Taylor & Francis (1980)
- [40] Versteeg,H.G. and Malalasekera,W.: An Introduction to Computational Fluid Dynamics. The Finite Volume Method. Pearson, 2nd Edition (2007)